Chapter 10

Expected performance of the ATLAS detector

10.1 Introduction

Since the publication of the ATLAS Detector and Physics Performance Technical Design Report [248] in 1999, all the detector components of the experiment have been constructed and integrated and most of them have been installed (see section 9.6). A detailed understanding of their features (geometry, amount of material and placement accuracy) has been achieved over this period, as described elsewhere in this article.

The purpose of this chapter is to present an overview of the main performance features of the ATLAS experiment, as expected today from the latest round of simulations and the current version of the reconstruction software and as validated wherever possible using test-beam measurements. It is therefore a snapshot of the present understanding of the performance of the detector. Somewhat in contrast to earlier documents, in particular the Detector and Physics Performance TDR [248], the performance results presented here will focus on the initial low-luminosity scenario for the beginning of data-taking at the LHC. Since the luminosity is expected to rise over the first year or so from 10^{31} cm^{-2} s^{-1} to 10^{33} cm^{-2} s^{-1}, most of the results presented below will correspond to simulated events without pile-up nor neutron background (see section 3.1), except in certain explicit cases where their contributions at luminosities of $\approx 10^{33}$ cm^{-2} s^{-1} have been considered.

The first two sections are devoted to the expected tracking performance in ATLAS and its powerful but complex magnet system (see chapter 2). The overall expected performance of the inner detector is described in section 10.2, while that of the muon spectrometer, both stand-alone and combined with the inner detector, is presented in section 10.3. Sections 10.4 (electrons and photons), 10.5 (hadronic jets), 10.6 (missing transverse energy), 10.7 (hadronic τ-decays), 10.8 (tagging of heavy flavours) and 10.9 (trigger) describe the expected performance of the overall ATLAS detector with respect to triggering, reconstruction, identification and measurement of the major final-state objects over the required range of energies for most of the physics channels of interest at the LHC.

2008 JINST 3 S08003

10.1.1 Realistic data challenge

Over the past seven years, a large and modular suite of software tools for simulation and reconstruction has been developed and integrated into the ATLAS computing model and first full-scale exercises of the operation of this computing model have begun. A large number of high-statistics samples of Monte-Carlo events have been run through the complete ATLAS simulation, reconstruction and analysis chain to assess the readiness of the overall system to cope with the initial data. Results from this data challenge, in particular from its calibration and alignment component, will be presented wherever relevant in this chapter.

As part of the preparations for initial data-taking, the simulation software has been adapted to describe and simulate, in addition to the ideal ATLAS detector description most commonly used, an ATLAS experimental set-up with alignment and placement shifts which are similar in size to those anticipated in the real detector. These have been included from macro-assembly to individual module level, as for example in the inner detector. In addition, magnetic field and material distortions have been included wherever relevant, as well as calibration distortions of the electromagnetic and hadronic calorimeters for certain specific studies. The results presented here are based on many tens of millions of events, originating from a variety of physics processes and event generators, and with the detector response simulated using GEANT 4 (version G4.7.1.p01 and QGSP GN physics list) [220, 249].

The results published more than eight years ago in ref. [248] correspond to a detector description which is quite different from the current one. Several real changes happened to the layout of the ATLAS detector:

- the η-coverage of the TRT has been decreased from $|\eta| < 2.5$ to $|\eta| < 2.0$, resulting in a significant loss of performance in that region (momentum resolution, tracking performance and electron identification);
- the end-cap cryostats and the extended barrel tile calorimeters have been recessed by 40 mm in z to make room for inner-detector services;
- certain end-cap muon chambers dedicated to momentum measurements in the transition region between the barrel and end-cap toroids have been deferred in terms of construction and installation in ATLAS, resulting in a significant loss in stand-alone performance (efficiency and momentum resolution).

In addition, the description of the installed detector has improved considerably:

- the amount of material in the inner detector and just in front of the electromagnetic calorimeter has increased substantially;
- the amount of material in the muon spectrometer has increased substantially in several areas.

For these reasons, the expected performance is somewhat worse than that published in ref. [248]. Only the most striking examples can be given in this article:

- the 25% degradation in the expected resolution for the invariant mass of four muons from Higgs-boson decay for $m_H = 130$ GeV reconstructed in stand-alone mode (see figure 10.40).

2008 JINST 3 S08003

This degradation is due in equal proportions to the missing chambers in the transition region between the barrel and end-cap toroids and to the increase of the material in the description of the muon spectrometer;

- the 12% degradation in the expected resolution for the reconstructed invariant mass of four electrons from Higgs-boson decay for $m_H = 130\,\text{GeV}$ (see figure 10.60) and of two photons from Higgs-boson decay for $m_H = 120\,\text{GeV}$ (see figure 10.61);
- the expected degradations in performance are smaller for other channels such as $Z \rightarrow \tau\tau$.

The model of the set-up used for the results presented here differs nevertheless from the reality in the ATLAS cavern, as it is has been described in the inner-detector, calorimeter and muon-spectrometer chapters, in several important respects since it had to be frozen for large-scale simulation:

- the amount of material in the inner detector has increased in some services regions of the active volume by a few percent of a radiation length, X_0 (at maximum 7% X_0);
- the amount of material in the inner detector outside the active volume and therefore near to the barrel and end-cap cryostats of the LAr calorimeter has increased by substantial amounts in certain regions: by 3.5% X_0 for $|\eta| < 0.7$, by 35–40% X_0 for $|\eta|$ increasing from 0.8 to 1.1, by 50–80% X_0 for $1.1 < |\eta| < 1.8$ and by 15% X_0 for $1.8 < |\eta| < 2.2$;
- the amount of material in the muon spectrometer is larger in certain areas than what has been included in the detector description for the results presented here. The largest missing items are the support structures for the small and big wheels (a few tens of tonnes), the saddle support structures for the barrel calorimetry, the inner-detector PP2 patch-panels, and more generally specific mechanical supports and services throughout the muon spectrometer. The uncertainties on the knowledge of this extra material will remain large until the installation of the last few macro-components in the pit has been completed.

10.1.2 Combined test-beam

The understanding of the detector components has improved considerably over the many years of construction, especially with extensive measurements in test-beams of the stand-alone and combined performance of the various calorimeters in the H6 and H8 test-beam facilities at CERN. The main results of these measurements are summarised in section 5.7.

A dedicated effort to understand the combined performance of a complete slice of the ATLAS detector, from the pixel detectors to the outermost stations of the muon chambers, took place in 2004 with the large-scale combined test-beam (CTB) exercise. Figure 10.1 shows a sketch of the layout of the CTB set-up, and figures 10.2 and 10.3 show respectively pictures of some of the actual tracking and calorimeter components and of some of the muon chamber components, as they were operated in 2004.

This effort has led to an improved detector description, and also to first sets of detailed calibration and alignment procedures, essential to the initial understanding of the detector performance

2008 JINST 3 S08003

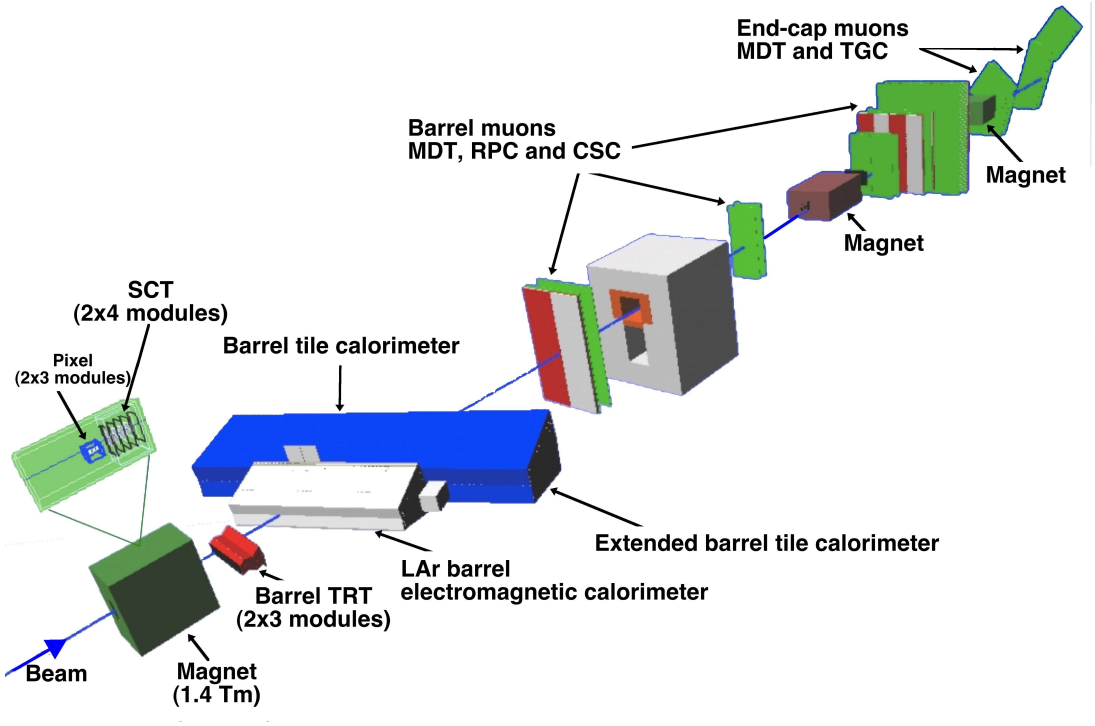

Figure 10.1: Sketch of the ATLAS combined test-beam set-up.

and to the extraction of the first physics results. The main results obtained from these measurements and from their comparison to the detailed simulation of the detector (used both for the CTB and for ATLAS itself) are presented in this article:

- the inner-detector alignment results are presented in section 10.2.2;
- the TRT electron identification results are presented in section 10.2.5;
- the muon-chamber alignment results are presented in section 10.3.2;
- the electromagnetic calorimeter energy measurement results are presented in section 5.7 together with all the other test-beam results related to stand-alone and combined calorimeter performance;

A general consequence of the various combined calorimeter test-beam efforts and of the CTB data analysis in particular is that the detector description of the barrel electromagnetic calorimeter and the calibration software of the various calorimeters have been considerably refined to reach agreement between test-beam data and simulation. These refinements are fully integrated into the ATLAS software framework for the experiment itself, a necessary condition to the desired tight coupling between test-beam simulation and data analysis and the actual simulation of physics collisions in ATLAS.

2008 JINST 3 S08003

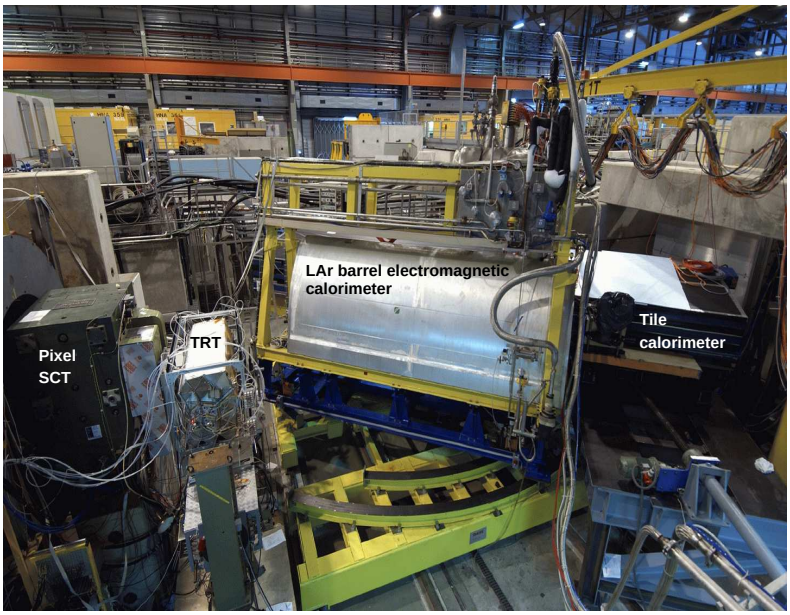

Figure 10.2: Picture of the combined test-beam set-up for the inner detector and the calorimeters. The beam particles come from the left of the picture, traverse the magnet and then hit the calorimeters on the right side of the picture. On the left, just behind the pole tips of the magnet in which the pixel and SCT modules were installed, are the barrel TRT modules. On the yellow rotating support table is the cryostat housing the LAr electromagnetic calorimeter modules and behind it (right side of the picture) are the tile calorimeter barrel (not visible) and extended barrel modules.

Figure 10.3: Picture of the combined test-beam set-up for the end-cap muon chamber system. The beam particles come from the right side of the picture, traverse the barrel muon chamber set-up, which is mostly hidden by the concrete blocks, and then go through three stations of end-cap MDT and TGC chambers.

2008 JINST 3 S08003

10.2 Reconstruction and identification of charged particles in the inner detector

Charged particle tracks with transverse momentum $p_T > 0.5\,\text{GeV}$ and $|\eta| < 2.5$ are reconstructed and measured in the inner detector and the solenoid field. The efficiency at low momentum is, however, limited because of the large amount of material in the inner detector (see section 4.10 and figure 4.45). The intrinsic measurement performance expected for each of the inner-detector sub-systems is described in section 4.1. This performance has been studied extensively over the years [60], both before and after irradiation of production modules, and also, more recently, during the combined test beam (CTB) runs in 2004 as described in section 10.1, and in a series of cosmic-ray tests in 2006 as described in section 4.9. The results have been used to update and validate the modelling of the detector response in the Monte-Carlo simulation. This section describes the expected performance of the inner detector in terms of alignment, tracking, vertexing and particle identification.

10.2.1 Track reconstruction

The inner-detector track reconstruction software [250] follows a modular and flexible software design, which includes features covering the requirements of both the inner-detector and muon-spectrometer reconstruction (see section 10.3 for a description of the strategies used for muon reconstruction). These features comprise a common event data model [251] and detector description [252], which allow for standardised interfaces to all reconstruction tools, such as e.g. track extrapolation, track fitting including material corrections, and vertex fitting. The extrapolation package combines propagation tools with an accurate and optimised description of the active and passive material of the full detector [253] to allow for material corrections in the reconstruction process. The suite of track-fitting tools includes global-χ^2 and Kalman-filter techniques, and also more specialised fitters, such as dynamic noise adjustment [254], Gaussian-sum filters [255] and deterministic annealing filters [256]. Other common tracking tools are provided, e.g. to apply calibration corrections at later stages of the pattern recognition, to correct for module deformations or to resolve hit-association ambiguities.

Track reconstruction in the inner detector is logically sub-divided into three stages:

1. A pre-processing stage, in which the raw data from the pixel and SCT detectors are converted into clusters and the TRT raw timing information is turned into calibrated drift circles. The SCT clusters are transformed into space-points, using a combination of the cluster information from opposite sides of a SCT module.

2. A track-finding stage, in which different tracking strategies [250, 257], optimised to cover different applications, are implemented. The default tracking exploits the high granularity of the pixel and SCT detectors to find prompt tracks originating from the vicinity of the interaction region. First, track seeds are formed from a combination of space-points in the three pixel layers and the first SCT layer. These seeds are then extended throughout the SCT to form track candidates. Next, these candidates are fitted, outlier clusters are removed, ambiguities in the cluster-to-track association are resolved, and fake tracks are rejected. This

2008 JINST 3 S08003

is achieved by applying quality cuts, e.g. on the number of associated clusters, with explicit limits set on the number of clusters shared between several tracks and the number of holes per track (a hole is defined as a silicon sensor crossed by a track without generating any associated cluster). The selected tracks are then extended into the TRT to associate drift-circle information in a road around the extrapolation and to resolve the left-right ambiguities. Finally, the extended tracks are refitted with the full information of all three detectors and the quality of the refitted tracks is compared to the silicon-only track candidates and hits on track extensions resulting in bad fits are labelled as outliers (they are kept as part of the track but are not included in the fit).

A complementary track-finding strategy, called back-tracking, searches for unused track segments in the TRT. Such segments are extended into the SCT and pixel detectors to improve the tracking efficiency for secondary tracks from conversions or decays of long-lived particles.

3. A post-processing stage, in which a dedicated vertex finder is used to reconstruct primary vertices. This is followed by algorithms dedicated to the reconstruction of photon conversions and of secondary vertices.

10.2.2 Alignment of the inner detector

The alignment of the inner detector is a crucial component in reaching the required tracking performance. The alignment procedure must determine accurately the actual positions in space of the silicon modules (pixel and SCT) as well as of the straws (or groups of straws) in the TRT modules. The task therefore corresponds to the determination of six degrees of freedom for each module, if it is treated as a rigid body. It will also be necessary to correct for imperfections within the modules, due to temperature gradients, module bows or other distortions. To ensure that the misalignment of silicon modules does not inflate the track parameter uncertainties by more than 20% above the intrinsic resolution at high-p_T, the module positions need to be determined with a precision of approximately 10 μm or better in the bending plane [60]. For a precision measurement of the mass of the W-boson, an understanding of the module positions at the level of 1 μm or better is required. The expected as-built and survey precisions of the inner-detector components before data-taking are described in section 4.3, and their overall placement accuracy inside the inner bore of the barrel LAr cryostat is summarised in table 4.11.

Alignment constants for the inner detector will be derived from a dedicated stream of tracks selected at a rate of $\sim$ 10 Hz, and will be updated if required every 24 hours. To reach a precision of 10 μm on the silicon-module positions, approximately one million good tracks with various topologies will be selected within this 24 hour period and written out to the calibration and alignment stream at the time of the final high-level trigger decision.

Several different track-based alignment techniques have been applied to CTB data, to cosmic-ray data and to Monte-Carlo simulations of a misaligned inner detector. All the approaches are based on the minimisation of hit residuals from high-momentum tracks, which are preferred because of their lower multiple-scattering distortions. The minimisation of track residuals is a necessary but not sufficient requirement for the alignment of the inner detector. Certain global distortions

of the geometry may not be or may only weakly be constrained by such tracks (these are called "weak modes"). While preserving the helical trajectory of the track, these modes would, in general, lead to biases on the measured track parameters. Sagitta distortions, which arise from systematic biases in the measurement of q/p_T, where q is the charge of the track, are one of the prominent examples.

To constrain and eliminate these weak modes, it is important to use tracks with different topologies:

- tracks from the interaction point, which will always constitute the bulk of the sample of tracks used for alignment. Using the primary vertex as an additional constraint will help to eliminate certain weak modes;
- cosmic-ray tracks, which have the advantage of providing a continuous helical trajectory across the whole inner detector, thereby mimicking a pair of opposite-sign equal-momentum and back-to-back tracks, when they pass close to the interaction point. In addition, a large fraction of the cosmic-ray tracks will cross the inner detector far from the beam axis, thereby providing additional constraints to eliminate certain weak modes;
- tracks from beam halo will help to constrain the initial alignment of the end-cap regions;
- tracks passing through the overlap regions of adjacent modules. These constrain the circumference of cylindrical geometries and thus improve the determination of the average radial position of the modules;
- track pairs from Z and J/ψ decays. Fitting these tracks to a common decay vertex and to a known invariant mass will provide sensitivity to systematic correlations between different detector elements;
- finally, additional constraints are provided by the information from survey measurements, which are, however, limited in practice to the relationships between nearby detector elements connected by rigid support structures.

With the unprecedented number of detector modules in the inner detector, the alignment task is immense in its scope and complexity. With the aim of simplifying it, the alignment procedure can be broken down into several steps. As a first step, the large detector structures (the barrel and the end-caps of each of the three sub-systems) are aligned with respect to each other. By treating these large-scale structures as rigid bodies with only a few degrees of freedom, the procedure converges on a global alignment with only limited statistics of reconstructed tracks. To achieve this goal, it is planned that sufficient cosmic-ray data be taken before LHC turn-on. In a second step, the individual barrel layers and end-cap disks can be aligned with respect to each other, leading to a system with several hundreds of degrees of freedom. In a third step, the complete alignment of all the detector modules implies resolving a system with almost 36,000 degrees of freedom (1744 pixel modules, 4088 SCT modules and 136 TRT modules) and therefore requires the large samples of tracks mentioned above. The last step in the whole process requires the study of possible residual biases, using resonances decaying to muons, E/p measurements combining inner detector and electromagnetic calorimetry, and combined muon measurements with the muon spectrometer (see section 10.3.2).

2008 JINST 3 S08003

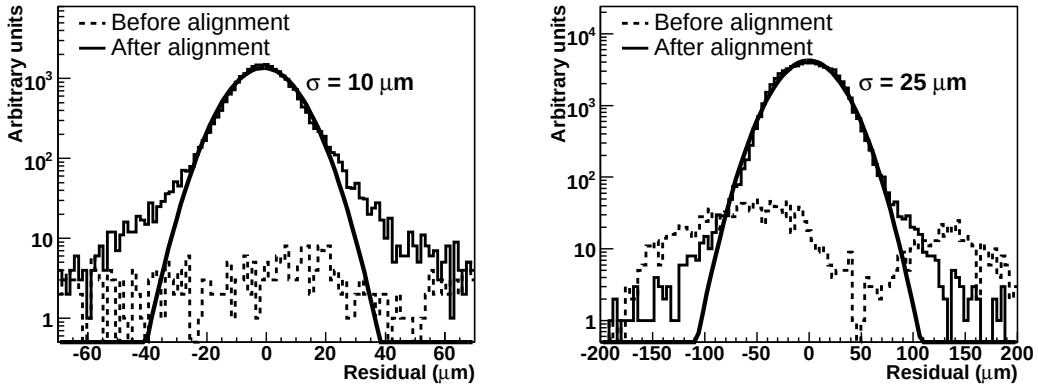

Figure 10.4: Distributions of pixel (left) and SCT (right) residuals for the most accurate measurement coordinate, as obtained for charged pions with an energy of 100 GeV in the combined test-beam data. The results are shown for tracks reconstructed in the pixel and SCT detectors before (dashed histogram) and after (full histogram) alignment. The curves represent Gaussian fits to the residuals after alignment. Because of the large misalignments of certain modules, most of the entries before alignment lie outside the boundaries of the plots.

10.2.2.1 Alignment in the combined test-beam

The alignment procedure has been applied to CTB data [258] using charged-hadron beams with energies between 5 and 180 GeV. The results obtained are shown in figure 10.4, in the case of one beam energy of 100 GeV, for the pixel and SCT residuals for the most accurate measurement coordinate. The striking improvement observed in the residual distributions after alignment arises from alignment constants changing by typically 100–200 μm for some of the pixel and SCT modules. The measured resolutions after alignment are in agreement with those expected from Monte-Carlo simulation of the CTB set-up with a perfect alignment.

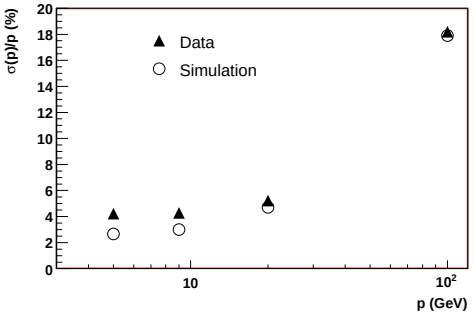

Figure 10.5: Fractional momentum resolution for pions as a function of pion momentum. The results are compared between data after alignment (see text) and simulation.

Figure 10.5 compares the measured momentum resolution for pions after alignment with that expected from Monte-Carlo simulation as a function of the pion momentum which ranges from 5 to 100 GeV. The mean of the beam momentum as measured using the pixels and the SCT is correct to $\sim 1\%$ at the highest energy of 100 GeV, indicating that residual misalignments are small. The disagreement observed at the lower end of the momentum spectrum is most likely related to the quality of the data taken with low-energy beams (a mix of electrons and pions taken early in the run when the operation of the pixel and silicon detectors was less stable than for the higher-energy runs).

2008 JINST 3 S08003

10.2.2.2 Misaligned inner detector in ATLAS simulation

Within the context of the realistic data challenge described in section 10.1, the inner-detector alignment algorithms are undergoing stringent tests, based on events simulated with a misaligned inner-detector geometry and reconstructed with the nominal geometry. The main focus of these tests is to study the various alignment approaches [259–261] within a realistic and full-scale scenario typical of what can be expected with initial data. One issue of particular interest is the implementation and validation of robust methods to determine and eliminate the weak modes, especially the sagitta distortions. The misalignments introduced for the realistic data challenge do not, however, cover all possible misalignment scenarios. In particular, systematic deformations of large scale structures like end-cap disks or barrel layers are not simulated. Twists or radial deformations of the barrel layers are known to correspond to weak modes of the alignment.

Nevertheless, a number of systematic displacements and rotations of large and smaller-scale structures were introduced, in addition to the smaller and random misalignments introduced at the module level. This resulted in initially low efficiency for reconstructing certain tracks and in track-parameter distortions of large magnitude (the expected mass peak for $Z \rightarrow \mu\mu$ decays was not initially visible). To converge on the first-pass alignment results presented here, reconstructed tracks were constrained to the beam-line and tracks from simulated cosmic-ray events were also used to provide additional constraints.

The impact of global sagitta distortions on the reconstructed invariant masses of neutral resonances decaying into oppositely charged particles is in principle only a small effect, since the momenta of the positively and negatively charged daughters are shifted in opposite directions. However, ϕ-dependent sagitta distortions may give rise to larger effects, which can become very significant at relatively high momentum (depending on the size and systematic nature of the residual misalignments). Figure 10.6 shows the effect of these residual misalignments on reconstructed $Z \rightarrow \mu\mu$ decays after applying the corrections obtained from a first-pass alignment of the inner detector based on high-p_T muons and cosmic rays. The monitoring of the evolution of the alignment constants during the various stages of this first-pass alignment has shown that residual distortions on the track parameters remain, even after using cosmic rays to remove some of the weak modes to which tracks originating from the interaction point are not very sensitive. The residual distortions are observed to be much smaller in the barrel than in the end-caps, for which the constraints provided by cosmic rays are much weaker. The fitted Gaussian widths of the reconstructed $Z \rightarrow \mu\mu$ peaks in figure 10.6 are 2.6 GeV for the ideal (or perfectly aligned) inner detector and 3.9 GeV for the inner detector after completing the first-pass alignment.

A measure of these residual distortions can be extracted, as one would do with real data, by searching for possible asymmetries between the p_T-spectra of negative and positive muons from $Z \rightarrow \mu\mu$ decays. This is illustrated in figure 10.7 which clearly demonstrates a significant residual asymmetry between the two spectra after the first-pass alignment. This large asymmetry is clearly related to the large residual contribution of 2.9 GeV to the resolution on the reconstructed dimuon mass after the first-pass alignment. If this residual width were for example ten times smaller, then a few days of data-taking at a luminosity of 10^{31} cm^{-2} s^{-1} would be required to actually detect a significant effect using $Z \rightarrow \mu\mu$ decays.

2008 JINST 3 S08003

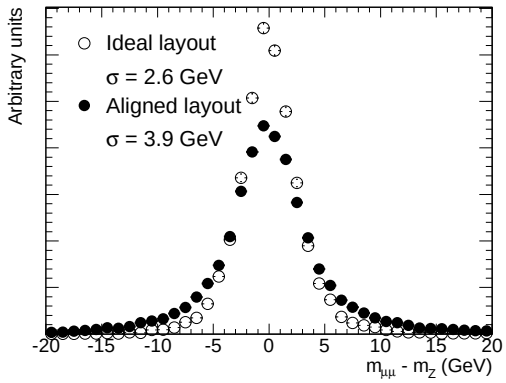

Figure 10.6: Difference between the reconstructed and true mass of dimuon pairs from $Z \rightarrow \mu\mu$ decay. The results are shown in the case of an ideal (perfectly aligned) inner detector (open circles) and for the inner detector after a first-pass alignment (full circles), based on high-p_T muon tracks and cosmic rays (see text).

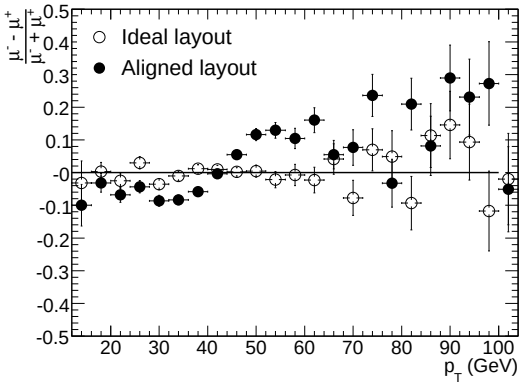

Figure 10.7: Asymmetry between negative and positive muons as a function of p_T, as obtained for the sample of $Z \rightarrow \mu\mu$ decays reconstructed in the inner detector and described in the text. The results are shown in the case of an ideal (perfectly aligned) inner detector (open circles) and for the inner detector after a first-pass alignment (full circles).

10.2.3 Tracking performance for single particles and particles in jets

The expected performance of the tracking system for reconstructing single particles and particles in jets is determined using a precise modelling of the individual detector response, geometry and passive material in the simulation. In this section, a consistent set of selection cuts for reconstructed tracks has been used throughout. Only prompt particles with $p_T > 1$ GeV and $|\eta| < 2.5$ are considered. Standard quality cuts require reconstructed tracks to have at least seven precision hits (pixels and SCT); in addition, the transverse and longitudinal impact parameters at the point of closest approach to the vertex must fulfil respectively $|d_0| < 2\,\text{mm}$ and $|z_0 - z_v| \times \sin\theta < 10\,\text{mm}$, where z_v is the position of the primary vertex along the beam and θ is the polar angle of the track. Stricter selection cuts, called b-tagging cuts, are defined by: at least two hits in the pixels and one in the vertexing layer, as well as $|d_0| < 1\,\text{mm}$ and $|z_0 - z_v| \times \sin\theta < 1.5\,\text{mm}$. A reconstructed track is matched to a Monte-Carlo particle if at least 80% of its hits were created by that particle. The efficiency is defined as the fraction of particles which are matched to reconstructed tracks passing the quality cuts, and the fake rate is defined as the fraction of reconstructed tracks passing the cuts which are not matched to a particle.

The resolution of a track parameter X can be expressed as a function of p_T as:

$$\sigma_X = \sigma_X(\infty)(1 \oplus p_X/p_T),$$

where $\sigma_X(\infty)$ is the asymptotic resolution expected at infinite momentum and p_X is a constant representing the value of p_T, for which the intrinsic and multiple-scattering terms are equal for the parameter X under consideration. This expression is approximate, working well at high p_T (where the resolution is dominated by the intrinsic detector resolution) and at low p_T (where the resolution is dominated by multiple scattering). Figures 10.8, 10.9 and 10.10 show the momentum resolution

Table 10.1: Expected track-parameter resolutions (RMS) at infinite transverse momentum, $\sigma_X(\infty)$, and transverse momentum, p_X, at which the multiple-scattering contribution equals that from the detector resolution. The momentum and angular resolutions are shown for muons, whereas the impact-parameter resolutions are shown for pions (see text). The values are shown for two η-regions, one in the barrel inner detector where the amount of material is close to its minimum and one in the end-cap where the amount of material is close to its maximum.

Track parameter	$0.25 < \|\eta\| < 0.50$		$1.50 < \|\eta\| < 1.75$	
	$\sigma_X(\infty)$	p_X (GeV)	$\sigma_X(\infty)$	p_X (GeV)
Inverse transverse momentum ($1/p_T$)	0.34 TeV^{-1}	44	0.41 TeV^{-1}	80
Azimuthal angle (ϕ)	70 μrad	39	92 μrad	49
Polar angle ($\cot\theta$)	0.7×10^{-3}	5.0	1.2×10^{-3}	10
Transverse impact parameter (d_0)	10 μm	14	12 μm	20
Longitudinal impact parameter ($z_0 \times \sin\theta$)	91 μm	2.3	71 μm	3.7

for muons and the transverse and longitudinal impact parameter resolutions for pions, all without any beam constraint and assuming the effects of misalignment to be negligible. Table 10.1 shows the values of $\sigma_X(\infty)$ and p_X for tracks in two η-regions, corresponding to the barrel and end-caps. The TRT measurements are included in the track fits for tracks with $|\eta| < 2.0$, beyond which there are no further TRT measurements. The impact parameter resolutions are quoted only for tracks with a hit in the vertexing-layer (this requirement has a very high efficiency, as illustrated below).

The determination of the lepton charge at high p_T is particularly important for measuring charge asymmetries arising from the decays of possible heavy gauge bosons (W' and Z'). Typically, such measurements require that the charge of the particle be determined to better than 3σ. Whereas the muon charge can be reliably measured at the highest momenta in the muon system, only the inner detector can measure the charge of electrons. The fraction of electrons for which the sign of the charge is wrongly determined is shown in figure 10.11, together with the same fraction for muons, included as a reference (perfect alignment has been assumed). For the muons, the fraction is well described by the nominal (Gaussian) resolution, whereas electrons are more complicated since they are subject to bremsstrahlung. This should help for charge determination since the momentum is reduced, but sometimes the electrons overlap with subsequent conversion electrons from the bremsstrahlung photons, which may cause pattern-recognition problems because of extra hits and overlaps. For $p_T < 1$ TeV, the sign of the curvature of a track is sufficiently well determined that the benefit from bremsstrahlung is small and the overlap problem dominates the electron reconstruction, causing the electron charge determination to be of worse quality than for muons. However at 2 TeV, the poor intrinsic resolution is the dominant factor, and the effect of bremsstrahlung compensates for the pattern-recognition problems.

Figure 10.12 shows the efficiencies for reconstructing muons, pions and electrons with a transverse momentum of 5 GeV, whereas figure 10.13 shows the efficiencies for reconstructing pions with p_T varying from 1 to 100 GeV. In addition to multiple-scattering, pions are affected by hadronic interactions in the inner-detector material, while electrons are subject to even larger reconstruction inefficiencies because of bremsstrahlung. As a result, the efficiency curves as a function of $|\eta|$ for pions and electrons reflect the shape of the amount of material in the inner detector (see figures 4.45 and 4.46). As expected, the efficiency becomes larger and more uniform as a function of $|\eta|$ at higher energies.

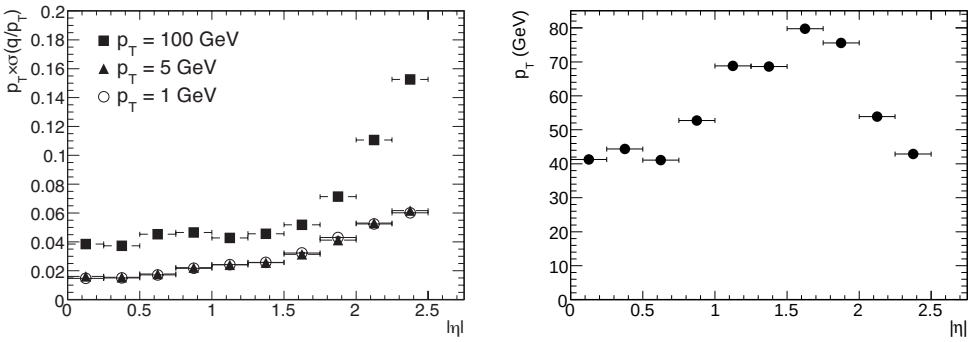

Figure 10.8: Relative transverse momentum resolution (left) as a function of $|\eta|$ for muons with $p_T = 1\,\text{GeV}$ (open circles), 5 GeV (full triangles) and 100 GeV (full squares). Transverse momentum, at which the multiple-scattering contribution equals the intrinsic resolution, as a function of $|\eta|$ (right).

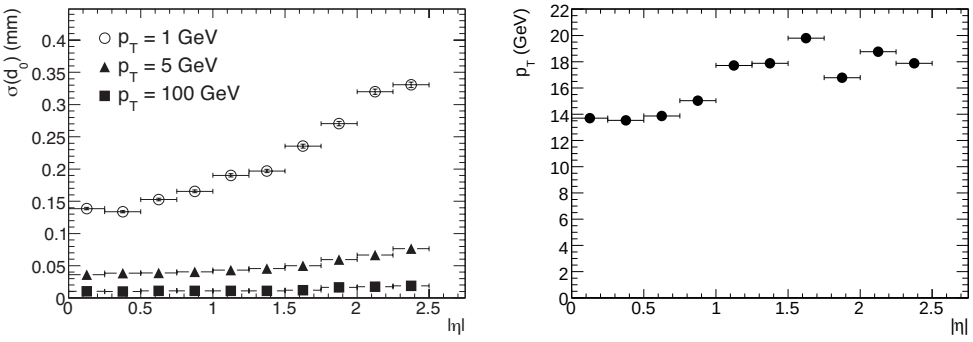

Figure 10.9: Transverse impact parameter, d_0, resolution (left) as a function of $|\eta|$ for pions with $p_T = 1\,\text{GeV}$ (open circles), 5 GeV (full triangles) and 100 GeV (full squares). Transverse momentum, at which the multiple-scattering contribution equals the intrinsic resolution, as a function of $|\eta|$ (right).

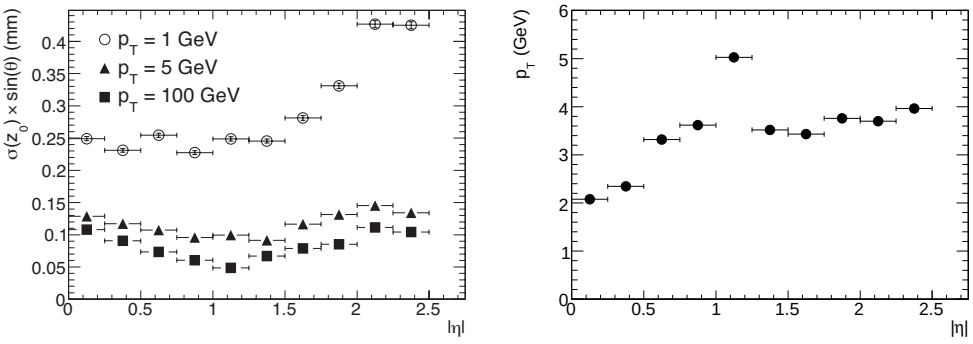

Figure 10.10: Modified longitudinal impact parameter, $z_0 \times \sin\theta$, resolution (left) as a function of $|\eta|$ for pions with $p_T = 1\,\text{GeV}$ (open circles), 5 GeV (full triangles) and 100 GeV (full squares). Transverse momentum, at which the multiple-scattering contribution equals the intrinsic resolution, as a function of $|\eta|$ (right).

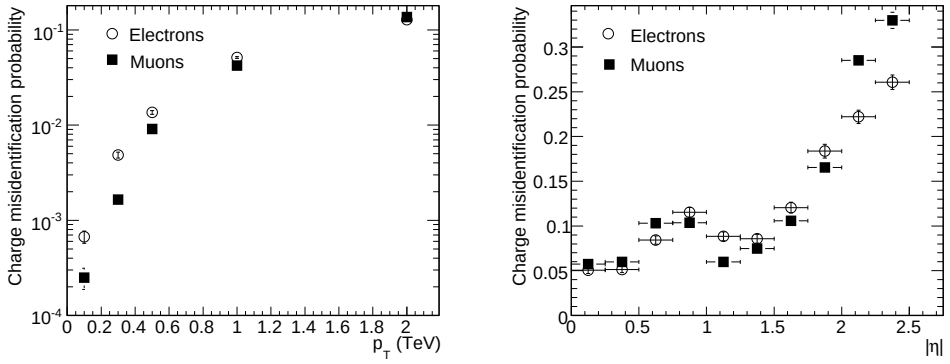

Figure 10.11: Charge misidentification probability for high energy muons and electrons as a function of p_T for particles with $|\eta| \leq 2.5$ (left) and as a function of $|\eta|$ for $p_T = 2$ TeV (right).

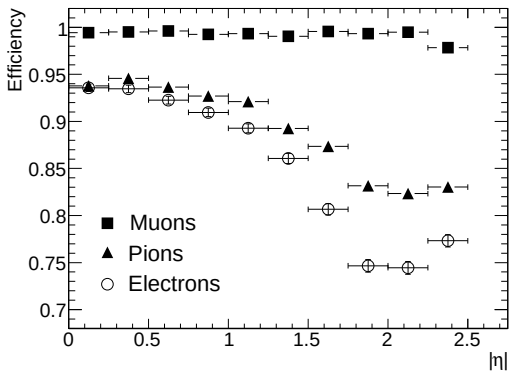

Figure 10.12: Track reconstruction efficiencies as a function of $|\eta|$ for muons, pions and electrons with $p_T = 5$ GeV. The inefficiencies for pions and electrons reflect the shape of the amount of material in the inner detector as a function of $|\eta|$.

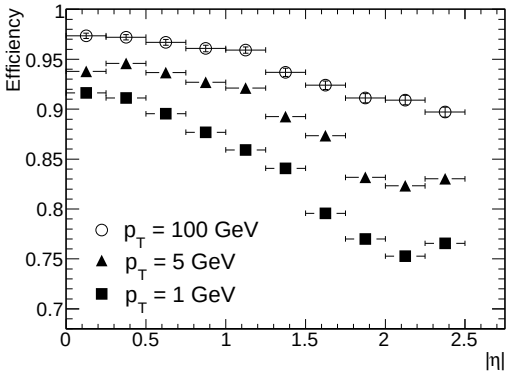

Figure 10.13: Track reconstruction efficiencies as a function of $|\eta|$ for pions with $p_T = 1$, 5 and 100 GeV.

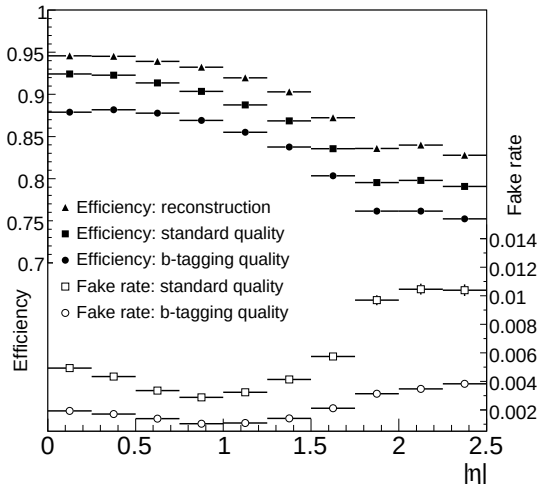

Figure 10.14: Track reconstruction efficiencies and fake rates as a function of $|\eta|$, for charged pions in jets in $t\bar{t}$ events and for different quality cuts (as described in the text). "Reconstruction" refers to the basic reconstruction before additional quality cuts.

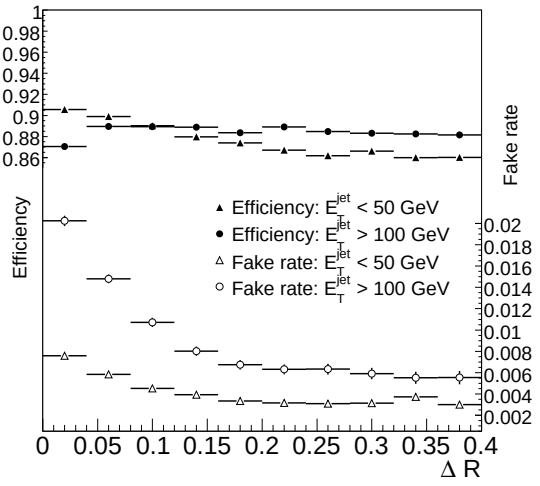

Figure 10.15: Track reconstruction efficiencies and fake rates as a function of the distance ΔR (defined as $\Delta R = \sqrt{\Delta\eta^2 + \Delta\phi^2}$) of the track to the jet axis, using the standard quality cuts and integrated over $|\eta| < 2.5$.

Figure 10.14 shows the track reconstruction efficiency for prompt pions (produced before the vertexing layer) and the fake rate for tracks in jets in $t\bar{t}$ events as a function of $|\eta|$. For these events, the mean jet p_T is 55 GeV, and the mean p_T of the accepted tracks which they contain is 4 GeV. The loss of efficiency at $|\eta| = 0$ with the b-tagging criteria arises from inefficiencies in the pixel vertexing layer, which are assumed here to be 1%; this improves at higher $|\eta|$, owing to the presence of larger clusters when the track incidence angle decreases. Beyond $|\eta| \sim 1$, the tracking performance deteriorates, mostly because of increased material. As shown in figure 10.15, the fake rate increases near the core of the jet, where the track density is the highest and induces pattern-recognition problems. This effect increases as the jet p_T increases. A few percent efficiency can be gained at the cost of doubling the fake rate in the jet core.

10.2.4 Vertexing performance

Vertexing tools constitute an important component of the higher-level tracking algorithms. The residuals of the primary vertex reconstruction are shown in figure 10.16, as obtained without using any beam constraint, for $t\bar{t}$ events and $H \to \gamma\gamma$ events with m_H = 110 GeV. The results shown here for $H \to \gamma\gamma$ events are based on tracks reconstructed from the underlying event and do not make use of the measurement of the photon direction in the electromagnetic calorimeter, which is discussed in section 10.4. The primary vertex in $t\bar{t}$ events has always a rather large multiplicity and includes a number of high-p_T tracks, resulting in a narrower and more Gaussian distribution than for $H \to \gamma\gamma$ events. Table 10.2 shows the resolutions of the primary vertex reconstruction in these $t\bar{t}$ and $H \to \gamma\gamma$ events, without and with a beam constraint in the transverse plane, as well as the

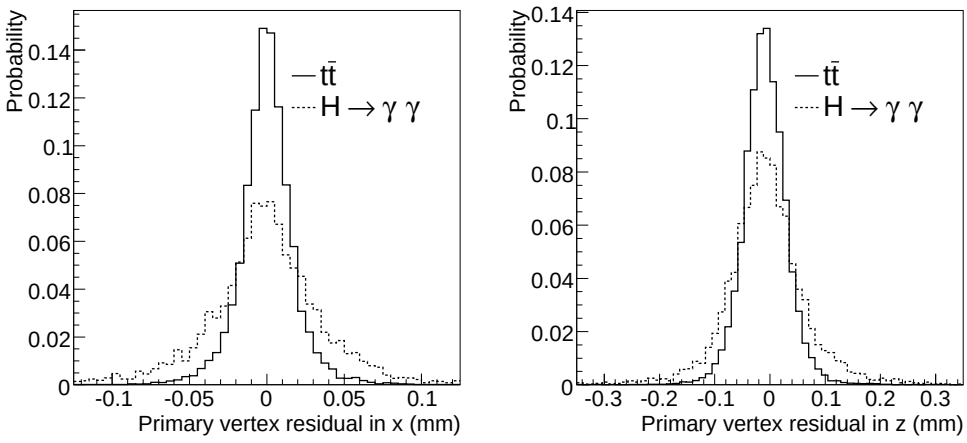

Figure 10.16: Primary vertex residual along x, in the transverse plane (left), and along z, parallel to the beam (right), for events containing top-quark pairs and $H \rightarrow \gamma\gamma$ decays with $m_H = 110\,\text{GeV}$. The results are shown without pile-up and without any beam constraint.

Table 10.2: Primary vertex resolutions (RMS), without and with a beam constraint in the transverse plane, for $t\bar{t}$ events and $H \rightarrow \gamma\gamma$ events with $m_H = 110\,\text{GeV}$ in the absence of pile-up. Also shown, in the presence of pile-up at a luminosity of 10^{33} cm^{-2} s^{-1}, are the efficiencies to reconstruct and then select the hard-scattering vertex within ± 300 μm of the true vertex position in z. The hard-scattering vertex is selected as the primary vertex with the largest Σp_T^2, summed over all its constituent tracks.

Event type	**x-y resolution (μm)**	**z resolution (μm)**	**Reconstruction efficiency (%)**	**Selection efficiency (%)**
$t\bar{t}$ (without beam constraint)	18	41	100	99
$t\bar{t}$ (with beam constraint)	11	40	100	99
$H \rightarrow \gamma\gamma$ (without beam constraint)	36	72	96	79
$H \rightarrow \gamma\gamma$ (with beam constraint)	14	66	96	79

efficiencies to reconstruct and select correctly these primary vertices in the presence of pile-up at a luminosity of 10^{33} cm^{-2} s^{-1} (the beam constraint in the transverse plane assumes the interactions occur at a fixed position with RMS of $\sim 15\,\mu$m).

The resolutions for the reconstruction of the radial position of secondary vertices for three-prong hadronic τ-decays in $Z \rightarrow \tau\tau$ events, with a mean p_T of 36 GeV for the τ-lepton, and for $J/\psi \rightarrow \mu\mu$ decays in events containing B-hadron decays, with a mean p_T of 15 GeV for the J/ψ, are shown respectively in figures 10.17 and 10.18. In the first more challenging example, the vertex resolutions are Gaussian in the central region, but have long tails as can be seen from the points showing 95% coverage in figure 10.17. Finally, figure 10.19 shows the resolution as a function of decay radius for the reconstruction of the radial position of secondary vertices for K_s^0 decays with mean p_T of 6 GeV in events containing B-hadron decays. The reconstruction is performed in three dimensions and hence requires at least two silicon hits. Consequently, the efficiency falls rapidly

2008 JINST 3 S08003

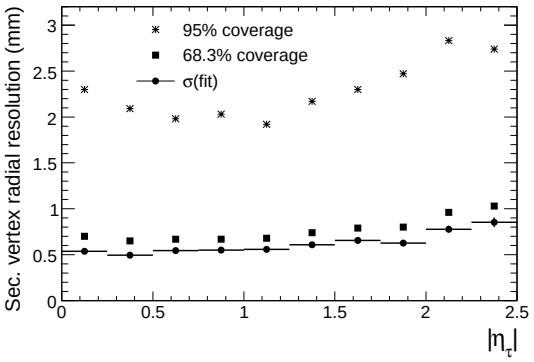

Figure 10.17: Resolution for the reconstruction of the radial position of the secondary vertex for three-prong hadronic τ-decays in $Z \rightarrow \tau\tau$ events, as a function of the pseudorapidity of the τ. The τ-leptons have an average visible transverse energy of 36 GeV. The distributions are fitted to a Gaussian core with width σ(fit). The fractions of events found within $\pm 1\ \sigma$ (68.3% coverage) and $\pm 2\ \sigma$ (95% coverage) are also shown.

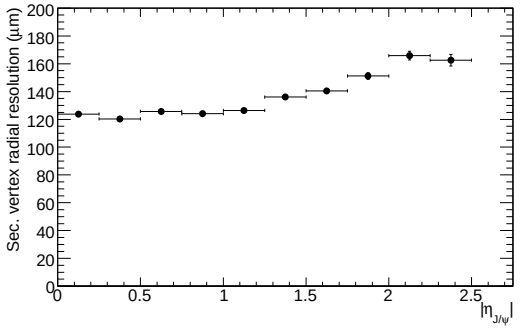

Figure 10.18: Resolution for the reconstruction of the radial position of the secondary vertex for $J/\psi \rightarrow \mu\mu$ decays in events containing B-hadron decays, as a function of the pseudorapidity of the J/ψ. The J/ψ have an average transverse momentum of 15 GeV.

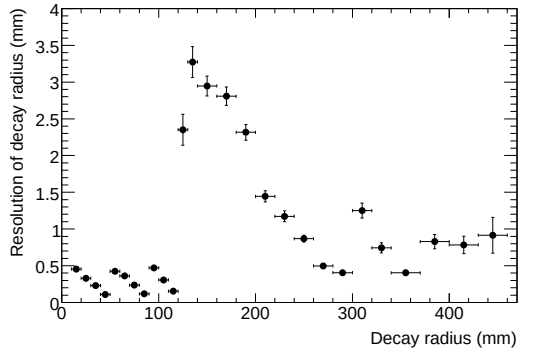

Figure 10.19: Resolution for reconstruction of radial position of secondary vertex for $K_s^0 \rightarrow \pi^+\pi^-$ decays in events containing B-hadron decays, as a function of the K_s^0 decay radius.

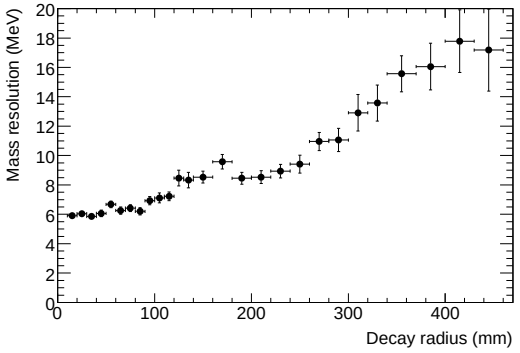

Figure 10.20: Resolution for reconstruction of the invariant mass of the charged-pion pair for $K_s^0 \rightarrow \pi^+\pi^-$ decays in events containing B-hadron decays, as a function of the K_s^0 decay radius.

for decay radii larger than 30 cm. The effect of crossing the three successive pixel layers is clearly visible as well as the degraded resolution for decays beyond the last pixel layer. Figure 10.20 shows the resolution as a function of decay radius for the reconstruction of the invariant mass of the charged-pion pair for the same $K_s^0 \rightarrow \pi^+\pi^-$ decays.

2008 JINST 3 S08003

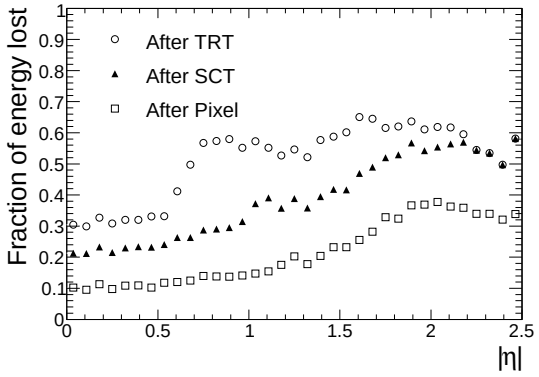

Figure 10.21: Fraction of energy lost on average by electrons with $p_T = 25\,\text{GeV}$ as a function of $|\eta|$, when exiting the pixel, the SCT and the inner-detector tracking volumes. The fraction of energy lost is not a strong function of the electron energy. For $|\eta| > 2.2$, there is no TRT material, hence the SCT and TRT lines merge.

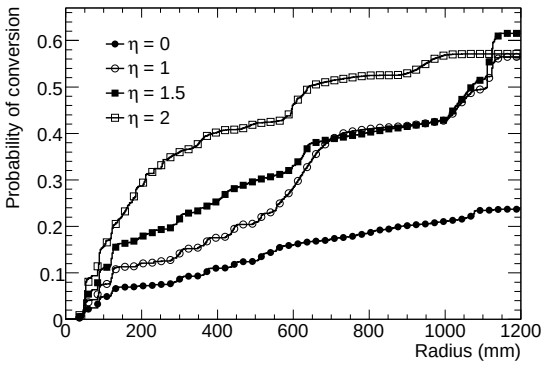

Figure 10.22: Probability for a photon to have converted as a function of radius for different values of $|\eta|$, shown for photons with $p_T > 1\,\text{GeV}$ in minimum-bias events. The probability is not a strong function of the photon energy.

10.2.5 Particle identification, reconstruction of electrons and photon conversions

The reconstruction of electrons and of photon conversions is a particular challenge for the inner detector, since electrons have lost on average between 20 and 50% of their energy (depending on $|\eta|$) when they leave the SCT, as illustrated in figure 10.21. In the same region, between 10% and 50% of photons convert into an electron-positron pair, as illustrated in figure 10.22.

The TRT plays a central role in electron identification, cross-checking and complementing the calorimeter, especially at energies below 25 GeV. In addition, the TRT contributes to the reconstruction and identification of electron track segments from photon conversions down to 1 GeV and of electrons which have radiated a large fraction of their energy in the silicon layers.

By fitting electron tracks in such a way as to allow for bremsstrahlung, it is possible to improve the reconstructed track parameters, as shown for $|\eta| > 1.5$ in figure 10.23 for two examples of bremsstrahlung recovery algorithms. These algorithms rely exclusively on the inner-detector information and therefore provide significant improvements only for electron energies below $\sim 25\,\text{GeV}$ (see section 10.4.2 for a discussion of bremsstrahlung recovery using also the position information of the electromagnetic calorimeter). The dynamic-noise-adjustment (DNA) method extrapolates track segments to the next silicon detector layer. If there is a significant χ^2 contribution, compatible with a hard bremsstrahlung, the energy loss is estimated and an additional noise term is included in the Kalman filter [254]. The Gaussian-sum filter (GSF) is a non-linear generalisation of the Kalman filter, which takes into account non-Gaussian noise by modelling it as a weighted sum of Gaussian components and therefore acts as a weighted sum of Kalman filters operating in parallel [255]. Figure 10.24 shows the improvements from bremsstrahlung recovery for the reconstructed $J/\psi \to ee$ mass. Without any bremsstrahlung recovery, only 50% of events are reconstructed within $\pm 500\,\text{MeV}$ of the nominal J/ψ mass, whereas with the use of the bremsstrahlung recovery, this fraction increases to approximately 60% for both algorithms.

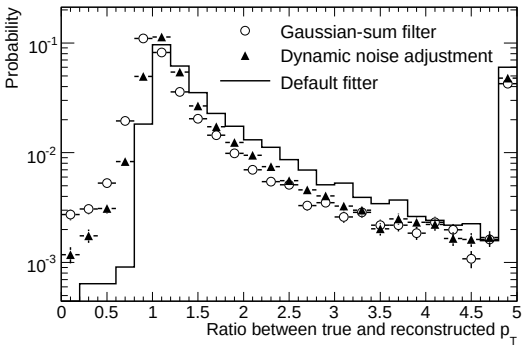

Figure 10.23: Probability distribution for the ratio of the true to reconstructed momentum for electrons with $p_T = 25\,\text{GeV}$ and $|\eta| > 1.5$. The results are shown as probabilities per bin for the default Kalman fitter and for two bremsstrahlung recovery algorithms (see text).

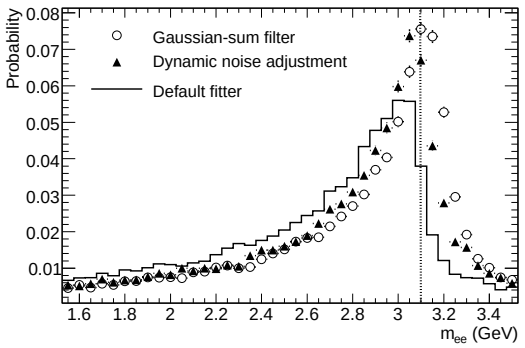

Figure 10.24: Probability for reconstructed invariant mass of electron pairs from $J/\psi \to ee$ decays in events with $B_d^0 \to J/\psi(ee)K_s^0$. The results are shown for the default Kalman fitter and for two bremsstrahlung recovery algorithms (see text). The true J/ψ mass is shown by the dotted line.

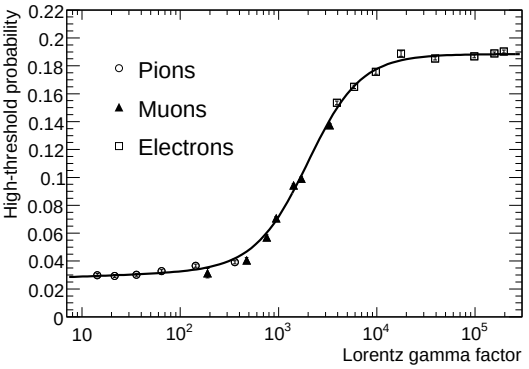

Figure 10.25: Average probability of a high-threshold hit in the barrel TRT as a function of the Lorentz γ-factor for electrons (open squares), muons (full triangles) and pions (open circles) in the energy range 2–350 GeV, as measured in the combined test-beam.

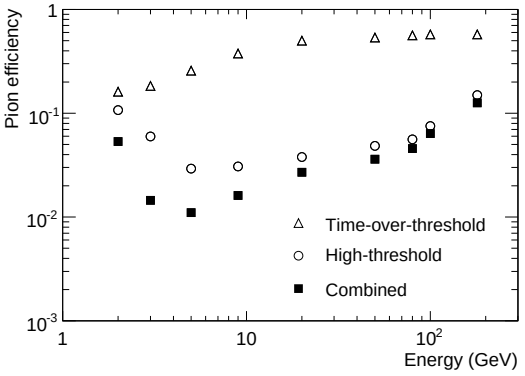

Figure 10.26: Pion efficiency shown as a function of the pion energy for 90% electron efficiency, using high-threshold hits (open circles), time-over-threshold (open triangles) and their combination (full squares), as measured in the combined test-beam.

Using pion, electron and muon samples in the energy range between 2 and 350 GeV, the barrel TRT response has been measured in the CTB in terms of the high-threshold hit probability, as shown in figure 10.25. The transition-radiation X-rays contribute significantly to the high-threshold hits for electron energies above 2 GeV and saturation sets in for electron energies above 10 GeV. Figure 10.26 shows the resulting pion identification efficiency for an electron efficiency of 90%, achieved by performing a likelihood evaluation based on the high-threshold probability for electrons and pions for each straw. Figure 10.26 also shows the effect of including time-over-threshold information, which improves the pion rejection by about a factor of two when combined with

2008 JINST 3 S08003

the high-threshold hit information. At low energies, the pion rejection (the inverse of the pion efficiency plotted in figure 10.26) improves with energy as the electrons emit more transition radiation. The performance is optimal at energies of ~ 5 GeV, and pion-rejection factors above 50 are achieved in the energy range of 2–20 GeV. At very high energies, the pions become relativistic and therefore produce more δ-rays and eventually emit transition radiation, which explains why the rejection slowly decreases for energies above 10 GeV.

The electron-pion separation expected for the TRT in ATLAS, including the time-over-threshold information, is shown as a function of $|\eta|$ in figure 10.27 as the pion identification efficiency expected for an electron efficiency of 90%. The shape observed is closely correlated to the number of TRT straws crossed by the track, which decreases from approximately 35 to a minimum of 20 in the transition region between the barrel and end-cap TRT, $0.8 < |\eta| < 1.1$, and which also decreases rapidly at the edge of the TRT fiducial acceptance for $|\eta| > 1.8$. Because of its more efficient and regular foil radiator, the performance in the end-cap TRT is better than in the barrel TRT (see section 4.3.3).

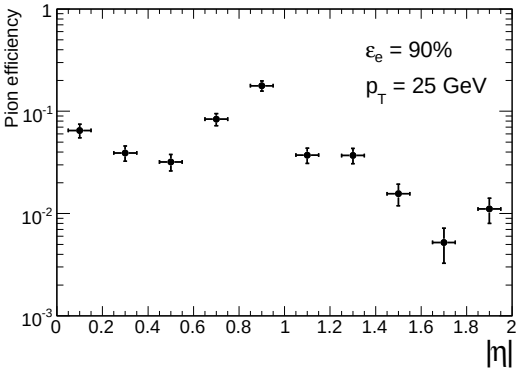

Figure 10.27: Expected pion efficiency as a function of $|\eta|$ for an efficiency of 90% for electrons with $p_T = 25$ GeV.

Figure 10.28 shows the efficiency for reconstructing conversions of photons with $p_T = 20$ GeV and $|\eta| < 2.1$ as a function of the conversion radius, using the standard tracking algorithm combined with the back-tracking algorithm described in section 10.2.1. At radii above 50 cm, the efficiency for reconstructing single tracks drops and that for reconstructing the pair drops even faster because the two tracks are merged. If both tracks from the photon conversion are reconstructed successfully, vertexing tools can be used to reconstruct the photon conversion with high efficiency up to radii of 50 cm. The overall conversion-finding efficiency can be greatly increased at large radii by defining single tracks as photon conversions under certain conditions. Only tracks which have no hits in the vertexing layer, are not associated to any fitted primary or secondary vertex, and pass a loose electron identification cut requiring more than 9% high-threshold hits on the TRT segment of the track, are retained. The resulting overall efficiency for finding photon conversions is almost uniform over all radii below 80 cm, as shown in figure 10.29.

10.3 Muon reconstruction and identification

10.3.1 Introduction

The collisions at the LHC will produce a broad spectrum of final-state muons, ranging from low-momentum non-isolated muons in b-jets to high-momentum isolated muons from W/Z-boson decays or from possible new physics. The experiment will detect and measure muons in the muon spectrometer and will also exploit the measurements in the inner detector and the calorimeters

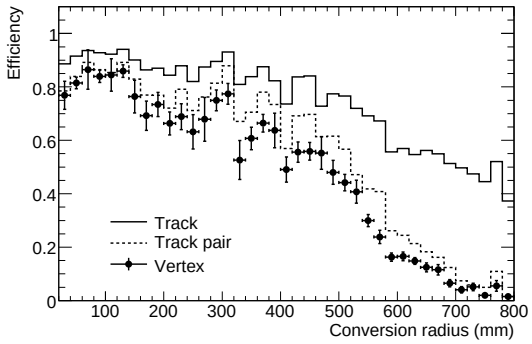

Figure 10.28: Efficiency to reconstruct conversions of photons with p_T = 20 GeV and $|\eta| < 2.1$, as a function of the conversion radius. Shown are the efficiencies to reconstruct single tracks from conversions, the pair of tracks from the conversion and the conversion vertex. The errors are statistical.

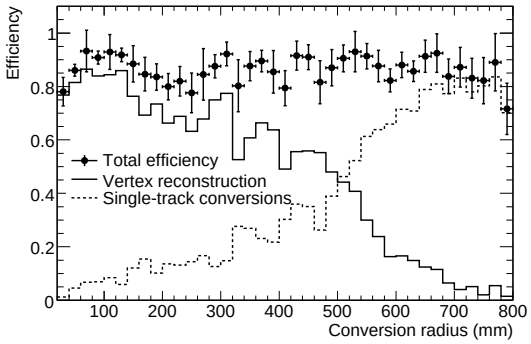

Figure 10.29: Efficiency to identify conversions of photons with p_T = 20 GeV and $|\eta| < 2.1$, as a function of the conversion radius. The overall efficiency is a combination of the efficiency to reconstruct the conversion vertex, as shown also in figure 10.28, and of that to identify single-track conversions (see text). The errors are statistical.

to improve the muon identification efficiency and momentum resolution. Muon measurements are a combination of accurate measurements in the muon spectrometer and in the inner detector. The muon spectrometer also efficiently triggers on muons over a wide range of energies and over $|\eta| < 2.4$. as described in detail in section 6.6 for the detectors and in section 10.9 for the actual trigger performance. The inner detector provides the best measurement at low to intermediate momenta, whereas the muon spectrometer takes over above 30 GeV. The toroidal field guarantees excellent momentum resolution even at the highest values of η (see section 2.2.3.2 and figure 2.12 for details about the mapping of the toroidal field).

This section describes the alignment results obtained in the combined test-beam (CTB), which have validated the overall alignment strategy for both the barrel and end-cap muon-chamber systems, and the expected muon reconstruction performance in terms of momentum resolution, track-finding efficiency and mass resolution for selected channels.

10.3.2 Calibration and alignment

In order to achieve the required performance for combined muon reconstruction, the inner detector and the muon spectrometer must be calibrated and aligned internally and with respect to each other. The alignment of the inner detector is described in section 10.2.2.

In the muon spectrometer, movements of most of the precision chambers (MDT and CSC) are monitored by a system of optical sensors with an accuracy of a few micrometres (see section 6.5). In principle, the optical system alone should provide the chamber positions with an accuracy such that the alignment contribution to the error on the sagitta measurement does not exceed 40 μm. Muon tracks, however, are required to align the chambers with no (or poor) optical connection, to align the end-caps with respect to the barrel, and to align the muon spectrometer with respect to the inner detector with an accuracy of approximately 200 μm in z and 1 mm in $R\phi$.

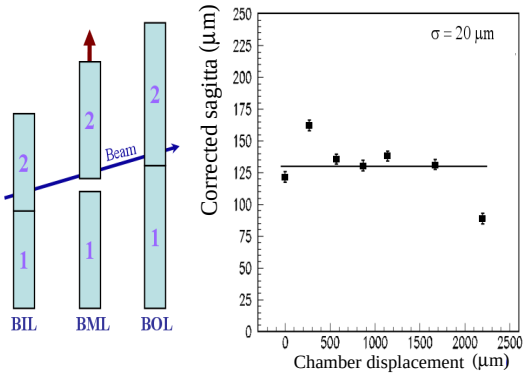

Figure 10.30: Sagitta measurement in the muon combined test-beam barrel sector set-up as a function of the value of systematic displacements of the middle barrel chamber in the direction indicated by the sketch.

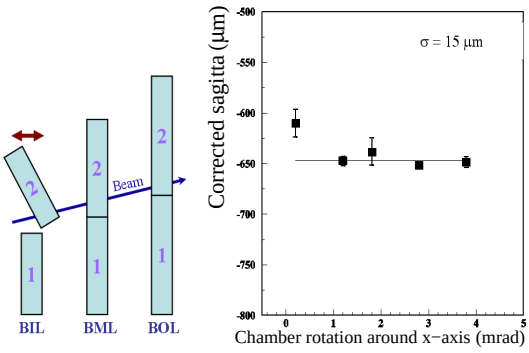

Figure 10.31: Sagitta measurement in the muon combined test-beam barrel sector set-up as a function of the value of systematic rotations of the inner barrel chamber around the axis indicated by the sketch (x-axis parallel to the drift tubes).

10.3.2.1 Performance of optical alignment system in test-beam

The optical alignment concept for the muon spectrometer underwent a final round of testing and validation with one full barrel sector and one full end-cap sector in the H8 muon beam line at CERN in 2002-2004 (see figures 10.1 and 10.3). Figures 10.30 and 10.31 show as examples the measured track sagittas, after applying the corrections obtained from the optical alignment system, for a specific displacement of the middle chamber of the barrel sector and for a specific rotation of the inner chamber of the barrel sector, respectively. Alignment accuracies of approximately 20 μm have been achieved in these tests, well within the design specifications of the alignment system (see section 6.5) [194, 195, 262, 263].

10.3.2.2 Alignment of the muon spectrometer with tracks

In the muon spectrometer (see section 6.3.2 and table 6.3), some chambers are not optically linked (BIS.8, BEE), or the optical connection does not have the required precision for the sagitta measurement (barrel chambers of the small sectors). During normal data-taking, these chambers can be aligned precisely using muon tracks passing through overlap regions with the optically aligned neighbouring chambers. Similarly, the alignment of the two end-caps with respect to the barrel will use tracks fully reconstructed in the barrel and passing through one end-cap chamber: one example of such an overlap is that between BIS-EIL-BML-BOL.

As an additional independent test of the achieved alignment accuracy, it is foreseen to run for some short periods without magnetic field in the toroids, while the solenoid is at full field. This will yield straight tracks in the muon spectrometer, which can be selected to have e.g. $p_T > 10$ GeV, using the matching track reconstructed in the inner detector to limit the impact of multiple scattering. If the chamber alignment were perfect, the measured sagittas would be centred around zero with

2008 JINST 3 S08003

a variance determined by multiple scattering and the position resolution of the chambers. Significant deviations from zero in certain η-ϕ regions would point to errors of chamber positioning, as obtained from the optical alignment. A statistical accuracy of 30 μm on the average sagitta can be obtained with 15000 tracks with $p_T > 10$ GeV per chamber triplet. This corresponds to a less than one day of data-taking at a luminosity of 10^{33} cm^{-2} s^{-1}. A similar procedure can be used during cosmic-ray data-taking to align parts of the spectrometer independently of LHC operation.

10.3.2.3 Overall calibration and alignment strategy

The drift-time measurements of the MDT's are synchronised with an accuracy of 200 ps by measuring the minimum drift time from the raw drift-time spectra of the individual tubes. The space-to-drift-time relationships, *R-t*, are iteratively determined from the residuals of reconstructed muon track segments in the chambers. The required *R-t* accuracy of 20 μm can be achieved with 2000 track segments per chamber.

Both the alignment constants obtained from tracks and the MDT calibrations will be produced on a daily basis and will have to be ready within 24 hours to be used in the reconstruction. In order to collect enough statistics for these tasks, a dedicated stream of high-p_T single muons will be provided at a rate of 1 kHz as a direct output of the L2 muon trigger [174].

10.3.3 Reconstruction strategies

Muons with momenta ranging from approximately 3 GeV to 3 TeV are identified and measured with optimal acceptance and efficiency through the use of a combination of three track-reconstruction strategies (see section 10.2.1 for a brief description of the tracking software common to inner-detector and muon-spectrometer reconstruction):

- Stand-alone: muon track reconstruction based solely on the muon spectrometer data over the range $|\eta| < 2.7$ (defined by the spectrometer acceptance).
- Combined: combination of a muon-spectrometer track with an inner-detector track over the range $|\eta| < 2.5$ (defined by the inner-detector acceptance).
- Segment tag: combination of an inner-detector track with a muon-spectrometer segment, i.e. a straight-line track, in an inner muon station.

Track reconstruction in the muon spectrometer is logically sub-divided into the following stages: pre-processing of raw data to form drift-circles in the MDT's or clusters in the CSC's and the trigger chambers (RPC's and TGC's), pattern-finding and segment-making, segment-combining, and finally track-fitting. Track segments are defined as straight lines in a single MDT or CSC station. The search for segments is seeded by a reconstructed pattern of drift-circles or clusters or by drift-circles or clusters lying in a region of activity, which is defined by the trigger chambers and has a size of the order of 0.4×0.4 in $\eta - \phi$ space.

Full-fledged track candidates are built from segments, starting from the outer and middle stations and extrapolating back through the magnetic field to the segments reconstructed in the other stations. Each time a reasonable match is found, the segment is added to the track candidate.

2008 JINST 3 S08003

The final track-fitting procedure takes into account, in full detail, the geometrical description of the traversed material and the magnetic field inhomogeneities along the muon trajectory.

The muon-spectrometer track parameters are determined at the inner stations, which yield the first set of measurements in the muon spectrometer. The track is then propagated back to the interaction point and the momentum is corrected for the energy loss in the calorimeters (and in the inner detector). The energy lost by dE/dX in the calorimeters is estimated by an algorithm, which uses either the parametrised expected energy loss or the measured calorimeter energy. The measured energy is used only if it exceeds significantly the most probable energy loss and if the muon track is isolated.

The combination of the stand-alone tracks reconstructed in the muon spectrometer with tracks reconstructed in the inner detector is performed in the region $|\eta| < 2.5$, which corresponds to the geometrical acceptance of the inner detector. This combination will considerably improve the momentum resolution for tracks with momenta below 100 GeV, but will also suppress to a certain extent backgrounds from pion punch-through and from pion or kaon decays in flight.

In the case of segment tags, inner-detector tracks are extrapolated to the inner muon stations and either associated directly to reconstructed muon segments or used to select muon drift-circles and clusters in a cone with typically a size of 100 mrad, from which track segments are then reconstructed. The muons reconstructed through this procedure provide an important improvement to the stand-alone muon reconstruction for three main reasons:

- at momenta below typically 6 GeV, muon tracks do not always reach the middle and outer muon stations;
- in the barrel/end-cap transition region with $1.1 < |\eta| < 1.7$, the middle stations are missing for the initial data-taking (EES and EEL chambers in table 6.4) and the stand-alone reconstruction efficiency is reduced in this region;
- in the difficult regions at $\eta \approx 0$ and in the feet, the geometrical acceptance of the muon stations is considerably reduced.

10.3.4 Muon reconstruction performance for single muons

Three main quantities can be used to summarise the performance of the muon reconstruction and identification algorithms: the momentum resolution, the efficiency and the misidentification or fake rate. This section presents the expected performance of the three first strategies described above for single muons. Both the stand-alone and combined results shown here have been obtained using as an example the algorithms described in ref. [264]. Except where directly relevant to the performance (e.g. for estimates of the fake rates), the results presented here do not include any effects arising from cavern background or pile-up.

Figure 10.32 shows the expected fractional momentum resolution, averaged over ϕ, for single muons with $p_T = 100$ GeV, as obtained for stand-alone and combined muon tracks. Over a large fraction of the acceptance, the stand-alone resolution is close to 3%, as shown in more detail in figure 10.33, which shows its variation as a function of ϕ in the region $0.3 < |\eta| < 0.65$. One clearly sees the degradation in resolution due to the feet which support the experiment and are situated close to $\phi = 240^\circ$ and 300°. In the region $1.1 < |\eta| < 1.7$, the large degradation of

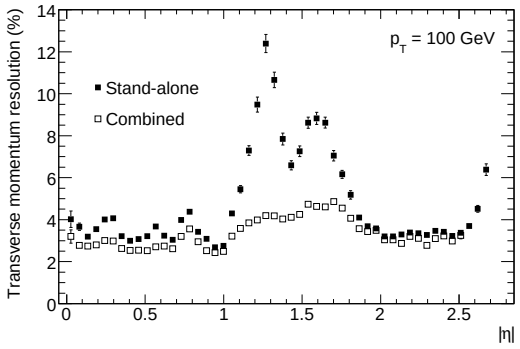

Figure 10.32: For muons with $p_T = 100\,\text{GeV}$, expected fractional momentum resolution as a function of $|\eta|$ for stand-alone and combined reconstruction. The degradation in the region with $1.1 < |\eta| < 1.7$ is due to the absence of the middle muon stations in the barrel/end-cap transition region for the initial data-taking, to the low bending power of the magnetic field in the transition region between the barrel and end-cap toroids and to the material of the coils of the end-cap toroids.

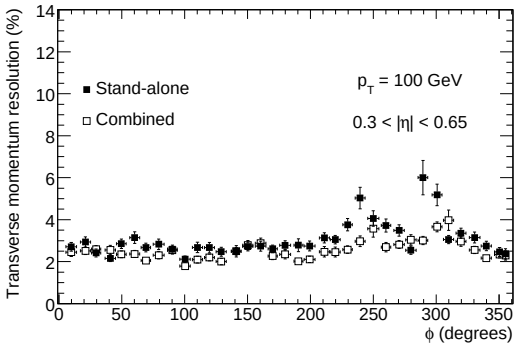

Figure 10.33: For muons with $p_T = 100\,\text{GeV}$, expected fractional momentum resolution as a function of ϕ for stand-alone and combined reconstruction. The resolution is degraded at $\phi = 240^\circ$ and 300°, due to the additional material introduced by the feet which support the barrel part of the detector.

the stand-alone momentum resolution is due to several effects. In the region $1.1 < |\eta| < 1.3$, the degradation is due to the absence of the middle muon stations in the barrel/end-cap transition region for the initial data-taking, which results in a large degradation of the resolution since the measurement is limited to an angle-angle measurement between the inner and outer stations. At larger values of $|\eta|$, the degradation is due to the combination of the low bending power of the magnetic field in the transition region between the barrel and end-cap toroids and of the large amount of material in the coils of the end-cap toroid in limited regions in ϕ. The contribution of the inner detector to the combined resolution is therefore more important in this η-region. In the barrel region, the contribution of the inner detector remains significant, whereas it basically vanishes for $|\eta| > 2.0$. This is due to the intrinsically worse momentum resolution in the inner detector because of the absence of any TRT measurements in this η-region, of the solenoidal field non-uniformity, and of the shorter length of the tracks in the inner-detector magnetic volume.

The stand-alone momentum resolution of muons with $p_T = 100\,\text{GeV}$ can be calculated based on the spatial resolution of the chambers, the material distribution, and the magnetic-field configuration in the muon spectrometer [265]. The result of this calculation is shown as a function of ϕ and $|\eta|$ in figure 10.34. No momentum measurement is possible at $|\eta| < 0.1$ and $|\eta| = 1.3$ because of holes in the acceptance of the muon spectrometer. The expected stand-alone momentum resolution is approximately 3% over most of the $\eta - \phi$ plane. It is degraded to 5% at $|\eta| = 0.2$, 0.3 and 0.7, due to support structures of the barrel toroid magnet coils. The degradation in the regions corresponding to $1.2 < |\eta| < 1.7$ and to ϕ-values which are multiples of 22.5° is caused by the

2008 JINST 3 S08003

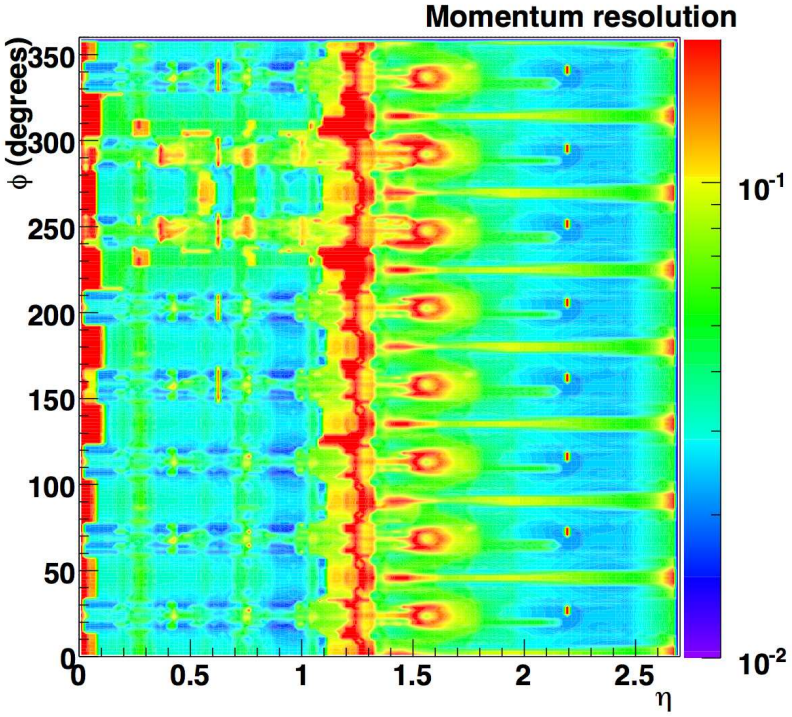

Figure 10.34: For muons with p_T = 100 GeV, expected fractional stand-alone momentum resolution as a function of ϕ and $|\eta|$. The results are based on a parametrisation using the material distribution in the muon spectrometer shown in figure 6.7, the magnetic field configuration in the muon spectrometer, and the spatial resolution of the muon chambers. No momentum measurement is possible at $|\eta| < 0.1$ over most of the azimuth, nor at $|\eta| = 1.3$ because of holes in the acceptance of the muon spectrometer (see text).

small bending power of the magnetic field in these regions. The resolution expectations from this analytical model are in good agreement with the results shown in figures 10.32 and 10.33, which are based on full simulation and reconstruction.

Figures 10.35 and 10.36 show the expected stand-alone and combined momentum resolutions as a function of p_T, excluding the η-region $1.1 < |\eta| < 1.7$, respectively for the barrel and end-cap muon spectrometer. The stand-alone resolution displays its characteristic behaviour with optimal resolution achieved at $\sim$ 100 GeV. At lower transverse momenta, the stand-alone resolution is dominated by fluctuations in the energy loss in the calorimeters, whereas at higher transverse momenta, it is dominated by the intrinsic MDT tube accuracy, assumed to be 80 μm in the case of a calibrated and aligned detector. At low transverse momenta, the combined resolution reflects directly the dominant performance of the inner detector, which is itself limited by multiple scattering for transverse momenta below $\sim$ 10 GeV (see section 10.2.3).

In figures 10.37 and 10.38, the single muon reconstruction efficiency is shown, respectively as a function of $|\eta|$ for muons with p_T = 100 GeV and as a function of p_T. The efficiency is defined as the fraction of simulated muons which are reconstructed within a cone of size ΔR = 0.2 of the

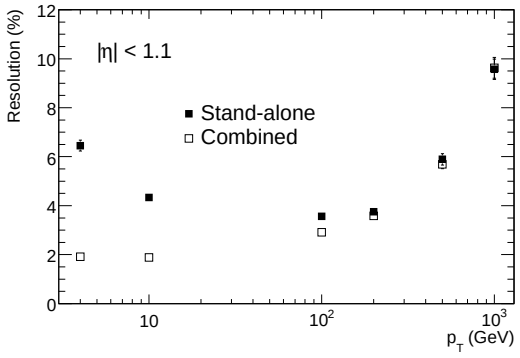

Figure 10.35: Expected stand-alone and combined fractional momentum resolution as a function of p_T for single muons with $|\eta| < 1.1$.

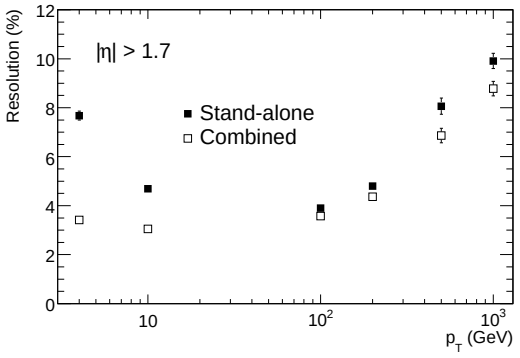

Figure 10.36: Expected stand-alone and combined fractional momentum resolution as a function of p_T for single muons with $|\eta| > 1.7$.

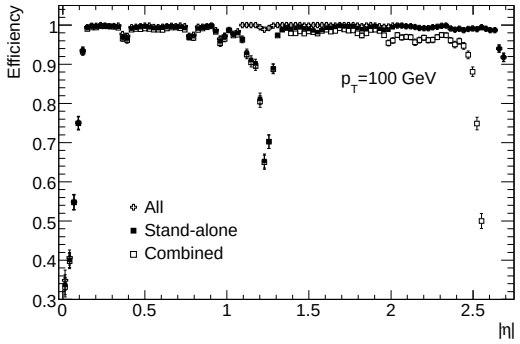

Figure 10.37: Efficiency for reconstructing muons with $p_T = 100\,\text{GeV}$ as a function of $|\eta|$. The results are shown for stand-alone reconstruction, combined reconstruction and for the combination of these with the segment tags discussed in the text.

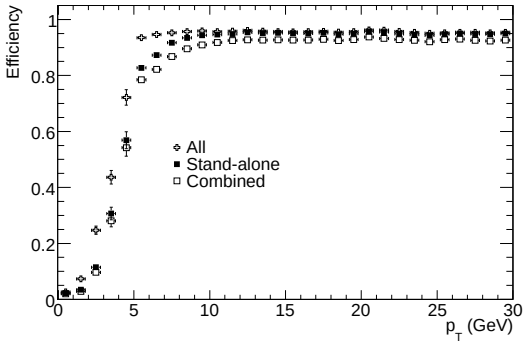

Figure 10.38: Efficiency for reconstructing muons as a function of p_T. The results are shown for stand-alone reconstruction, combined reconstruction and for the combination of these with the segment tags discussed in the text.

initial muon. The results are shown for stand-alone reconstruction, for combined reconstruction, and for the overall combination of these with the segment tags discussed above. The efficiency for stand-alone tracks drops to very low values in the region with $\eta \sim 0$ because of the large gap for services, in which there are very few muon stations. The stand-alone efficiency also drops substantially close to $\eta = 1.2$, which corresponds to a region in the barrel/end-cap transition region where several stations are missing. The efficiency for combining stand-alone muon tracks with the inner detector is very high in the central region, starts to drop for $|\eta| > 2.0$ and decreases rapidly to 0 for $|\eta| > 2.4$. The segment tags contribute only to a limited extent to the overall efficiency for $1.4 < |\eta| < 2.0$ for muons with high p_T, but figure 10.38 shows that, as expected, their contribution is substantial for lower p_T values.

The efficiencies presented above must be compared to the expected fake rates, especially in the presence of cavern background, which permeates the whole muon spectrometer, and of pile-up, which affects mostly the high-$|\eta|$ region. Electromagnetic showers triggered by energetic muons traversing the calorimeters and support structures lead to low-momentum electron and positron tracks, which accompany the muons in the muon spectrometer. These low-momentum tracks are an irreducible source of fake stand-alone muons. Most of them can be rejected by a cut on their transverse momentum. For example, a cut requiring $p_T > 5\,\text{GeV}$ reduces the fake rate to a few percent per triggered event. Such fakes can be almost entirely rejected by requiring a match of the muon-spectrometer track with an inner-detector track.

The second source of fake stand-alone muons is the background of thermal neutrons and low-energy γ-rays in the muon spectrometer (the so-called "cavern background"). Most of these fakes also have transverse momenta smaller than 5 GeV. The expected fake rate with $p_T > 5\,\text{GeV}$ from cavern background at 10^{33} cm^{-2} s^{-1} is below 2% per triggered event. This rate is proportional to the background counting rate and can be reduced by almost an order of magnitude by requiring a match of the muon-spectrometer track with an inner-detector track.

10.3.5 Reconstruction of $Z \rightarrow \mu\mu$ and $H \rightarrow \mu\mu\mu\mu$ decays

The large expected rates of $Z \rightarrow \mu\mu$ decays provide an excellent tool to untangle various effects which might lead to distortions of the measured dimuon invariant mass spectrum. One example is shown in figure 10.39 for stand-alone muon measurements, where the performance obtained with a misaligned layout is compared to that expected from a perfectly aligned layout. The misalignments introduced for this study were random displacements of typically 1 mm and random rotations of typically 1 mrad. These lead to a distribution of the difference between the dimuon reconstructed invariant mass and the true dimuon mass with a fitted Gaussian resolution of approximately 8 GeV. The fitted Gaussian resolution obtained for the same distribution in the case of the perfectly aligned layout is 2.5 GeV.

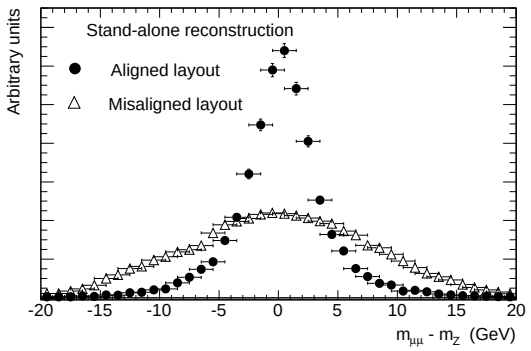

Figure 10.39: For stand-alone muon reconstruction, reconstructed invariant mass distribution of dimuons from $Z \rightarrow \mu\mu$ decays for an aligned layout of the chambers and for a misaligned layout, where all chambers are displaced and rotated randomly by typically 1 mm and 1 mrad.

The muon reconstruction and identification efficiency will also be measured from data using $Z \rightarrow \mu\mu$ decays and the tag-and-probe method described in section 10.9.7 with similar results in terms of accuracy of the measurement. These in situ measurements will be extended to lower-mass resonances, using J/ψ and Υ decays at lower initial luminosities.

Finally, figures 10.40 and 10.41 show the four-muon invariant mass distributions from respectively stand-alone and combined reconstruction without using any Z-mass constraint for $H \rightarrow \mu\mu\mu\mu$ decays in the case of a Higgs-boson mass of 130 GeV. The stand-alone resolution is 3.3 GeV, whereas the combined resolution is 2.1 GeV. The non-Gaussian tails in the distribution

2008 JINST 3 S08003

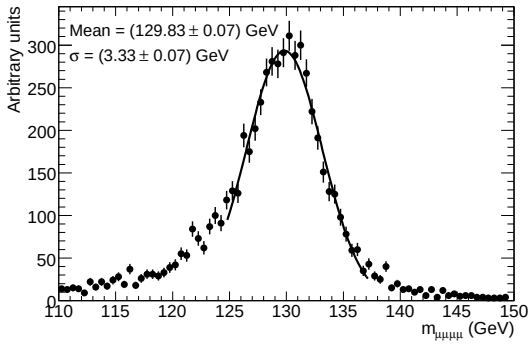

Figure 10.40: For $H \rightarrow \mu\mu\mu\mu$ decays with $m_H = 130\,\text{GeV}$, reconstructed mass of the four muons using stand-alone reconstruction. The results do not include a Z-mass constraint.

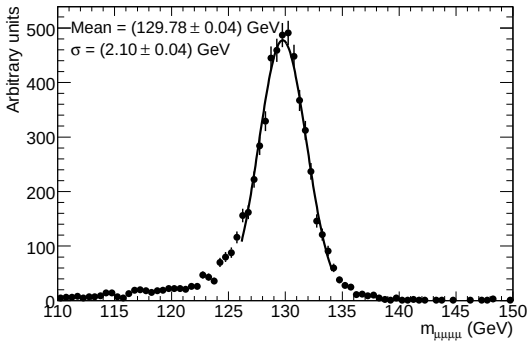

Figure 10.41: For $H \rightarrow \mu\mu\mu\mu$ decays with $m_H = 130\,\text{GeV}$, reconstructed mass of the four muons using combined reconstruction. The results do not include a Z-mass constraint.

amount to 29% (resp. 18%) of events which lie further than 2σ away from the peak for the stand-alone (resp. combined) reconstruction. They are partially due to radiative decays, but mostly to muons poorly measured in certain regions of the muon spectrometer, especially in the case of the stand-alone measurements.

10.4 Electrons and photons

Efficient and accurate reconstruction and identification of electrons and photons will be a task of unprecedented difficulty at the LHC, where the ratios of inclusive electrons and photons to jets from QCD processes are expected to be between one and two orders of magnitude worse than at the Tevatron (as an example, the electron-to-jet ratio is expected to be $\sim 10^{-5}$ at $p_T = 40\,\text{GeV}$). In addition, the large amount of material in front of the electromagnetic calorimeters and the harsh operating conditions at the LHC design luminosity provide a difficult challenge in terms of preserving most of the electrons and photons with their energies and directions measured as well as would be expected from the intrinsic performance of the electromagnetic calorimeters measured in test-beams. This section is devoted to a summary of the calibration and expected performance of the electromagnetic calorimeter, of electron and photon identification in the energy range of interest for initial physics, and of the strategies under evaluation for the validation and certification of the performance in situ.

10.4.1 Calibration and performance of the electromagnetic calorimeter

The results presented in this section are based on detailed simulation studies, validated by extensive test-beam studies over the past years (see section 5.7) and using reconstruction procedures developed for test-beam data analysis. Compared to ref. [248], the material budget in front of the calorimeter has increased substantially. The large amount of material in front of the presampler and the electromagnetic calorimeter leads to substantial energy losses for electrons, as shown in figure 10.42 (see also figure 10.21 for more details on electron energy loss in the inner-detector

2008 JINST 3 S08003

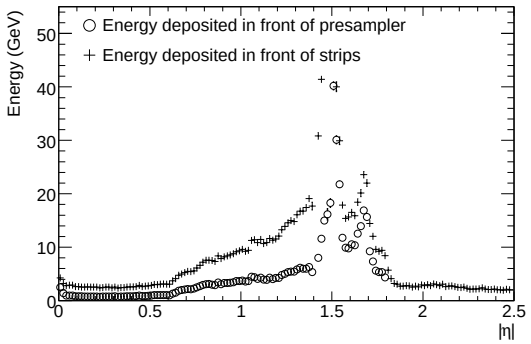

Figure 10.42: Average energy loss in GeV as a function of $|\eta|$ for electrons with an energy of 100 GeV. The results are shown before the presampler (open circles) and the strip layer (crosses).

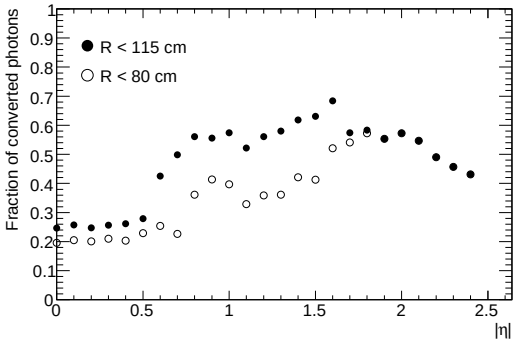

Figure 10.43: Fraction of photons converting at a radius of below 80 cm (115 cm) in open (full) circles as a function of $|\eta|$.

material itself) and to a large fraction of photons converting, as shown in figure 10.43 (see also figure 10.22 for details on the photon conversion probability in the inner-detector material).

Electron and photon reconstruction is seeded using a sliding-window algorithm with a window size corresponding to 5×5 cells in the middle layer of the electromagnetic calorimeter (see table 1.3 for a detailed description of the granularity and η-coverage of the electromagnetic calorimeter). A cluster of fixed size is then reconstructed around this seed. For electrons, the energy in the barrel electromagnetic calorimeter is collected over an area corresponding to 3×7 cells in the middle layer or 0.075×0.175 in $\Delta\eta \times \Delta\phi$. This choice optimises the balance between the conflicting requirements of collecting all the energy even in the case of hard bremsstrahlung and of preserving the energy resolution by minimising the contributions from noise and pile-up. For unconverted photons, adequate performance is obtained by limiting the area to 3×5 cells in the middle layer, whereas converted photons are treated like electrons. Finally, for the end-cap electromagnetic calorimeters, an optimal area of 5×5 cells in layer 2 has been chosen for both electrons and photons.

Position corrections are applied as a first step in the precise reconstruction of the electromagnetic cluster. Corrections for modulations of the local energy response as a function of the extrapolated impact point of the electron in both η and ϕ are shown in figures 10.44 and 10.45, respectively. These corrections do not modify the global energy scale and are rather small in terms of the relative response: typically, the η-variation is, minimum to maximum, around 1%, whereas the ϕ-modulation correction due to the accordion structure of the absorbers is, minimum to maximum, around 0.4%. The parabolic component of this latter correction is smaller than the one in η because of the energy sharing between adjacent cells in ϕ.

The most important corrections to optimise at the same time the energy resolution and the linearity of the response are incorporated using η-dependent longitudinal weights, similarly to what is described for the electromagnetic calorimeter test-beam results in section 5.7.1:

$$E = s(\eta)[c(\eta) + w_0(\eta) \cdot E_{\text{PS}} + E_{\text{strips}} + E_{\text{middle}} + w_3(\eta) \cdot E_{\text{back}}], \tag{10.1}$$

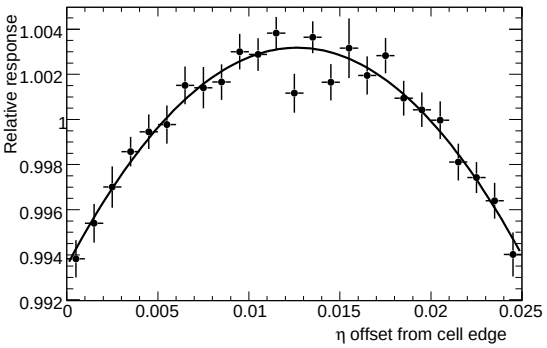

Figure 10.44: Electron energy response modulation as a function of the η offset within the cell. The curve represents a fit to the points used to parametrise the correction.

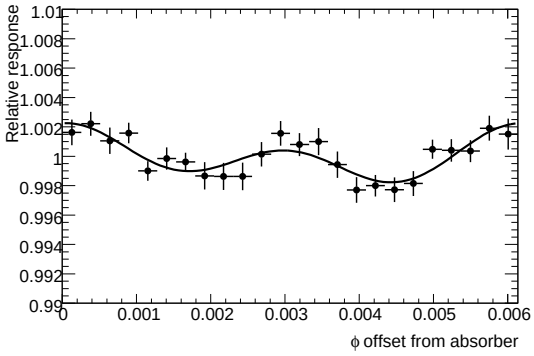

Figure 10.45: Electron energy response modulation as a function of the ϕ offset from the absorber. The curve represents a fit to the points used to parametrise the correction.

where s is an overall scale factor, c is an offset, w_0 corrects for energy losses upstream of the presampler, and w_3 corrects for longitudinal leakage, while E_{PS}, E_{strips}, E_{middle} and E_{back} represent the energies measured in the successive layers of the electromagnetic calorimeter (presampler, strips, middle and back). The weights are determined as functions of $|\eta|$, using simulated single-particle events (electrons and photons) with energies from 5 GeV to 200 GeV. The weights are calculated separately for electrons (matched track required) and photons (no matched track required) and applied to the corresponding cluster energies. In the future, this method will be replaced by a more complex algorithm, which corrects the different types of true energy loss one by one, by correlating each of them with measured observables.

In figures 10.46 and 10.47, the energy response, plotted as the difference between measured and true energy divided by the true energy, is shown for electrons with an energy of 100 GeV and for two illustrative η-values in the barrel electromagnetic calorimeter. The central value of the energy is reconstructed with excellent precision ($\sim 3 \times 10^{-4}$) if one assumes perfect knowledge of the material in front of the calorimeter. Both the Gaussian core and the non-Gaussian component of the tail of the energy distribution are significantly worse at the point with the larger η due to the larger amount of material in front of the calorimeter (see figure 4.46). As shown in figures 10.48 and 10.49, the resolution and non-Gaussian tails are better for photons than for electrons, but are somewhat worse for all photons than for unconverted photons, i.e. photons not converting before leaving the volume of the inner detector.

The energy resolution as a function of energy is shown in figures 10.50 and 10.51, respectively for electrons and photons and for three illustrative values of $|\eta|$. The results shown here include the expected electronic noise contributions at 100 GeV of 190, 190 and 230 MeV (respectively 180, 180 and 230 MeV) for the three η-values for electrons (respectively photons).

As expected in the case of the points at the larger η-values, the resolution is degraded with respect to the one at the more central value of η. Fits to these results similar to those described in section 5.7.1 and expressed in eq. (5.2) yield stochastic terms of respectively 10.0%, 15.1% and 14.5% for the electrons at the three η-values shown. The corresponding terms for photons are found to be 10.2%, 12.4% and 12.1%, once again showing that photons are less sensitive than

2008 JINST 3 S08003

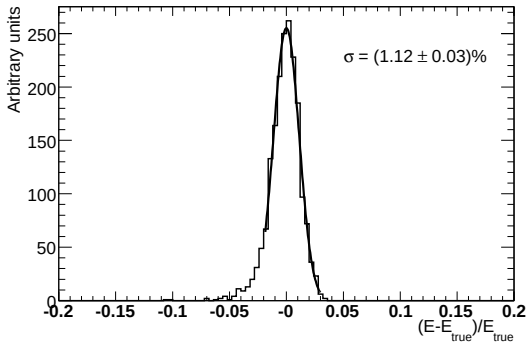

Figure 10.46: Difference between measured and true energy normalised to true energy for electrons with an energy of 100 GeV at $\eta = 0.325$.

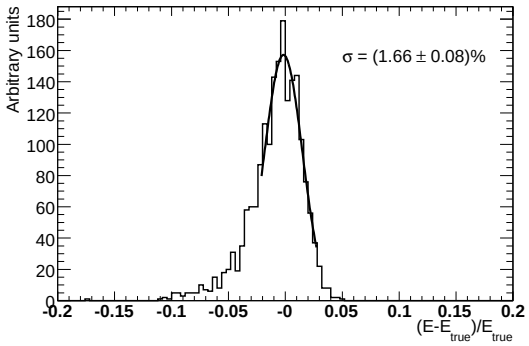

Figure 10.47: Difference between measured and true energy normalised to true energy for electrons with an energy of 100 GeV at $\eta = 1.075$.

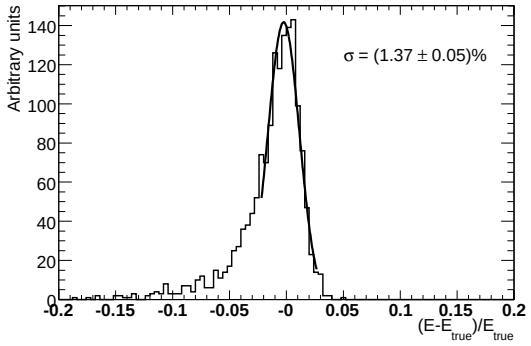

Figure 10.48: Difference between measured and true energy normalised to true energy for all photons with an energy of 100 GeV at $\eta = 1.075$.

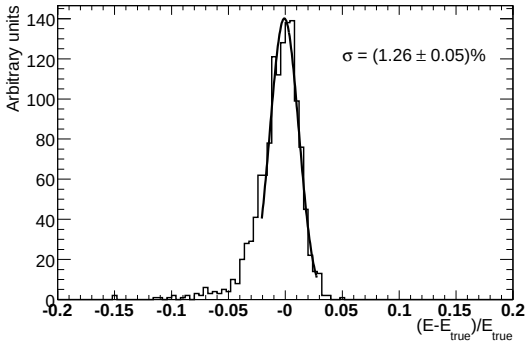

Figure 10.49: Difference between measured and true energy normalised to true energy for unconverted photons with an energy of 100 GeV at $\eta = 1.075$.

electrons to the material in front of the calorimeter. This can also be clearly seen when comparing figures 10.52 and 10.53, which show for electrons and photons the expected relative energy resolution as a function of $|\eta|$ for a fixed energy of 100 GeV. The η-region between 1.37 and 1.52 corresponds to the difficult transition region between the barrel and end-cap cryostats, where the energy resolution degrades significantly despite the presence of scintillators in the crack between the barrel and end-cap cryostats to correct for the energy lost in the barrel cryostat flange (see section 5.5). This crack region is not used for photon identification nor for precision measurements with electrons.

In figure 10.54, the expected η-resolution is shown for the two main layers (strips and middle layer) of the barrel and end-cap calorimeters. The resolution is fairly uniform as function of $|\eta|$ and is $2.5 - 3.5 \times 10^{-4}$ for the strips (which have a size of 0.003 in η in the barrel electromagnetic calorimeter) and $5 - 6 \times 10^{-4}$ for the middle-layer cells (which have a size of 0.025 in η). The regions with worse resolution correspond to the barrel/end-cap transition region and, for the

2008 JINST 3 S08003

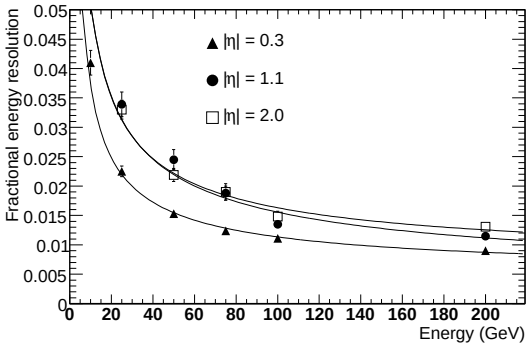

Figure 10.50: Expected relative energy resolution as a function of energy for electrons at $|\eta| = 0.3$, 1.1, and 2.0. The curves represent fits to the points at the same $|\eta|$ by a function containing a stochastic term, a constant term and a noise term.

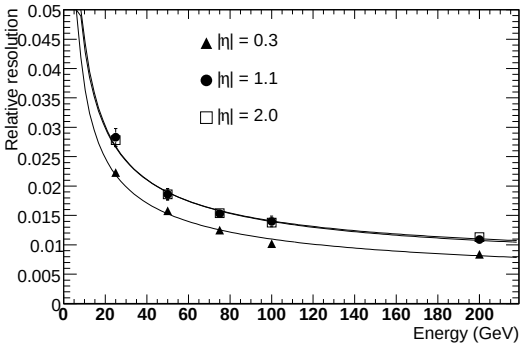

Figure 10.51: Expected relative energy resolution as a function of energy for photons at $|\eta| = 0.3$, 1.1, and 2.0. The curves represent fits to the points at the same η by a function containing a stochastic term, a constant term and a noise term.

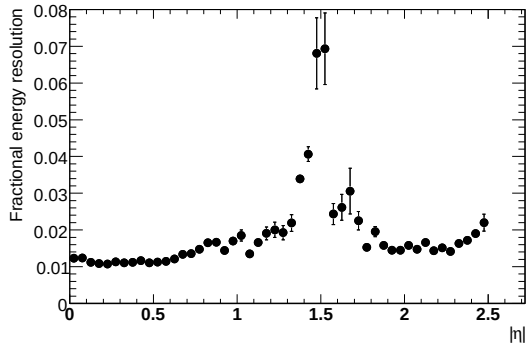

Figure 10.52: Expected relative energy resolution as a function of $|\eta|$ for electrons with an energy of 100 GeV.

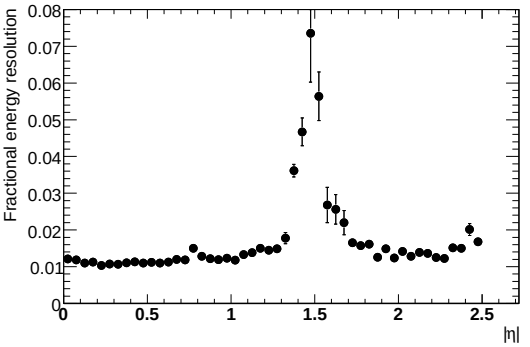

Figure 10.53: Expected relative energy resolution as a function of $|\eta|$ for photons with an energy of 100 GeV.

strips, to the region with $|\eta| > 2$, where the strip granularity of the end-cap calorimeter becomes progressively much coarser (see table 1.3). The results shown in section 5.7.1 are somewhat better because they correspond to a higher electron energy of 245 GeV.

Because of the fine lateral and longitudinal granularity of the electromagnetic calorimeter, these η-measurements can be used to determine the direction of the axis of the shower development in the η-direction (or polar angle θ). To achieve the best performance, one requires an accurate parametrisation of the shower depth (R-coordinate in the barrel and z-coordinate in the end-caps), as determined by Monte-Carlo simulations for both layers. The resulting resolution on the polar angle of photon showers is shown in figure 10.55 for a representative sample of photons from $H \rightarrow \gamma\gamma$ decays. A resolution of 50–75 mrad $/\sqrt{E\ (\mathrm{GeV})}$ is obtained, which should be sufficient to e.g. measure accurately the invariant mass of photon pairs without using any primary vertex information.

2008 JINST 3 S08003

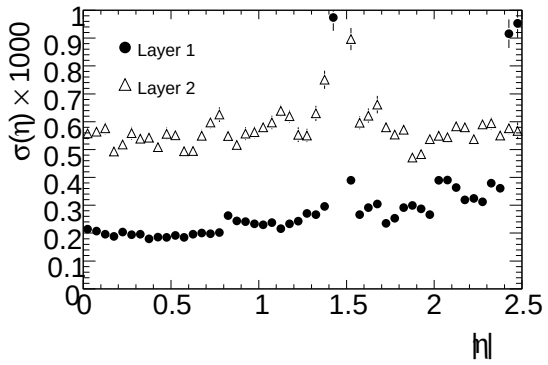

Figure 10.54: Expected η-resolution as a function of $|\eta|$ for photon showers with an energy of 100 GeV and for the two main layers of the barrel and end-cap electromagnetic calorimeters.

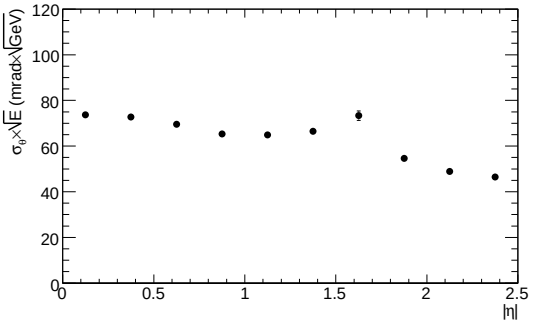

Figure 10.55: Expected precision on the polar angle θ of photons from $H \to \gamma\gamma$ decays as a function of $|\eta|$, expressed in units of mrad $\cdot \sqrt{E}$, where E is the measured energy of the photon shower in GeV.

In addition to the calorimeter-seeded electron and photon reconstruction, a second electron reconstruction and identification algorithm uses good-quality tracks as a seed and constructs a cluster around the extrapolated impact point in the calorimeter [266]. This algorithm relies more on the electron identification capabilities of the inner detector and has been developed to improve the efficiency for low-p_T electrons (see section 10.4.3) as well as for electrons close to jets (see section 10.8.5). The algorithm matches good-quality inner-detector tracks to small clusters of electromagnetic energy. For a given track, only the energy contained in a small window along the track extrapolation is used and the contribution of neighbouring hadronic showers is therefore reduced. The identification procedure takes full advantage of the tracking and electron-identification capabilities of the TRT in the inner detector (over $|\eta| < 2.0$, as described in section 10.2.5), as well as of the granularity of the electromagnetic calorimeter. A likelihood ratio combines inner-detector information (measured track momentum and transition-radiation hits) with shower-shape variables from the calorimeter.

In the following, unless specified otherwise (as in section 10.4.3), only the results of the calorimeter-seeded algorithm will be discussed.

10.4.2 Electron and photon reconstruction and identification

For the standard reconstruction of electrons and photons, a seed cluster is taken from the electromagnetic calorimeter and a loosely matching track is searched for among all reconstructed tracks. Additionally, the candidate is flagged if it matches a photon conversion reconstructed in the inner detector. Electron and photon candidates are thus separated reasonably cleanly, by requiring the electrons to have an associated track but no associated conversion. In contrast, the photons are defined as having no matched track, or as having been matched to a reconstructed conversion.

For all electron and photon candidates, shower-shape variables (lateral and longitudinal shower profiles, etc.) are calculated using the fine granularity of the electromagnetic calorimeter, and typically more than 50 calorimeter cells are summed to collect the full cluster energy. Addition-

ally, combined reconstruction properties, such as the ratio of energy (calorimeter) to momentum (inner detector), the difference between the coordinates η and ϕ reconstructed by the cluster and the track extrapolated into the calorimeter, and the ratio of high-threshold transition radiation hits to low-threshold hits on the track, are used to identify electrons.

The energy of high-p_T electrons is obtained from the energy measured in the calorimeter (the inner-detector momentum measurement is not expected to improve the accuracy of the calorimeter energy measurement significantly for energies above 20–30 GeV). The η and ϕ directions are, however, more precisely determined using the associated track. For photons, everything is derived from the calorimeter information, the energy, the ϕ-direction using the precisely known average transverse position of the primary vertex, and the η-direction as described above.

10.4.2.1 Electrons

The standard identification for isolated high-p_T electrons is based on cuts on the shower shapes, on information from the reconstructed track and on the combined reconstruction. Jet rejections are computed with respect to truth-particle jets reconstructed using particle four-momenta within a cone of size $\Delta R = 0.4$. Three sets of cuts have been studied depending on the signal efficiency and jet rejection requirements of the physics samples under study:

- "loose cuts" consisting of simple shower-shape cuts (longitudinal leakage, shower shape in the middle layer of the electromagnetic calorimeter) and very loose matching cuts between reconstructed track and calorimeter cluster;
- "medium cuts", which add shower-shape cuts using the important information contained in the first layer of the electromagnetic calorimeter and track-quality cuts similar to the standard reconstruction cuts quoted in section 10.2.3;
- "tight cuts", which tighten the track-matching criteria and the cut on the energy-to-momentum ratio. These cuts also explicitly require the presence of a vertexing-layer hit on the track (to further reject photon conversions) and a high ratio between high-threshold and low-threshold hits in the TRT detector (to further reject the background from charged hadrons), as shown in section 10.2.5. Additionally, further isolation of the electron may be required by using calorimeter energy isolation beyond the cluster itself. Two sets of tight selection cuts are used in this section to illustrate the overall performance of the electron identification. They are labelled as "tight (TRT)", in the case where a TRT cut with approximately 90% efficiency for electrons is applied, and as "tight (isol.)", in the case where a TRT cut with approximately 95% efficiency is applied in combination with a calorimeter isolation cut.

The performance of the cut-based analysis is summarised in table 10.3 and in figure 10.56 for electrons. As can be seen from table 10.3, the signal from prompt electrons is dominated by initially non-isolated electrons from heavy flavours, which explains the much lower efficiency observed for these electrons. Dedicated algorithms might improve this efficiency somewhat, but these electrons will nevertheless provide the most abundant initial source of isolated electrons and will be used for alignment of the electromagnetic calorimeters and the inner detector, for E/p calibrations, and more generally to improve the understanding of the material of the inner detector. For tight cuts and

Table 10.3: Expected efficiencies for isolated and non-isolated electrons and corresponding jet background rejections for the three standard levels of cuts used for electron identification. The results are shown for simulated inclusive jet samples corresponding to E_T-thresholds of the electron candidates of 17 GeV (left) and 8 GeV (right). The three bottom rows show, for each of the inclusive jet samples, the fractions of all surviving candidates which originate from the different categories for the medium cuts and the two sets of tight cuts. The isolated electrons are prompt electrons from W, Z and top-quark decay and the non-isolated electrons are from b, c decay. The residual jet background is split into its two dominant components, electrons from photon conversions and Dalitz decays (first term in brackets) and charged hadrons (second term in brackets). The quoted errors include part of the systematics, but do not include the larger systematic uncertainties from the physics input and detector simulation.

Cuts	$E_T >$ **17 GeV**			$E_T >$ **8 GeV**		
	Efficiency (%)		**Jet rejection**	**Efficiency (%)**		**Jet rejection**
	$Z \rightarrow ee$	$b,c \rightarrow e$		Single electrons (E_T=10 GeV)	$b,c \rightarrow e$	
Loose	87.9 ± 0.5	38 ± 1	570 ± 10	75.7 ± 0.5	46 ± 1	510 ± 10
Medium	76.7 ± 0.5	27 ± 1	2200 ± 20	64.8 ± 0.5	36 ± 1	1280 ± 10
Tight (TRT)	61.3 ± 0.5	20 ± 1	$(8 \pm 1)10^4$	46.4 ± 0.5	25 ± 1	$(4.7 \pm 0.5)10^4$
Tight (isol.)	63.6 ± 0.5	16 ± 1	$(9 \pm 1)10^4$	48.7 ± 0.5	24 ± 1	$(4.3 \pm 0.5)10^4$
	Relative populations of surviving candidates (%)			**Relative populations of surviving candidates (%)**		
	Isolated	Non-isolated	Jets	Isolated	Non-isolated	Jets
Medium	0.9	6.4	92.6 (1.5 + 91.1)	—	7.7	92.3 (2.2 + 90.9)
Tight (TRT)	10.5	56.1	33.4 (4.3 + 29.0)	—	63.2	36.8 (4.0 + 32.8)
Tight (isol.)	13.0	53.4	33.6 (4.6 + 29.0)	—	62.8	37.2 (4.4 + 30.3)

an electron p_T of $\sim$ 20 GeV, the isolated electrons from W, Z and top-quark decays represent less than 20% of the total prompt electron signal and are only at the level of $\sim$ 30–40% of the residual jet background. For the lower E_T-threshold of 8 GeV, the expected signal from isolated electrons is negligibly small. Not surprisingly, the tight TRT cuts are more efficient to select non-isolated electrons from heavy-flavour decay, while the tight isol. cuts are more efficient at selecting isolated electrons. After tight cuts, the signal-to-background ratio is close to 2:1, and depends only weakly on the E_T-threshold. The residual background is dominated by charged hadrons. Further rejection could be possible at the expense of loss of efficiency by stronger cuts (TRT and/or isolation) and by improving the photon conversion reconstruction (see section 10.2.5).

Figure 10.56 shows in more detail the overall reconstruction and identification efficiencies for the three sets of electron cuts discussed above: the E_T dependence of the efficiencies is shown for single electrons of fixed E_T as well as for physics processes containing isolated electrons from cascade decays of supersymmetric particles to illustrate the rather stable behaviour of the cuts when moving from the ideal case of single particles to a busy environment with many additional jets in the event. The somewhat worse efficiency observed in complex events is attributed to the fraction of cases when the electron candidate is close to or even within a high-p_T jet. The overall efficiency of the cuts remains stable for even higher electron energies (the efficiency of the tight isol. cuts is 68% for electrons of E_T = 500 GeV).

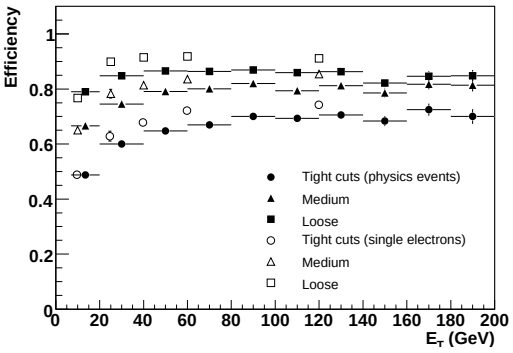

Figure 10.56: Overall reconstruction and identification efficiency of various levels of electron cuts: loose, medium, and tight isol. as a function of E_T for single electrons (open symbols) and for isolated electrons in a sample of physics events with a busy environment (full symbols).

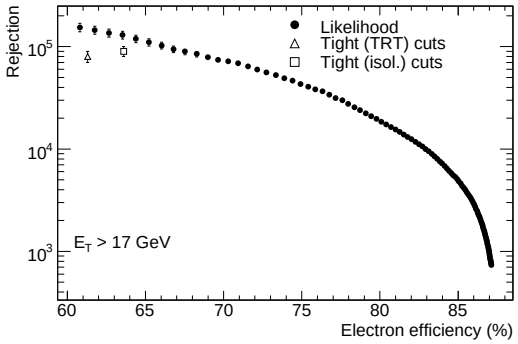

Figure 10.57: Jet rejection as a function of overall reconstruction and identification efficiency for electrons, as obtained using a likelihood method (full circles). The results obtained with the standard cut-based method are also shown in the case of tight TRT (open triangle) and tight isol. (open square) cuts.

In addition to the traditional cut-based analysis, multivariate techniques have been developed, based on similar variables, and the performance of a likelihood technique is shown as an example in figure 10.57. Compared to the tight cuts described above, a gain of 4–8% in efficiency for the same fixed rejection against jets or of 40–60% in rejection for the same fixed efficiency can be obtained, using this likelihood method for isolated electrons with energies typical of those expected from $Z \rightarrow ee$ decays.

As discussed already to some extent in section 10.2.5, certain dedicated tracking algorithms improve the momentum reconstruction for electrons with transverse momenta up to 10 GeV. However, as shown in figure 10.58 for electrons with $p_T = 25$ GeV, a significant reduction of the tails due to bremsstrahlung can only be achieved at higher energies by combining the inner-detector measurements with the accurate measurement of the ϕ-position of the electromagnetic shower. This latter constraint, when combined with the extrapolated track impact in the calorimeter, provides enough information to estimate with reasonable accuracy the origin and energy of a hard bremsstrahlung photon. As shown in figure 10.58, this combined bremsstrahlung

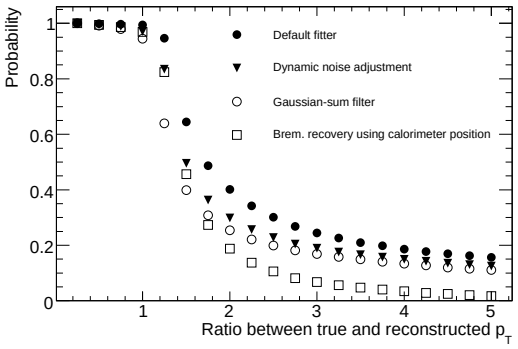

Figure 10.58: For electrons with $p_T = 25$ GeV and $|\eta| > 1.5$, integral probability for ratio of true to reconstructed transverse momentum to exceed a given value. The various symbols represent different track-fitting algorithms (see section 10.2.5) and the bremsstrahlung recovery algorithm, which uses the accurate measurement of the shower position in ϕ in the electromagnetic calorimeter (see text).

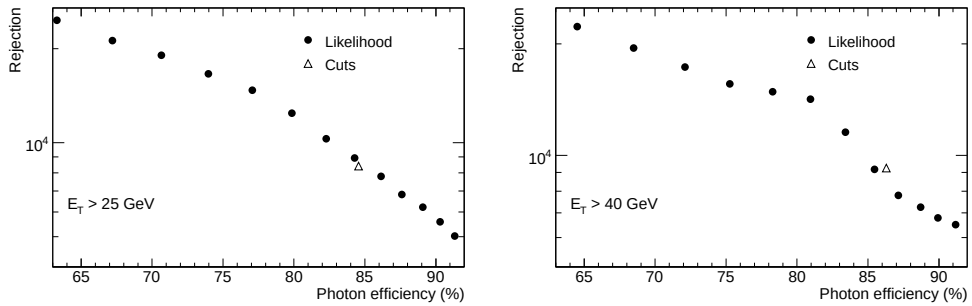

Figure 10.59: For reconstructed photon candidates with $E_T > 25\,\text{GeV}$ (left) and with $E_T > 40\,\text{GeV}$ (right), jet rejection as a function of photon efficiency, as obtained using a likelihood method. The results obtained with the standard cut-based method are also shown for reference.

recovery procedure will reduce considerably the tails in the E/p distribution, which will be an important tool for studying the uniformity of calibration of the electromagnetic calorimeter, as well as material and alignment effects.

10.4.2.2 Photons

Photons are much harder to extract as a signal from the jet background than certain specific isolated electron signals, such as those expected from $Z \rightarrow ee$ or $W \rightarrow e\nu$ decays. A single set of photon identification cuts, equivalent to the "tight cuts" defined for electrons, has been optimised based on the shower shapes in the calorimeter with special emphasis on separating single π^0's from photons using the very fine granularity in η of the strip layer. In addition, a simple track-isolation criterion has been added to further improve the rejection while preserving the vast majority of converted photons. Using these criteria, an efficiency of 84% has been obtained for photons with an energy spectrum as expected from $H \rightarrow \gamma\gamma$ decay with $m_H = 120\,\text{GeV}$. This efficiency is quite uniform over the whole η-range except for the crack between the barrel and end-cap calorimeters mentioned above. For this value of the photon efficiency, a jet rejection of ~ 5000 (without track isolation) to 9000 (with track isolation) has been achieved, averaged over the parton flavours corresponding to the inclusive di-jet background sample used. The expected jet rejections are shown in table 10.4 separately for quarks and gluons and for two relevant values of the E_T-threshold applied to the photon candidates. The larger rejection expected against gluon jets is due to the softer fragmentation and therefore broader lateral extent of gluon jets compared to light jets which are dominant in the quark-jet sample. The residual background from jets is mostly composed of isolated π^0's, so the fine-grained strip layer of the electromagnetic calorimeter is an important element to achieve such rejections. As for the electrons, the jet rejections are computed with respect to truth-particle jets reconstructed using particle four-momenta within a cone of size $\Delta R = 0.4$.

Multivariate methods have also been developed for the more difficult case of photon identification. These can be seen in figure 10.59, which shows as an example the expected performance for a likelihood technique compared to the standard cut-based analysis. For photon candidates with $E_T > 25\,\text{GeV}$ and a fixed efficiency of 84%, the rejection with respect to the cut-based selection is improved by 6% for the likelihood method.

Table 10.4: Jet rejections obtained before and after applying track-isolation cuts for photon candidates with $E_T > 25$ GeV and $E_T > 40$ GeV and for a photon efficiency of approximately 84%. The rejection values are shown with their statistical errors separately for quark and gluon jets.

Selection cuts	$E_T > 25$ GeV		$E_T > 40$ GeV	
	Quark jets	Gluon jets	Quark jets	Gluon jets
Before isolation	1770±50	15000±700	1610±100	15000±1600
After isolation	2760±100	27500±2000	2900±240	28000±4000

10.4.2.3 Reconstruction of $H \rightarrow eeee$ and $H \rightarrow \gamma\gamma$ final states

The performance of the reconstruction, including calibration, with the identification criteria discussed above is shown in figure 10.60 for decays of a Higgs boson with a mass of 130 GeV to four electrons (loose electron cuts applied) and in figure 10.61 for decays of a Higgs boson with a mass of 120 GeV to two photons (tight photon cuts applied and barrel/end-cap transition region excluded). A global constant term of 0.7% has been included in the electromagnetic calorimeter resolution for these plots. In the case of $H \rightarrow \gamma\gamma$ decays, the photon directions are derived from a combination of the direction measurement in the electromagnetic calorimeter described above (see figure 10.55) with the primary vertex information from the inner detector (see table 10.2).

In the case of the Higgs-boson decay to four electrons, the central value of the reconstructed invariant mass is correct to ~ 1 GeV, corresponding to a precision of 0.7%, and the expected Gaussian resolution is $\sim 1.5\%$. The non-Gaussian tails in the distribution amount to 20% of events which lie further than 2σ away from the peak. They are mostly due to bremsstrahlung, particularly in the innermost layers of the inner detector, but also to radiative decays and to electrons poorly measured in the barrel/end-cap transition region of the electromagnetic calorimeter.

In the case of the Higgs-boson decay to two photons, the central value of the reconstructed invariant mass is correct to ~ 0.2 GeV, corresponding to a precision of 0.3%, and the expected resolution is $\sim 1.2\%$. Figure 10.61 also clearly shows that most of the non-Gaussian tails at low values of the reconstructed mass of the photon pair are due to photons which converted in the inner detector.

10.4.3 Assessment of performance in situ with initial data

One important ingredient in the calibration strategy for the electromagnetic calorimeter is the use of large-statistics samples of $Z \rightarrow ee$ decays to perform an accurate inter-calibration of regions with a fixed size of $\Delta\eta \times \Delta\phi = 0.2 \times 0.4$ [267]. It is expected that such a scheme will decrease the initial spread from region to region, conservatively assumed to be approximately 1.5–2%, to values comparable to the expected constant term of $\sim 0.5\%$ in each region. This however assumes an excellent knowledge of the material in front of the electromagnetic calorimeter. The material in the inner detector should be eventually mapped out very accurately using e.g. photon conversions, but other less sensitive but more robust methods will also be used, exploiting the high granularity of the electromagnetic calorimeter. The energy flow measured in the second layer of the electromagnetic calorimeter, for example in minimum-bias events, provides such a tool, as illustrated in figure 10.62. Only energy deposits more than 5σ above the electronic noise level are considered

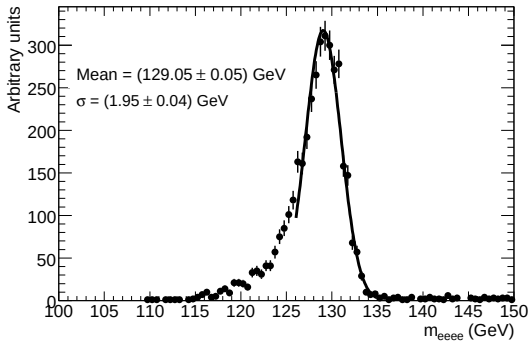

Figure 10.60: Expected distribution for the invariant mass of the four electrons from Higgs-boson decays with m_H = 130 GeV. The energies of the electrons are determined only from the electromagnetic calorimeter measurements. The results do not include a Z-mass constraint.

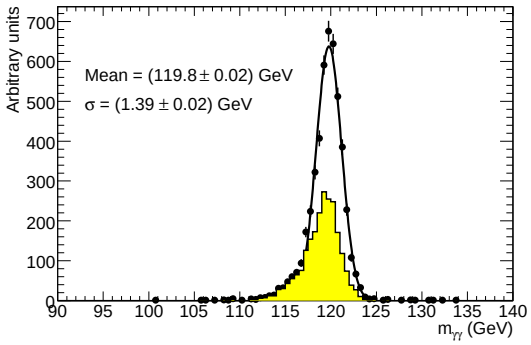

Figure 10.61: Expected distribution for the invariant mass of the two photons from Higgs-boson decays with m_H = 120 GeV. The shaded plot corresponds to events in which at least one of the two photons converted at a radius below 80 cm.

for these measurements. With approximately two million minimum-bias events, corresponding to roughly one day of data-taking, additional material inside the inner detector amounting to 20% X_0 would be identified in any region of size $\Delta\eta \times \Delta\phi = 0.1 \times 0.1$ [268]. Another more sensitive possibility is the study of the ϕ-symmetry of the fraction of energy deposited in the first layer of the electromagnetic calorimeter by isolated electrons, as shown in figure 10.63. Combining this information with that from the other layers in the calorimeter and with the momentum measurement of the electrons will provide higher sensitivity (for example in η) than the minimum-bias results.

Figure 10.64 shows the result of such an inter-calibration procedure applied to simulated $Z \rightarrow ee$ decays with an initial 2% spread from region to region. Once the material in front of the electromagnetic calorimeter is sufficiently well understood, an inter-calibration accuracy of 0.7% could be achieved for a total of approximately 50,000 $Z \rightarrow ee$ decays, reconstructed with the medium set of identification cuts described above, and corresponding to an integrated luminosity of $\sim 150\ \text{pb}^{-1}$.

As described in section 10.9.3 for initial luminosities of $10^{31}\ \text{cm}^{-2}\ \text{s}^{-1}$, a trigger on low-mass di-electron pairs (the 2e5 signature in table 10.7) should provide good statistics of $J/\psi \rightarrow ee$ and $\Upsilon \rightarrow ee$ decays. An example of the signal and background samples which will be provided by the low-mass pair di-electron trigger in early data is shown in figure 10.65. For this study, the track-seeded algorithm introduced in section 10.4.1 has been used with tight electron cuts as described above. The signal-to-background ratio obtained is larger than one at the J/ψ and Υ peaks, but the extraction of electron pairs from Drell-Yan will require further studies (tighter identification or kinematic cuts). With an integrated luminosity of 100 pb^{-1} and an efficient identification and reconstruction of these low-mass pairs, approximately 100,000 J/ψ decays and 30,000 Υ decays could be isolated for detailed studies of the electron identification and reconstruction performance, in particular in terms of matching energy and momentum measurements at a scale quite different from that of the more commonly used $Z \rightarrow ee$ decays.

2008 JINST 3 S08003

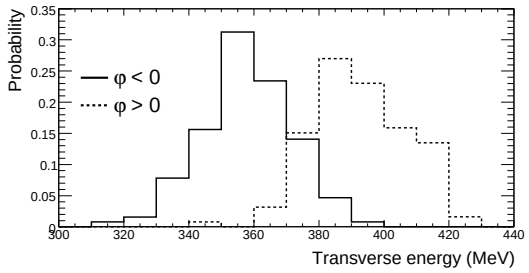

Figure 10.62: Distribution of the transverse energy accumulated in $\Delta\eta \times \Delta\phi = 0.1 \times 0.025$ middle-layer regions with a few hours of minimum bias events. The full histogram corresponds to the hemisphere with a nominal amount of inner-detector material in the simulation for $1.8 < \eta < 1.9$, whereas the dotted histogram corresponds to the hemisphere with a 25% increase in the amount of material in the same η-region.

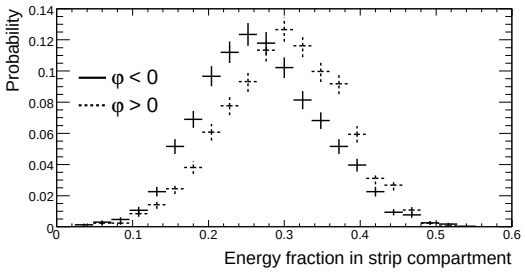

Figure 10.63: Distribution of the fraction of energy deposited in the strip layer by electrons from W/Z decays corresponding to the statistics expected for an integrated luminosity of 50 pb^{-1}. The full histogram corresponds to the hemisphere with a nominal amount of inner-detector material in the simulation for $1.8 < \eta < 1.9$, whereas the dotted histogram corresponds to the hemisphere with a 25% increase in the amount of material in the same η-region.

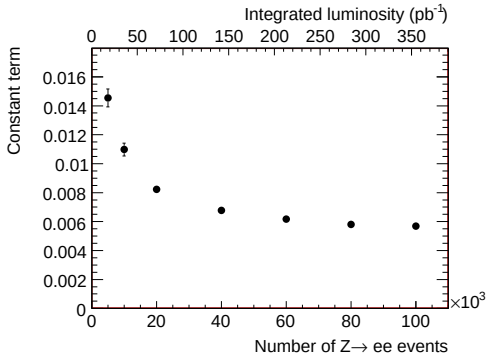

Figure 10.64: Statistical accuracy expected from inter-calibration of the electromagnetic calorimeter as a function of the number of reconstructed $Z \rightarrow ee$ decays or of the integrated luminosity (see text). These results assume a perfect knowledge of the material in front of the electromagnetic calorimeter.

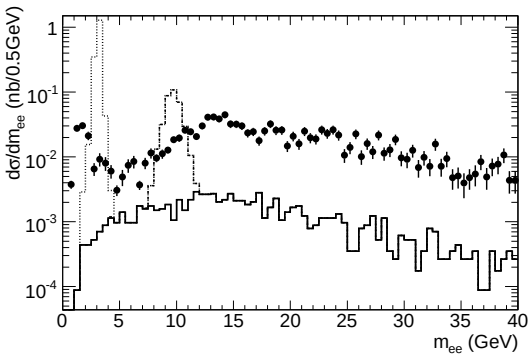

Figure 10.65: Expected differential cross-section for low-mass electron pairs using the 2e5 trigger menu item discussed in section 10.9.3. Shown is the invariant di-electron mass distribution reconstructed using tracks for $J/\psi \rightarrow ee$ decays (dotted histogram), $\Upsilon \rightarrow ee$ decays (dashed histogram) and Drell-Yan production (full histogram). Also shown is the expected background after the offline selection described in the text (full circles).

10.5 Jet reconstruction

The ATLAS calorimeters have very high lateral granularity and several samplings in depth over $|\eta| < 3.2$ (see table 1.3 for an overview of the properties of the various ATLAS calorimeters). The forward calorimeters, which cover the region $3.2 < |\eta| < 4.9$, also provide sufficient granularity to reconstruct jets with small polar angles with reasonable accuracy and efficiency. For the reconstruction of jets in the wide variety of physics processes of interest at the LHC, specific care has therefore been taken to devise a modular and generic design of the corresponding software. The implementation allows for the use of a variety of jet clustering algorithms using as input any reconstruction object having a four-momentum representation. These inputs can vary from calorimeter cells, or charged tracks, to Monte-Carlo truth objects, such as stable particles or final-state partons from the generator. It also supports easy implementation of jet-clustering algorithms different from the ones most commonly used, and has followed the guidelines collected for Run II at the Tevatron [269].

10.5.1 Jet clustering algorithms

The two default jet-clustering algorithms in ATLAS are a seeded fixed-cone algorithm and a successive recombination algorithm. Both algorithms are used in two different configurations, one producing narrow jets for e.g. W-mass spectroscopy in $t\bar{t}$ events or events containing large multiplicities of jets as in supersymmetric models, and the other producing wider jets for e.g. QCD studies of di-jet and multi-jet final states at luminosities below 10^{33} cm^{-2} s^{-1}.

The seeded cone algorithm uses two parameters, the transverse energy threshold for a seed, $E_T = 1$ GeV for all cone jets, and the cone size, $\Delta R = \sqrt{\Delta\eta^2 + \Delta\phi^2}$, with $\Delta R = 0.4$ for narrow jets and $\Delta R = 0.7$ for wide jets. In all cases, a split-and-merge step follows the actual cone building, with an overlap fraction threshold of 50%. The cone algorithm in this particular implementation is fast and therefore also used in the high-level trigger (see section 10.9).

The $k_\perp$ algorithm in ATLAS is implemented following the suggestions in [270], which makes it efficient even for a rather large number of input objects and avoids the usual pre-clustering step. The distance parameter $R = \sqrt{\Delta\eta^2 + \Delta\phi^2}$ is adjusted for narrow jets to $R = 0.4$ and for wide jets to $R = 0.6$. The physics performance is very similar to the one of the corresponding cone configurations. In all cases the full four-momentum recombination is used to calculate the jet kinematics after each clustering step.

10.5.2 Input to jet reconstruction

Typical inputs for jet-finding in ATLAS are final-state particles for truth-particle jets, and calorimeter signals for reconstructed or calorimeter jets. Naturally, truth-particle jets are only available in simulated data. They are formed by applying a jet algorithm to all stable neutral and charged particles in the final state within $|\eta| < 5$. These particles can emerge from the hadronisation of the hard-scattered parton, from initial- and final-state radiation, and from the underlying multiple interactions in the event. The kinematic properties of these particles are taken at their generation vertex, before any interaction with the detector and its magnetic field.

2008 JINST 3 S08003

Figure 10.66 presents an overview of the reconstruction flow for calorimeter jets. Calorimeter jets are reconstructed by applying a jet-clustering algorithm to calorimeter signals, typically followed by a calibration step. Two different signals from the calorimeter are used for jet-finding, towers and topological clusters. Towers are formed by collecting cells into bins of a regular $\Delta\eta \times \Delta\phi = 0.1 \times 0.1$ grid, depending on their location, and summing up their signals, or a fraction of their signal corresponding to the overlap area fraction between the tower bin and the cell in $\Delta\eta$ and $\Delta\phi$. This summing stage is non-discriminatory, meaning all calorimeter cells are used in the towers. Towers with negative signals are dominated by noise, and cannot be used in jet-finding. They are recombined with nearby positive signal towers until the net signal is positive, i.e. the resulting towers have a valid physical four-vector and can directly be used by the jet finders. This approach can be understood as an overall noise cancellation rather than suppression, since the noisy cells still contribute to the jets at initial luminosities of 10^{31} cm^{-2} s^{-1} to 10^{33} cm^{-2} s^{-1}.

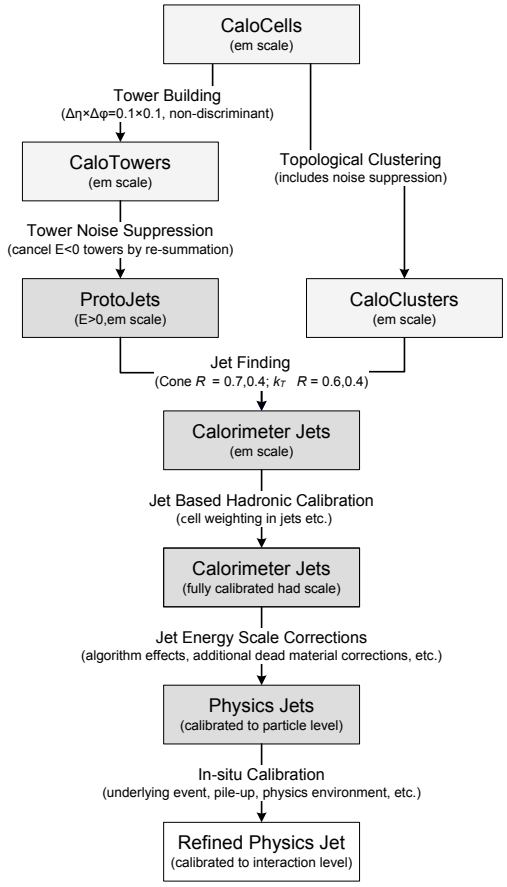

Figure 10.66: Jet reconstruction flow for calorimeter jets from towers or clusters.

Topological cell clusters represent an attempt to reconstruct three-dimensional energy depositions in the calorimeter [152, 271]. First, nearest neighbours are collected around seed cells with a significant absolute signal above the major seed threshold, i.e. $|E_{\text{cell}}| > 4\sigma_{\text{cell}}$ of the total noise (electronics plus pile-up). Energy equivalents of the σ of the electronic noise alone in the various calorimeter cells are shown in figure 5.27, while figure 10.67 shows estimates for the total σ when fluctuations from pile-up at a luminosity of 2×10^{33} cm^{-2} s^{-1} are included at the cell level. These neighbouring cells are collected independently of the magnitude of their own signal. If the absolute value of their signal significance is above a secondary seed threshold, typically such that $|E_{\text{cell}}| > 2\sigma_{\text{cell}}$, they are considered secondary seeds and their direct neighbours are also collected. Finally, all surrounding cells above a very low threshold (typically set to 0σ) are added if no more secondary seeds are among the direct neighbours. A final analysis of the resulting cluster looks for multiple local signal maxima. In case of more than one maximum in a given cluster, it is split into smaller clusters, again in three dimensions, along the signal valleys between the maxima.

Contrary to the signal tower formation, topological cell clustering includes actual noise suppression, meaning that cells with no signal at all are most likely already not included in the cluster. This results in substantially less noise, as shown in figure 10.68, and less cells, as shown in figure 10.69, in these cluster jets than in tower jets. Topological cell clusters are under study for

2008 JINST 3 S08003

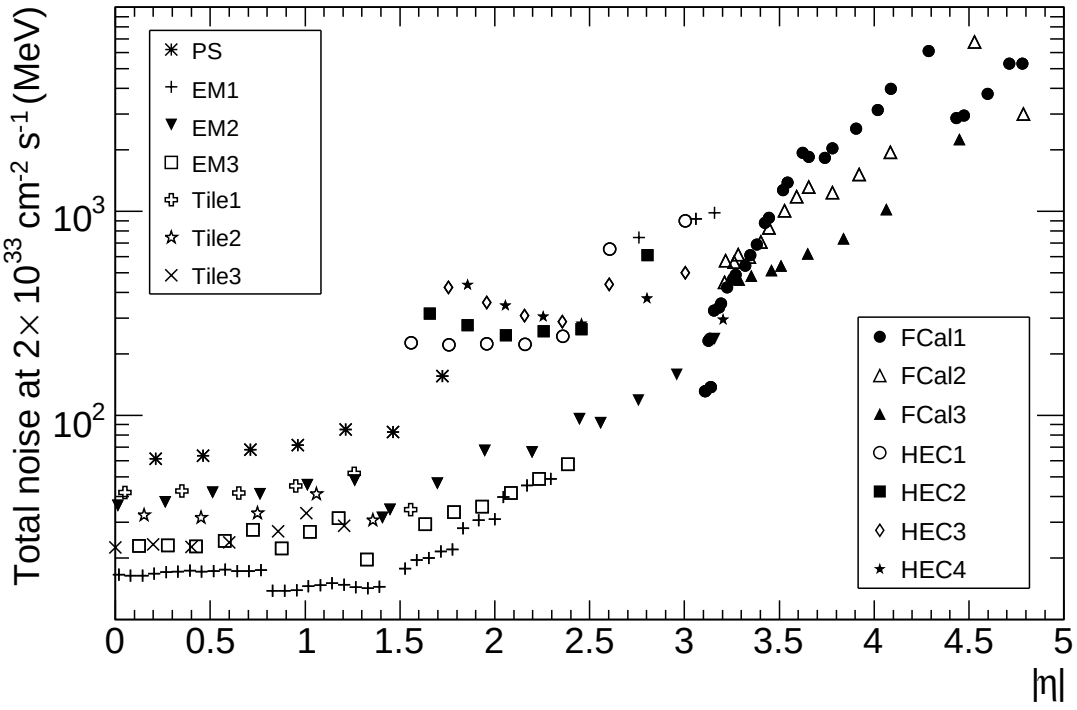

Figure 10.67: Expected noise from the electronics and pile-up at 2×10^{33} cm^{-2} s^{-1} in individual cells of the various layers of the calorimeters as a function of $|\eta|$. See Figure 5.27 for the pure electronic noise expected from the various layers of the calorimeters. Note that the presampler noise is corrected for by the appropriate sampling fractions as discussed in section 5.6.2.1.

use as the basis for the local hadronic energy calibration, which attempts to correct for detector effects, such as calorimeter responses with $e/h > 1$ and dead-material energy losses, outside of the jet context itself. Although very promising in terms of noise suppression, the topological cell clustering will require careful validation with real data, in particular in terms of the possible impact of long-range noise correlations and of detailed studies of pile-up effects as the luminosity increases.

10.5.3 Jet calibration

The strategy currently adopted for calorimeter jet calibration in ATLAS is the application of cell signal weighting similar to the original approach developed for the H1 calorimeter [272]: all calorimeter cells with four-momenta $(E_i, \vec{p}_i)$, where $E_i = |\vec{p}_i|$, in tower or cluster jets are considered and re-summed with weighting functions, w, such that the resulting new jet four-momentum is:

$$\left(E_{\mathrm{rec}}, \vec{p}^{\,\mathrm{jet}}_{\mathrm{rec}}\right) = \left(\sum_i^{N_{\mathrm{cells}}} w(\rho_i, \vec{X}_i) E_i, \sum_i^{N_{\mathrm{cells}}} w(\rho_i, \vec{X}_i)\vec{p}_i\right). \tag{10.2}$$

The weighting functions w depend on the cell signal density, $\rho_i = E_i/V_i$, where V_i is the volume of the cell considered, and on the cell location in the calorimeter, $\vec{X}_i$, consisting basically of module and layer identifiers. They are fitted using simulated QCD di-jet events, covering the whole kinematic range expected at the LHC, and matching calorimeter cone-tower jets, with $\Delta R = 0.7$, with

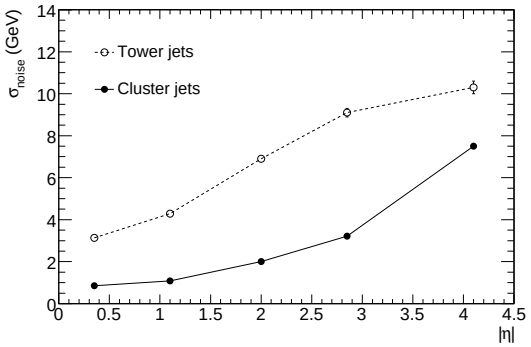

Figure 10.68: Average electronic noise contribution to cone jets with $\Delta R = 0.7$ in QCD di-jet events, reconstructed from towers (open circles) and topological cell clusters (full circles), as a function of $|\eta|$.

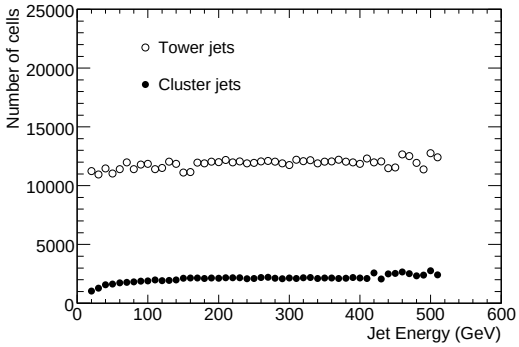

Figure 10.69: Average total number of cells contributing to cone jets with $\Delta R = 0.7$ in QCD di-jet events, reconstructed from towers (open circles) and topological cell clusters (full circles), as a function of the jet energy.

nearby truth-particle cone jets of the same size and with energy E_{truth}, and then constraining E_{rec} in eq. (10.2) to E_{truth} by:

$$\frac{\partial \chi^2}{\partial w(\rho_i, \vec{X}_i)} = \frac{\partial}{\partial w(\rho_i, \vec{X}_i)} \left[\sum_{\text{matched jets}} \frac{((E_{\text{rec}} + E_{\text{DM}}) - E_{\text{truth}})^2}{E_{\text{truth}}} \right] = 0 . \tag{10.3}$$

The weighting functions determined in this way absorb all detector effects, including missing signals from charged truth particles with less than $\sim$ 400 MeV transverse momentum, which are bent away from the calorimeter by the solenoid magnetic field in the inner detector cavity. Implicitly included also are corrections for energy loss in inactive materials, except for losses between the electromagnetic barrel and tile barrel calorimeters, which are parametrised in eq. (10.3) as:

$$E_{\text{DM}} = \alpha \sqrt{E_{EMB3} E_{TILE0}} , \tag{10.4}$$

where E_{EMB3} is the sum of the energies of the cells in the last layer of the barrel electromagnetic calorimeter belonging to the jet and E_{TILE0} is the corresponding sum in the first layer of the hadronic tile calorimeter. Both quantities are reconstructed at the electromagnetic energy scale. The parameter α was assumed to be independent of energy and of η and was determined together with $w(\rho_i, \vec{X}_i)$ in a combined fit according to eq. (10.3).

Naturally, the calibration applied in this way only corrects to the level of the truth-particle jet. The extracted weighting functions were obtained for cone-tower jets with $\Delta R = 0.7$ and are not universal, since they depend on the choice of calorimeter signals used, on the jet algorithm chosen and on its specific configuration, and on the choice of (simulated) physics calibration samples used to extract them. Residual mis-calibrations for all cluster cone and cluster $k_\perp$ jets are corrected for by functions depending on $|\eta|$ and p_T of each measured jet. Similar corrections are applied to tower cone jets with $\Delta R = 0.4$ and to the tower $k_\perp$ jets. These corrections have been derived by comparing the calorimeter jets after applying the cell signal weights and dead-material corrections with the matching truth-particle jet in the simulated QCD di-jet events.

2008 JINST 3 S08003

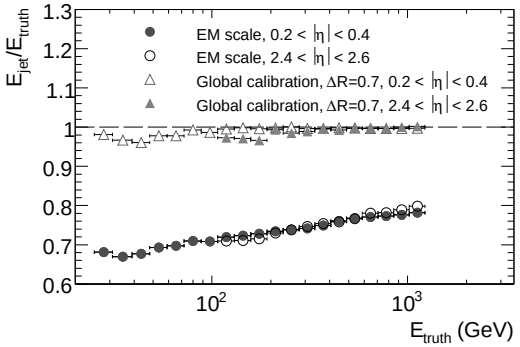

Figure 10.70: Signal linearity for cone-tower jets with $\Delta R = 0.7$, as expressed by the ratio of reconstructed tower jet energy to the matching truth-jet energy $E_{\mathrm{rec}}/E_{\mathrm{truth}}$, in two different regions of $|\eta|$ and as a function of E_{truth}. Jet signals calibrated at the electromagnetic energy scale are compared to the fully calibrated jets.

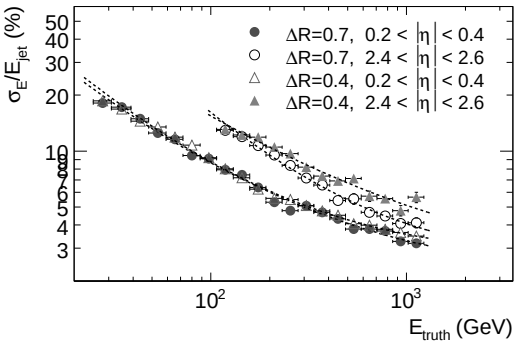

Figure 10.71: Fractional energy resolution for calibrated cone-tower jets reconstructed with $\Delta R = 0.7$ and $\Delta R = 0.4$ in two different regions of $|\eta|$ and as a function of E_{truth}.

10.5.4 Jet signal characteristics

All signal features discussed in the following are extracted from simulations including a model for the electronic noise in each calorimeter cell, tuned with parameters extracted from various test-beam measurements. The results shown here are, unless stated otherwise, based on the jet-calibration procedure described above, called from now on global calibration. Pile-up fluctuations are not included.

The most important requirements for the jet signal after global calibration are a linear response across all jet energies, a uniform response as independent as possible from the jet direction, and a fractional energy resolution within the specifications laid out in table 1.1.

10.5.4.1 Jet signal linearity and energy resolution

The signal linearity for calorimeter jets in ATLAS is expressed by the ratio of the reconstructed jet energy and the matched truth-jet energy, $E_{\mathrm{rec}}/E_{\mathrm{truth}}$, in simulated QCD di-jet events.

Figure 10.70 shows, for two different regions in $|\eta|$, that the the signal linearity for cone jets made from towers with $\Delta R = 0.7$ is reasonable over the whole energy range after the global calibration is applied. figure 10.70 also shows the deviations from signal linearity expected for jets reconstructed at the electromagnetic energy scale, i.e. without any hadronic calibration applied. In this case, the reconstructed jet signals correspond to only $\sim 65\%$ (at the lowest energies) to $\sim 80\%$ (at the highest energies) of the true jet energy.

The fractional energy resolution for the same jets, again after global calibration, is shown as a function of E_{truth} and for two different η-regions in figure 10.71. In addition, the resolution for a smaller cone size $\Delta R = 0.4$ is shown. The curves show the results of a three-parameter fit to the

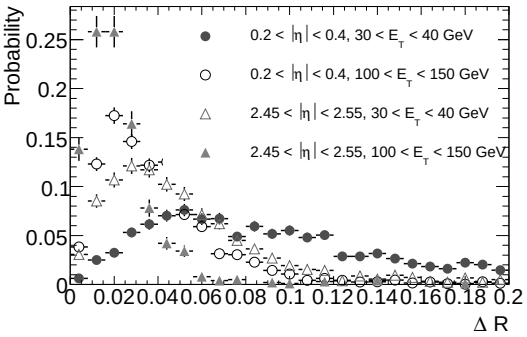

Figure 10.72: For cone-tower jets reconstructed with $\Delta R = 0.7$, distribution of ΔR between reconstructed and matched particle jet axes for two different transverse energy and η-ranges.

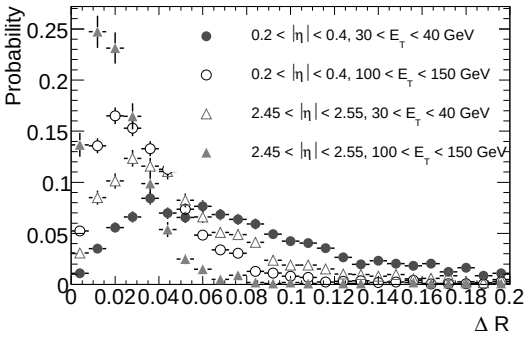

Figure 10.73: For cone-cluster jets reconstructed with $\Delta R = 0.7$, distribution of ΔR between reconstructed and matched particle jet axes for two different transverse energy and η-ranges.

energy resolution function:

$$\frac{\sigma}{E} = \sqrt{\frac{a^2}{E} + \frac{b^2}{E^2} + c^2} \tag{10.5}$$

For central jets in the region $0.2 < |\eta| < 0.4$, the stochastic term is $\approx 60\%\sqrt{\text{GeV}}$, while the high-energy limit of the resolution, expressed by the constant term c, is $\approx 3\%$ with the current global calibration. One important contribution to the η-dependence of the jet energy resolution is the noise, which varies quite rapidly due to the increasing readout-cell size and the change in calorimeter technology in the hadronic calorimeters from the low-noise tile calorimeter to the (higher-noise) LAr calorimeter with increasing η. The noise term b in the energy resolution function is found to increase from 0.5 GeV to 1.5 GeV when going from the barrel to the end-cap η-ranges shown in figure 10.71.

10.5.4.2 Jet direction measurement

The highly granular ATLAS calorimeters provide a precise measurement not only of the jet energy, but also of the jet direction together with the knowledge of the primary vertex position from the inner detector (see section 10.2.4). Figures 10.72 and 10.73 show very similar distributions of the distance ΔR between reconstructed and matched truth-particle jet directions for tower and cluster cone jets with $\Delta R = 0.7$ in two different pseudo-rapidity regions and two different transverse energy ranges. The choice of calorimeter signal obviously does not significantly affect the direction reconstruction of the jet. The general conclusion is that for both tower and cluster jets with transverse energies above 100 GeV, basically all reconstructed jets fall within the default matching cuts, $\Delta R < 0.2$. At lower transverse energies, however, it is clear that the precision with which the jet axis is reconstructed is degraded and a non-negligible fraction of reconstructed jets will fall outside the default matching cut. This issue is rediscussed below in section 10.5.5 with wider matching cuts to assess the efficiency and purity of reconstruction of low-p_T jets.

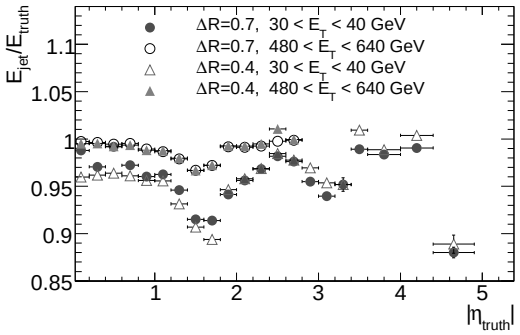

Figure 10.74: Signal uniformity for QCD di-jets in two different E_T ranges, as a function of $|\eta|$ of the matched truth-particle jet. The results are shown for cone-tower jets with $\Delta R = 0.7$ and $\Delta R = 0.4$.

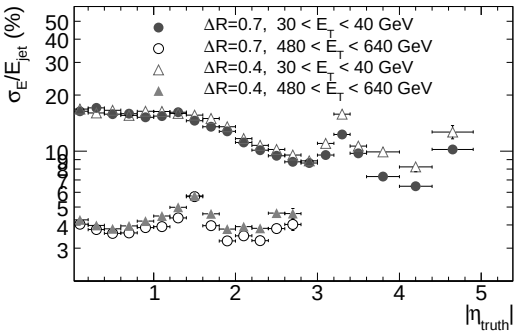

Figure 10.75: Jet energy resolution for QCD di-jets in two different E_T ranges, as a function of $|\eta|$ of the matched truth-particle jet. The results are shown for cone-tower jets with $\Delta R = 0.7$ and $\Delta R = 0.4$.

10.5.4.3 Jet signal uniformity

The variation of the jet energy response as a function of the jet direction is a measure of the uniformity of the jet signal across the full rapidity coverage of the calorimeters. Figure 10.74 shows for tower jets the ratio of reconstructed to matching truth-particle energy as a function of $|\eta|$ for jets in two different bins of E_T. The dips in response, corresponding to the two transition regions, $1.2 < |\eta| < 2.0$ and $2.8 < |\eta| < 3.4$, are much more apparent at low transverse energies. The dip in response in the last η-bin is a reflection of the limited fiducial coverage of jet reconstruction for $|\eta| > 4.4$. The η-dependence of the corresponding fractional energy resolution in figure 10.75 can be understood: the energy E_{jet} of jets with $30 < p_T < 40\,\text{GeV}$ increases from $E_{\text{jet}} = 30\,\text{GeV}$ at $|\eta| = 0$ to $E_{\text{jet}} \approx 1.8\,\text{TeV}$ at $|\eta| = 4.5$. Following the parametrisation in eq. (10.5), the fractional energy resolution, σ/E, improves dramatically over this energy range. The energy-dependent stochastic, $a/\sqrt{E}$, and noise, b/E, terms dominate over a large part of the kinematic regime. For jets with $480 < p_T < 640\,\text{GeV}$, the jet energy range is $480 \leq E_{\text{jet}} < 7000\,\text{GeV}$ from $|\eta| = 0$ up to $|\eta| \approx 3.1$, which is the kinematic limit at the LHC. In this region, σ/E is essentially independent of E_{jet}, i.e. dominated by the constant term, $c \gg a/\sqrt{E} \gg b/E$.

10.5.5 Jet reconstruction performance

The evaluation of the jet reconstruction performance includes not only the required signal features discussed above, but also parameters which are more oriented towards physics analysis, such as jet-finding efficiency and purity, jet vetoing, and jet tagging.

The jet reconstruction efficiency is defined as:

$$\varepsilon(\Delta R_m) = \frac{\text{\# matches of truth particle jets with reconstructed jets}}{\text{\# truth particle jets}} = \frac{N_m^{\text{jets}}(\Delta R_m)}{N_{\text{truth}}^{\text{jets}}}, \qquad (10.6)$$

where $\Delta R_m = \sqrt{(\eta_{\text{reco}} - \eta_{\text{truth}})^2 + (\phi_{\text{reco}} - \phi_{\text{truth}})^2}$ is the chosen matching radius (typically

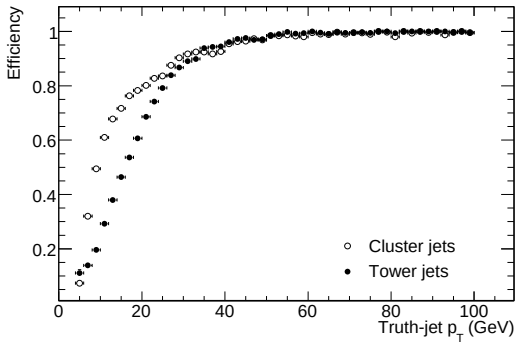

Figure 10.76: Efficiency of jet reconstruction in VBF-produced Higgs-boson events as a function of p_T of the truth-particle jet for cone-tower and cone-cluster jets with $\Delta R = 0.7$.

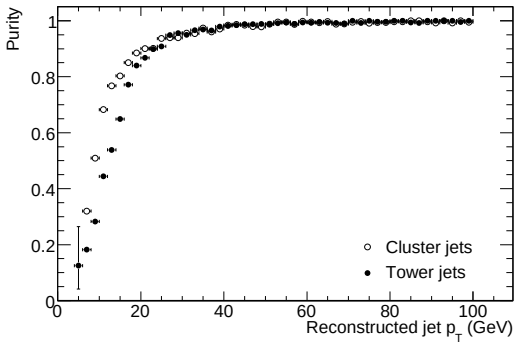

Figure 10.77: Purity of jet reconstruction in VBF-produced Higgs-boson events as a function of p_T of the reconstructed jet for cone-tower and cone-cluster jets with $\Delta R = 0.7$.

$\Delta R_m = 0.2$). The purity π of the jet reconstruction can be expressed as:

$$\pi(\Delta R_m) = \frac{\#\text{ matches of truth particle jets with reconstructed jets}}{\#\text{ reconstructed jets}} = \frac{N_m^{\text{jets}}(\Delta R_m)}{N_{\text{reco}}^{\text{jets}}}. \qquad (10.7)$$

The fake jet reconstruction rate f is then simply $f = 1 - \pi(\Delta R_m)$. In all cases, only one match is allowed for each reference jet. In case of two or more nearby jets, the one closest to the chosen reference is taken.

The two different calorimeter signal definitions used for jet reconstruction (towers and clusters) are expected to produce different efficiencies and purities. This is particularly important for searches for specific exclusive final states, where the requirement that no additional jet be present in the event is often used as a powerful tool to reject certain backgrounds. For example, one of the interesting production channels for the Higgs boson is vector-boson fusion (VBF), which has a very characteristic final state with two forward-going quark jets (often called tag jets) and, for non-hadronic Higgs-boson decay modes, no jets from the hard-scattering process itself in the central region of the detector. In this specific case, the efficiency of the jet-finding in the forward region, as defined in eq. (10.6), is a measure of the jet-tagging probability. The purity of the jet reconstruction in the central region then measures the efficiency for vetoing low-p_T jets.

The resulting efficiencies and purities are shown for cone-tower and cone-cluster jets with $\Delta R = 0.7$, respectively, as a function of p_T and y in figures 10.76, 10.77, 10.78 and 10.79 for the specific case of VBF produced $H \rightarrow \tau\tau$ decays with $m_H = 120\,\text{GeV}$ and for a looser matching radius $\Delta R_m = 0.5$ (see eq. (10.6) and (10.7)). These results show that for $p_T > 40\,\text{GeV}$, the performances of the tower and cluster jets are very similar. For lower values of p_T, however, the cluster jets are found with both higher efficiency and purity than tower jets.

For jets reconstructed with $p_T > 10\,\text{GeV}$, the fake rates in the central region are quite high, ranging from 30% for cluster jets to 45% for tower jets. In the forward regions, the jet-tagging efficiencies are close to 90% for cluster jets while they are only around 50% for tower jets with,

2008 JINST 3 S08003

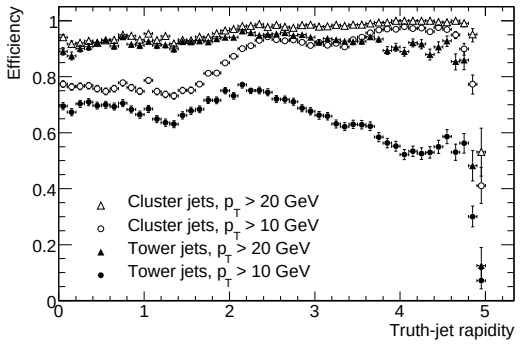

Figure 10.78: Efficiency of jet reconstruction in VBF-produced Higgs-boson events as a function of the rapidity y of the truth-particle jet for $p_T^{\text{jet}} > 10\,\text{GeV}$ and $p_T^{\text{jet}} > 20\,\text{GeV}$ and for cone-tower and cone-cluster jets with $\Delta R = 0.7$.

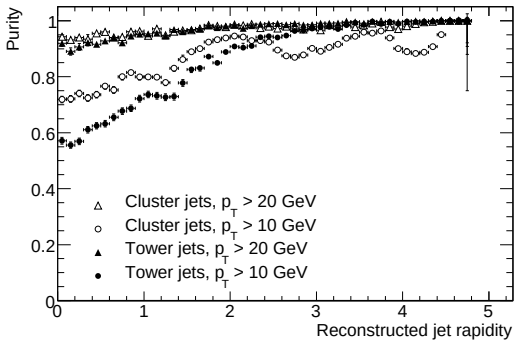

Figure 10.79: Purity of jet reconstruction in VBF-produced Higgs-boson events as a function of the rapidity y of the reconstructed jet for $p_T^{\text{jet}} > 10\,\text{GeV}$ and $p_T^{\text{jet}} > 20\,\text{GeV}$ and for cone-tower and cone-cluster jets with $\Delta R = 0.7$.

however, significantly higher fake rates of $\sim 10\%$ for the cluster jets. These results are clearly also quite sensitive to pile-up, so it is important to stress here that the numbers above apply only for initial data-taking at luminosities between 10^{31} cm^{-2} s^{-1} and 10^{33} cm^{-2} s^{-1}.

10.5.6 Validation of jet calibration with in-situ measurements

There are several final states at the LHC which provide signals for validation of the jet energy calibration, and, in some cases, even the extraction of further corrections. In general, final states with a well measured electromagnetic object balancing one or more jets in transverse momentum, such as in $\gamma+\text{jet(s)}$ and $Z+\text{jet(s)}$ events, are good choices for this task. The $\gamma+\text{jet(s)}$ process provides high statistics in the transverse momentum range from 40 to 400 GeV, but lower purity than the $Z+\text{jet(s)}$ process, which should, however, cover precisely the lower edge of the transverse momentum range, up to 100 GeV.

As an example, one approach to measure the jet response using $\gamma+\text{jet(s)}$, which has been developed at the Tevatron, is the missing transverse momentum projection fraction. The basic idea of this method is to project the hadronic transverse-momentum vectors onto the transverse-momentum vector of the photon and to measure the apparent E_T^{miss} fraction. In events where the photon is back-to-back with the jet (to better than approximately ten degrees in ϕ, the jet response R_{jet} can then be determined by

$$R_{\text{jet}} = -\frac{\sum_{\text{signals}} \vec{p}_{T,\text{had}} \cdot \hat{\eta}_\gamma}{p_{T,\gamma}} \,. \tag{10.8}$$

Here $\hat{\eta}_\gamma = \vec{p}_{T,\gamma}/p_{T,\gamma}$ is the direction of the photon in the transverse event plane. The hadronic transverse momentum can be calculated using the reconstructed jet(s) ($\vec{p}_{T,\text{had}} = \vec{p}_{T,\text{jet}}$), or just using the sum of cluster signals without the jet context ($\vec{p}_{T,\text{had}} = \vec{p}_{T,\text{calo}}$). Figure 10.80 shows the jet response for cone-tower jets with $\Delta R = 0.4$ at the electromagnetic energy scale, as a function of the jet energy, for simulated $\gamma+\text{jet}$ events. This variable can be measured directly and can thus become

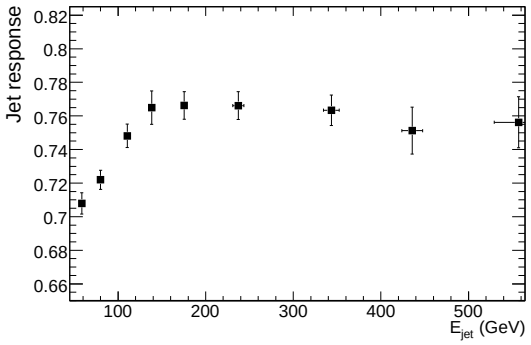

Figure 10.80: Jet response for seeded cone-tower jets ($\Delta R = 0.4$) in $\gamma+$jet events, averaged over η and calculated by the missing transverse momentum fraction method, as a function of the jet energy. The calorimeter signals are reconstructed at the electromagnetic energy scale.

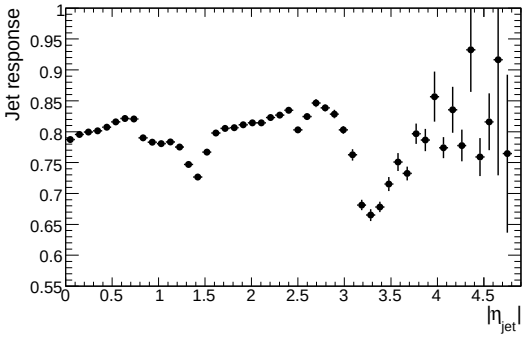

Figure 10.81: Jet response for seeded cone-tower jets ($\Delta R = 0.4$), in $\gamma+$jet events, averaged over jet energy and calculated by the missing transverse momentum fraction method, as a function of the jet direction, $|\eta_{\text{jet}}|$. The calorimeter signals are reconstructed at the electromagnetic energy scale. The degraded response in the calorimeter crack regions is clearly visible.

the basis for a global jet energy scale calibration derived from collision data. The η-dependence of the jet response for the same jets and events is shown in figure 10.81. The shape of the response clearly indicates the effect of the crack regions of the ATLAS calorimeter system on the jet energy measurement.

The other important final state for jet calibration are hadronically decaying W bosons ($W \to qq$), which in ATLAS can only be used with high purity in $t\bar{t}$ production. Here, m_W constrains the energy scale of the two quark jets. Figure 10.82 shows the ratio between the reconstructed di-jet mass from $W \to jj$ decays and the nominal W-boson mass as a function of the true transverse momentum, p_T^W, of the W-boson. For the nominal selection cuts used to reconstruct $t\bar{t}$ events, this ratio departs significantly from unity at low values of p_T^W because of the high p_T-threshold of 40 GeV applied to the jets, as illustrated in figure 10.82. With further in-situ corrections aimed at re-scaling jet energies as a function of $|\eta|$ to obtain a uniform response, e.g. as shown in figure 10.81, a linearity of better than 2% can be achieved up to values of p_T^W as high as 200 GeV.

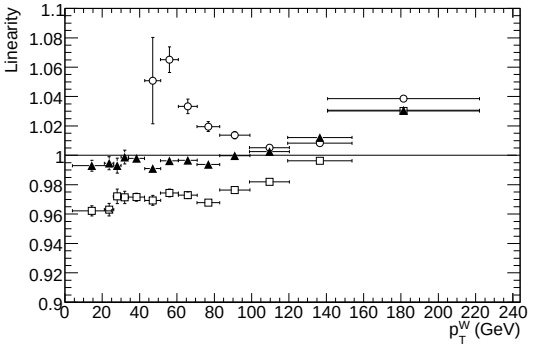

Figure 10.82: Ratio of the reconstructed di-jet mass from $W \to jj$ decays in $t\bar{t}$ events to the nominal mass as a function of the transverse momentum of the W-boson, p_T^W, for globally calibrated cone-tower jets with $\Delta R = 0.7$. Shown are the results for the nominal jet-selection cuts, $p_T > 40$ GeV (open circles), for jets reconstructed with $p_T > 10$ GeV (open squares) and for jets re-scaled to obtain a more uniform response as a function of $|\eta|$ (full triangles).

2008 JINST 3 S08003

10.6 Missing transverse energy

A very good measurement of the missing transverse energy, E_T^{miss}, is a critical requirement for the study of many physics channels in ATLAS, in particular in the search for signals from new physics such as supersymmetry or extra dimensions. A good E_T^{miss} measurement in terms of linearity and accuracy is also important for the reconstruction of the top-quark mass from $t\bar{t}$ events with one top quark decaying semi-leptonically. It is crucial for the efficient and accurate reconstruction of the Higgs-boson mass when the Higgs boson decays to a pair of τ-leptons, the most prominent example being the supersymmetric Higgs boson A. Another important requirement on the measurement of E_T^{miss} is to minimise the impact of tails induced by imperfections in the detector coverage or detector response. The η-coverage of the forward calorimeters minimises by design any tails from particles escaping at very large η, but there are several transition regions in the calorimetry, which will lead to incorrect measurements of E_T^{miss} in a certain fraction of the cases. This could significantly enhance for example the backgrounds from QCD multi-jet events to a possible signal from supersymmetry or the backgrounds from $Z \rightarrow ll$ decays accompanied by high-p_T jets to a possible signal from Higgs-boson decay into two leptons and two neutrinos. This section describes briefly the reconstruction and calibration of E_T^{miss} in ATLAS, illustrates the expected performance with a few examples, and finally concludes with a discussion of the possible sources of fake E_T^{miss}.

10.6.1 Reconstruction and calibration of E_T^{miss}

The E_T^{miss} reconstruction in ATLAS is based in a first step on the calibrated calorimeter cell energies (following the global calibration scheme described in section 10.5.3) and on the reconstructed muons. The E_T^{miss} muon term is calculated from the momenta of the muons measured using the stand-alone muon-spectrometer reconstruction (see section 10.3). Energy lost by muons in the calorimeter is thus not double-counted, since it is only taken into account in the calorimeter term. Only good-quality muons with a matched track in the inner detector are considered, which reduces considerably possible contributions from fake muons, sometimes created from high hit multiplicities in the muon spectrometer in events with very energetic jets.

In a second step, the E_T^{miss} reconstruction accounts for the so-called cryostat term, which corrects for the energy lost in the cryostat between the barrel LAr electromagnetic and tile calorimeters. This correction is applied following the recipe described in section 10.5.3 and eq. (10.4) and is found to be non-negligible for high-p_T jets: it represents a 5% contribution per jet with p_T above 500 GeV.

In a final step, a refined calibration of E_T^{miss} is performed through the association of each high-p_T object in the event to its globally calibrated cells. Starting from the reconstructed identified objects in a carefully chosen order, namely electrons, photons, hadronically decaying τ-leptons, b-jets, light jets and muons, each calorimeter cell is associated to its parent high-p_T object. The refined calibration of E_T^{miss} then replaces the initial contribution from globally calibrated cells by the contribution from the corresponding calibrated high-p_T objects themselves. The cells which survive a noise cut optimised in terms of E_T^{miss} measurements and which do not contribute to any reconstructed object are also calibrated using the global calibration scheme and accounted for in the E_T^{miss} calculation.

2008 JINST 3 S08003

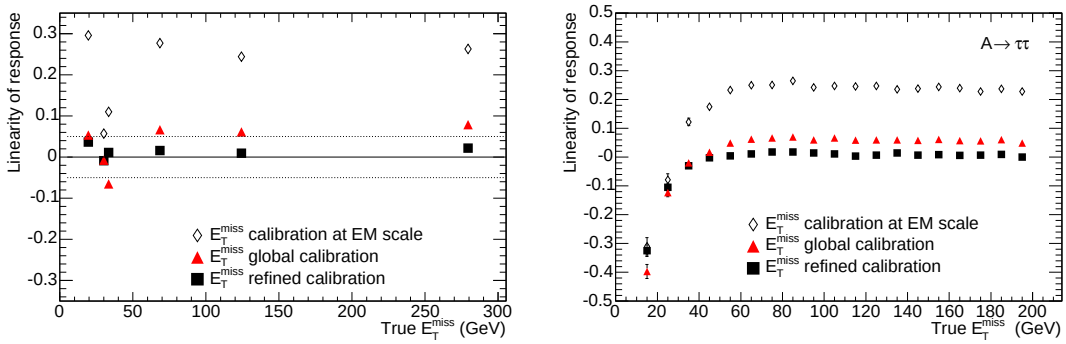

Figure 10.83: Linearity of response for reconstructed E_T^{miss} as a function of the average true E_T^{miss} for different physics processes covering a wide range of true E_T^{miss} and for the different steps of E_T^{miss} reconstruction (see text). The points at average true E_T^{miss} of 20 GeV are from $Z \rightarrow \tau\tau$ events, those at 35 GeV are from $W \rightarrow e\nu$ and $W \rightarrow \mu\nu$ events, those at 68 GeV are from semi-leptonic $t\bar{t}$ events, those at 124 GeV are from $A \rightarrow \tau\tau$ events with $m_A = 800$ GeV, and those at 280 GeV are from events containing supersymmetric particles at a mass scale of 1 TeV (left). Linearity of response for reconstructed E_T^{miss} as a function of the true E_T^{miss} for $A \rightarrow \tau\tau$ events with $m_A = 800$ GeV (right).

10.6.2 Evaluation of E_T^{miss} performance

The E_T^{miss} performance is evaluated by comparing the final reconstructed and calibrated value of E_T^{miss} with the true E_T^{miss}, calculated using all stable and non-interacting particles in the final state, for a number of physics processes of interest, involving a variety of topologies and final states over a wide range of energies. Although this evaluation focuses primarily on the linearity of response and on resolution, other features, such as the direction of the E_T^{miss} vector (in the transverse plane) and tails in the measurement of E_T^{miss} have also been carefully studied.

The expected performance in terms of E_T^{miss} linearity of response as a function of true E_T^{miss} is shown for a number of physics processes of interest in figure 10.83. The evolution of the linearity of response is illustrated for each of the major steps in the E_T^{miss} reconstruction described above:

- the uncalibrated E_T^{miss} corresponds to the use of cell energies at the electromagnetic scale, which therefore creates a large systematic bias of 10–30% in the response (the bias is smaller for events containing little hadronic activity on average, such as $W \rightarrow e\nu$ and $W \rightarrow \mu\nu$ decays);
- the reconstructed E_T^{miss} based on globally calibrated cell energies and reconstructed muons provides a correct response to within 5%;
- the reconstructed E_T^{miss} including in addition the cryostat correction provides excellent linearity of response for all processes except $W \rightarrow e\nu$;
- the refined E_T^{miss} calibration in the specific case of $W \rightarrow e\nu$ events amounts to correcting the globally calibrated cells of the electron shower back to the electromagnetic scale and the linearity of response is then also restored in this case.

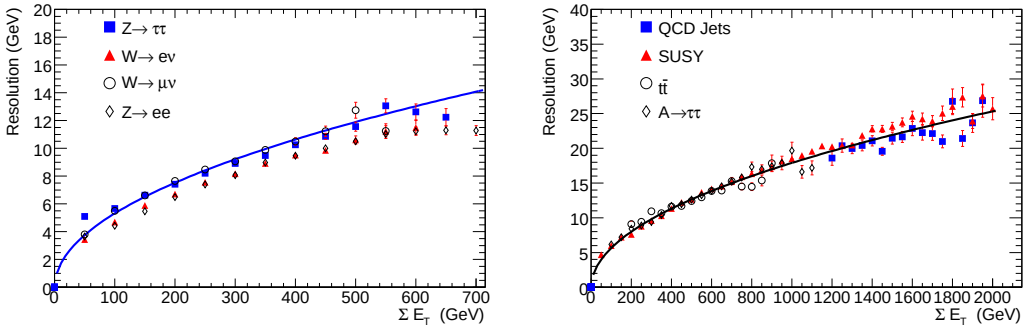

Figure 10.84: Resolution σ of the two components (x, y) of the E_T^{miss} vector after refined calibration as a function of the total transverse energy, ΣE_T, measured in the calorimeters for different physics processes corresponding to low to medium values of ΣE_T (left) and to higher values of ΣE_T (right). The curves correspond respectively to the best fit, $\sigma = 0.53\sqrt{\Sigma E_T}$, through the points from $Z \rightarrow \tau\tau$ events (left) and to the best fit, $\sigma = 0.57\sqrt{\Sigma E_T}$, through the points from $A \rightarrow \tau\tau$ events (right). The points from $A \rightarrow \tau\tau$ events are for masses m_A ranging from 150 to 800 GeV and the points from QCD jets correspond to di-jet events with $560 < p_T < 1120$ GeV.

Figure 10.84 shows that the E_T^{miss} resolution σ follows an approximate stochastic behaviour over a wide range of values of the total transverse energy deposited in the calorimeters. A simple fit to a function $\sigma = a \cdot \sqrt{\Sigma E_T}$ yields values between 0.53 and 0.57 for the parameter a, for ΣE_T values between 20 and 2000 GeV. The refined E_T^{miss} calibration yields somewhat better results for the E_T^{miss} resolution for e.g. $W \rightarrow e\nu$ decays. Departures from this simple behaviour are expected and observed for low values of ΣE_T where noise plays an important contribution and for very high values of ΣE_T where the constant term in the jet energy resolution dominates.

10.6.3 Measurement of E_T^{miss} direction

Figure 10.85 shows the E_T^{miss} azimuthal angular resolution as a function of the true E_T^{miss} for three different physics processes. The measurement of the E_T^{miss} azimuth is clearly more accurate for $W \rightarrow e\nu$ events, which contain in general one high-p_T electron and moderate hadronic activity in addition, than for $t\bar{t}$ events, which contain much more hadronic activity. Figure 10.85 also shows that, for values of the true E_T^{miss} below 40 GeV, the accuracy on the measurement of the direction of a E_T^{miss} vector with small modulus degrades rapidly. In contrast, for high values of the true E_T^{miss}, azimuthal accuracies below 100 mrad can be achieved.

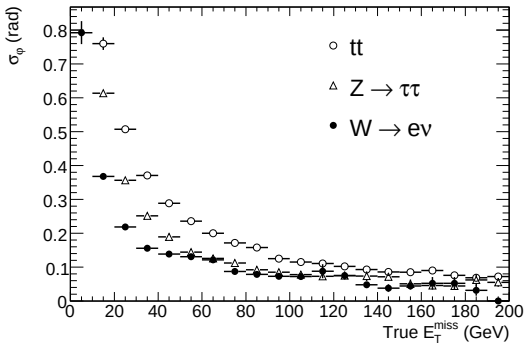

Figure 10.85: Accuracy of the measurement of the azimuth of the E_T^{miss} vector as a function of the true E_T^{miss} for three different physics processes: semi-leptonic $t\bar{t}$ events, $Z \rightarrow \tau\tau$ and $W \rightarrow e\nu$ events.

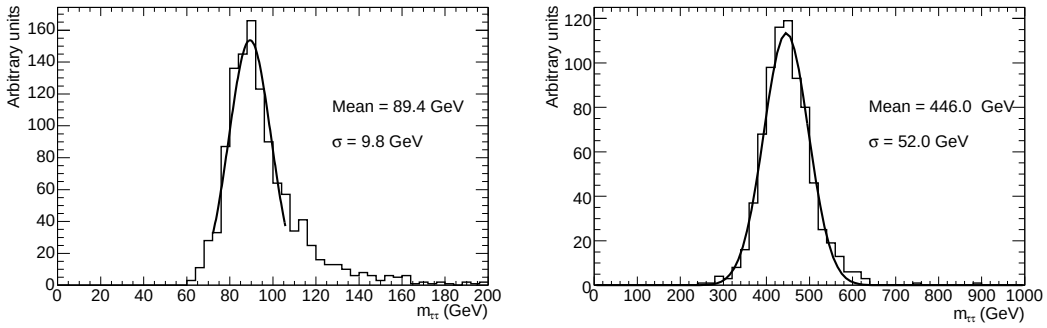

Figure 10.86: Expected distributions for the reconstructed invariant mass of τ-lepton pairs, with one τ-lepton decaying to a lepton and the other one decaying to hadrons. The results are shown for $Z \rightarrow \tau\tau$ decays (left) and for $A \rightarrow \tau\tau$ decays with $m_A = 450\,\text{GeV}$ (right).

As discussed in section 10.6.5, large fluctuations in the jet energy measurements, due in particular to cracks in the fiducial acceptance of the calorimeters, may lead to fake E_T^{miss} with a vector of large modulus pointing in the same direction as the mis-measured jet in the azimuthal plane. A good accuracy on the measurement of the E_T^{miss} azimuth will therefore be needed to apply a cut, requiring that the measured E_T^{miss} vector be isolated from all high-p_T jets in the event, with a high efficiency for signal events with large true E_T^{miss}.

10.6.4 Use of E_T^{miss} for mass reconstruction

The reconstructed E_T^{miss} vector can be used to improve the overall reconstruction of final-state topologies with only one neutrino in the final state (e.g. in $t\bar{t}$ events with one hadronic and one semi-leptonic top-quark decay). But, under certain simplifying assumptions and only for pairs which are not back-to-back [273, 274], one can even use the reconstructed E_T^{miss} vector in $Z \rightarrow \tau\tau$ and $A \rightarrow \tau\tau$ decays, despite the presence of several neutrinos in the final state, to reconstruct the invariant mass of the $\tau\tau$ pair. The results of such a procedure are shown in figure 10.86 for the reconstruction of $Z \rightarrow \tau\tau$ and $A \rightarrow \tau\tau$ decays with $m_A = 450\,\text{GeV}$, where A is a super-symmetric Higgs boson. The reconstructed masses are correct to $\sim 2\%$ and the mass resolution is approximately 11%. Nevertheless, significant tails remain in the distributions because of the highly non-Gaussian effects induced by mis-measurements of E_T^{miss} and by the approximations used.

10.6.5 Fake E_T^{miss}

Fake E_T^{miss}, defined simply as the difference between reconstructed and true E_T^{miss}, can arise at a significant level from a number of different sources: beam-gas scattering and other machine backgrounds, displaced interaction vertices, hot/dead/noisy cells (or regions) in the calorimeters, and mis-measurements in the detector itself, due to high-p_T muons escaping outside the fiducial acceptance of the detector (see also section 10.3) and to large losses of deposited energy in cracks or inactive materials (see also section 10.5.4.3). These latter two effects might effectively limit the performance of the E_T^{miss} reconstruction in the longer term and have therefore been studied in detail.

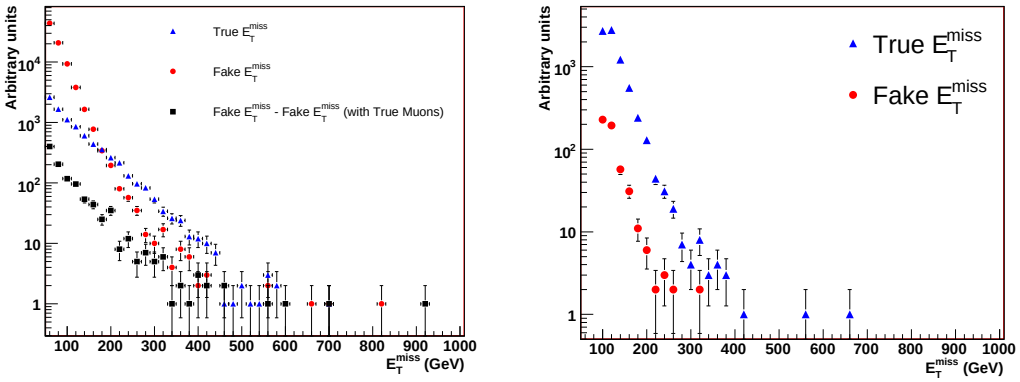

Figure 10.87: For QCD di-jet events containing at least one jet with $560 < E_T < 1120$ GeV, distribution of fake E_T^{miss} (circles), calculated as the difference between reconstructed and true E_T^{miss}, compared to the true E_T^{miss} (triangles) expected in this di-jet sample (left). Also shown is the distribution of fake E_T^{miss} due to muons (squares), calculated as the difference between the fake E_T^{miss} and the residual fake E_T^{miss} obtained using only the true muons in the event. The fake and true E_T^{miss} distributions are shown (right) after applying an isolation cut on the azimuth of the reconstructed E_T^{miss} vector . This cut requires that the distance in azimuth between the reconstructed E_T^{miss} vector and the direction of any high-p_T jet reconstructed in the event be larger than 17°.

Figure 10.87 shows the distributions of fake and true E_T^{miss} for QCD di-jet events containing at least one jet with $560 < E_T < 1120$ GeV and for two cases: in the first case, all events are considered and figure 10.87 shows that fake E_T^{miss} dominates the spectrum up to true E_T^{miss} values of 200 GeV for this particular sample. In the second case, events are considered only if the reconstructed E_T^{miss} vector is isolated in azimuth from all reconstructed jets in the event. The isolation cut requires that the distance in azimuth between the reconstructed E_T^{miss} vector and the direction of any high-p_T jet reconstructed in the event be larger than 17°. In this case, true E_T^{miss} dominates the spectrum even for true E_T^{miss} values well below 100 GeV. These results confirm that the main source of fake E_T^{miss} in these events arises from mis-measurements of jets in certain regions of the calorimeter.

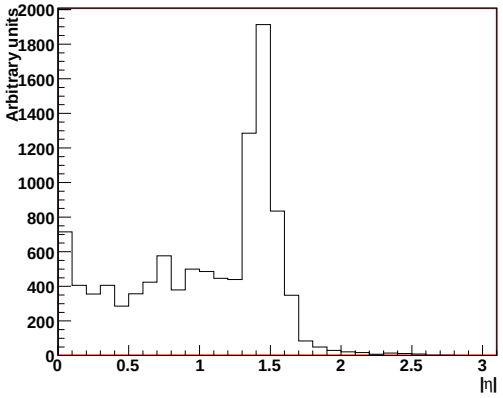

Figure 10.88: For QCD di-jet events containing at least one jet with $560 < E_T < 1120$ GeV and with a fake E_T^{miss} larger than 100 GeV, distribution of $|\eta|$ of the mis-measured jet.

For those events with a fake E_T^{miss} larger than 100 GeV, figure 10.88 shows the distribution of $|\eta|$ of the mis-measured jet, defined as the jet which deviates the most from its matching truth jet in terms of its energy measurement. Clear excesses of mis-measured jets are observed around $\eta = 1.5$ (crack region) and around $\eta = 0$ (sensitive region for calibration of the overall calorimeter

response). As already shown in figure 10.87, these excesses can be significantly reduced with simple topological cuts, but other tools can also reduce them further if required, such as the use of jets reconstructed from tracks to further improve the isolation in azimuth of the reconstructed E_T^{miss}.

10.7 Hadronic τ-decays

Hadronic decays of τ-leptons will play an important role at the LHC, especially as probes for new phenomena spanning a wide range of theoretical models. Based on this motivation, two complementary approaches, one track-based and the other calorimeter-based (see section 10.7.3), have been developed to efficiently reconstruct and identify these decays, whilst providing the required large rejection against the otherwise overwhelming backgrounds from hadronic jets. The equally difficult task of triggering on these decays as inclusively as possible is addressed in section 10.9.

In general, hadronically decaying τ-leptons are reconstructed by matching narrow calorimeter clusters with a small number of tracks. Specific analyses may require exactly one or three tracks with total charge consistent with the charge of a τ-lepton, and, if more than one, the tracks may be required to be quite collimated and to be consistent with originating from a common secondary vertex. The visible reconstructed energy of the hadronically decaying τ-lepton is concentrated in a narrow cone around the leading (highest-p_T) track (typically a cone of half-angle $\Delta R = 0.2$ is sufficient to collect this energy). It can be estimated using only the calorimeter information or using a more refined scheme (often called energy flow), which combines the reconstructed track momenta with the energy of localised electromagnetic clusters within the chosen narrow cone.

Several key variables, which are characteristic of the properties of hadronic τ-decays, are used for the purpose of identification: the profile of the shower in the electromagnetic calorimeter, the isolation of the narrow calorimeter cluster used to identify the τ-candidate, the number and energy-weighted width of strips, the ratio between the transverse energy deposited in the calorimeter and the transverse momentum of the leading track, the number of associated tracks (passing some quality criteria), the momentum-weighted width and invariant mass of the track system and the signed impact parameter significance. Both traditional cut-based selections and multi-variate discrimination techniques (likelihood, neural networks, etc.) have been applied to this set of identification variables (see section 10.7.3).

Two specific performance aspects of particular interest for the reconstruction of hadronic τ-decays are first discussed in this section and are followed by the more general discussion of the overall performance in terms of reconstruction and identification efficiency versus rejection of the large backgrounds from QCD jets expected at the LHC.

10.7.1 Track reconstruction in hadronic τ-decays

The efficiency and quality of the track reconstruction in the inner detector are discussed in some detail in section 10.2. For hadronic τ-decays from a representative sample of $W \rightarrow \tau\nu$ and $Z \rightarrow \tau\tau$ decays studied with the track-based algorithm, particular attention has been given to minimise the amount of charge misidentification and of migration between the single- and three-prong categories in the reconstruction. In the low-p_T range, the performance is degraded due to hadronic interactions in the inner-detector material (see for example figure 10.12). For hadronic

2008 JINST 3 S08003

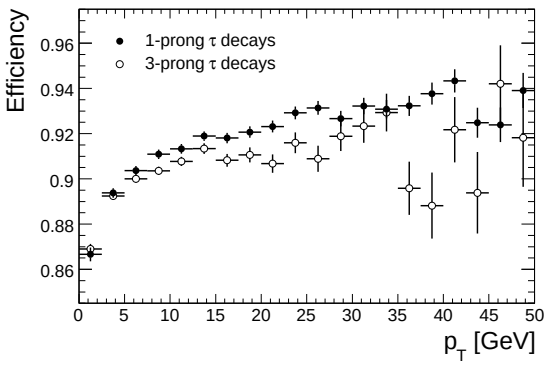

Figure 10.89: Reconstruction efficiency for charged-pion tracks as a function of the pion transverse momentum for single- and three-prong hadronic τ-decays from $W \rightarrow \tau\nu$ and $Z \rightarrow \tau\tau$ signal samples.

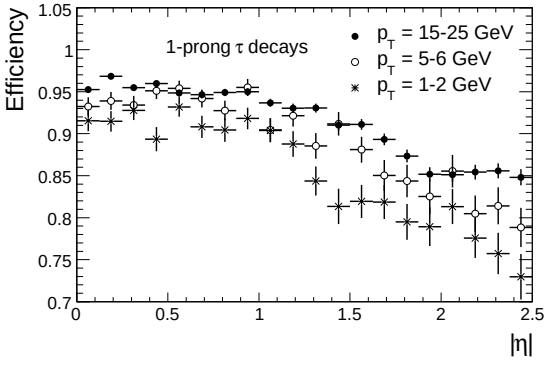

Figure 10.90: Reconstruction efficiency for the charged-pion track as a function of $|\eta|$ for three different ranges of pion p_T, for single-prong hadronic τ-decays from $W \rightarrow \tau\nu$ and $Z \rightarrow \tau\tau$ signal samples.

τ-decays with high energy, the performance for three-prong decays will be degraded due to the strong collimation of the tracks. Figures 10.89 and 10.90 show the efficiency for reconstructing tracks from single-prong and three-prong τ-decays for τ-leptons from W/Z-boson decays as a function of the track transverse momentum and pseudorapidity. The quality criteria used are the standard ones discussed in section 10.2.3 and the results shown in figure 10.90 are in agreement with those shown for single particles in figure 10.13, except for three-prong τ-decays at high energy for which a degradation in efficiency is observed.

The charge of the identified hadronic τ-decay is determined as the sum of the reconstructed track charges. For the leading track, which is required e.g. by the track-based algorithm to have a transverse momentum larger than 9 GeV, charge misidentification is limited to $\sim 0.2\%$ with the standard quality cuts. The overall charge misidentification probability for the τ-lepton is, however, dominated by combinatorial effects: single-prong decays may migrate to the three-prong category due to photon conversions or the presence of additional tracks from the underlying event, or a three-prong decay may be reconstructed as a single-prong decay due to inefficiencies of the track reconstruction and selection. This overall misidentification is estimated to be below $\sim 3\%$ without requiring further quality cuts.

The rejection of leptonic τ-decays misidentified as single-prong hadronic τ-candidates is based on dedicated algorithms optimised to veto electrons and muons in the kinematic configurations of interest here. The rejection obtained against electron tracks from $W \rightarrow e\nu$ decays is approximately 50 for a τ-efficiency of 95%. Using only information from the calorimeter combined with the inner detector, the rejection obtained against muons from $W \rightarrow \mu\nu$ decays is sufficient, reaching a value of approximately 30 for a τ-efficiency of 99%.

10.7.2 Electromagnetic clusters in single-prong decays

Because of the very fine granularity of the electromagnetic calorimeter, electromagnetic clusters created by showers from photons from π^0 decays can be identified and measured with reasonable

Table 10.5: Expected probabilities for observing a specific multiplicity of localised clusters in the electromagnetic calorimeter within the narrow cone ($\Delta R = 0.2$) used to identify the τ-candidate, for inclusive and exclusive single-prong hadronic τ-decays from $W \rightarrow \tau\nu$ and $Z \rightarrow \tau\tau$ signal samples,

Decay mode	No cluster	One cluster	More than one cluster
All single-prong τ-decays	32%	35%	33%
$\tau \rightarrow \pi^{\pm}\nu$	65%	20%	15%
$\tau \rightarrow \rho^{\pm}(\rightarrow \pi^0\pi^{\pm})\nu$	15%	50%	35%
$\tau \rightarrow a_1^{\pm}(\rightarrow 2\pi^0\pi^{\pm})\nu$	9%	34%	57%

efficiency and accuracy within the narrow cone used to reconstruct hadronic τ-decays. The results reported in this section have been obtained using the three-dimensional topological clustering described in more detail in section 10.5 applied only to the first two layers of the electromagnetic calorimeter.

As an example, in the case of single-prong decays, the reconstructed charged track in the inner detector and the reconstructed isolated clusters in the electromagnetic calorimeter may be used to obtain the energy and invariant mass of the visible products of the hadronic τ-decay. The resulting performance has been evaluated for $W \rightarrow \tau\nu$ decays and is shown in table 10.5 for inclusive single-prong decays and also for exclusive decays containing a ρ or a_1 meson compared to decays containing only one single charged pion. Figure 10.91 shows the response and resolution obtained by this algorithm for reconstructing the visible transverse energy from the τ-decay, in the cases where one such isolated electromagnetic cluster is identified: the response is correct to $\sim 2.5\%$ and the fractional energy resolution is $\sim 5\%$, i.e. far better than that obtained for normal hadronic jets in the same energy range of 20–50 GeV. In the cases where several such clusters are identified, their energy-weighted barycentre is calculated and the fractional energy resolution is somewhat degraded to $\sim 7\%$. Finally, in the cases where at least one such cluster is identified, figure 10.92 shows the reconstructed invariant mass of the system for three single-prong final states. The use of certain specific final states in hadronic τ-decays will be of great interest in polarisation and spin analyses in searches for new particles decaying into τ-leptons.

10.7.3 Identification of hadronic τ-decays and rejection of QCD jets

Two complementary algorithms for τ-identification and reconstruction have been studied, as outlined above:

- a track-based algorithm [275], which relies on tracks reconstructed in the inner detector and adopts an energy-flow approach. This algorithm has been optimised for visible transverse energies in the 10–80 GeV range, which corresponds to hadronic τ-decays from $W \rightarrow \tau\nu$ and $Z \rightarrow \tau\tau$ processes;

- a calorimeter-based algorithm [276], which relies on clusters reconstructed in the calorimeter and has been optimised for visible transverse energies above 30 GeV, which corresponds to hadronic τ-decays from heavy Higgs-boson production and decay.

2008 JINST 3 S08003

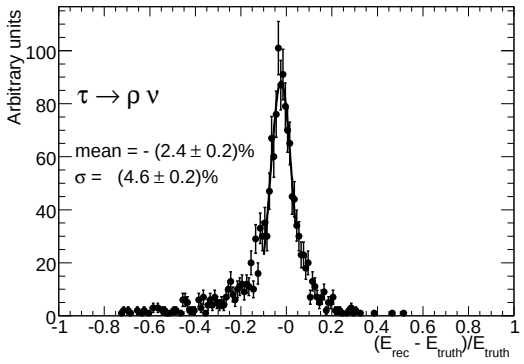

Figure 10.91: Energy response, expressed as the ratio $(E_{\text{rec}} - E_{\text{truth}}/E_{\text{truth}}$, where E_{rec} (resp. E_{truth}) are the reconstructed (resp. true) visible energies (see text), for single-prong hadronic τ-decays from a $W \rightarrow \tau\nu$ signal sample with one reconstructed electromagnetic cluster.

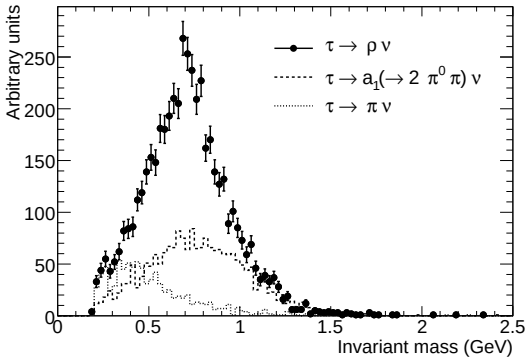

Figure 10.92: Distribution of reconstructed invariant mass of visible decay products (see text), for single-prong hadronic τ-decays from a $W \rightarrow \tau\nu$ signal sample with at least one reconstructed electromagnetic cluster.

Figures 10.93 and 10.94 show the expected performance of the two algorithms, expressed as curves describing jet rejection versus efficiency for single- and three-prong hadronic τ-decays separately and for different ranges of the visible transverse energy. The jet rejections are computed with respect to truth jets reconstructed using particle four-momenta within a cone of size $\Delta R = 0.4$. The behaviour of the respective rejection versus efficiency curves reflects the different optimisations performed for the two algorithms. Whereas the track-based algorithm has been tuned to preserve similar performance for single- and three-prong decays, the calorimeter-based algorithm has been tuned to provide the best possible rejection at medium-to-high energies and is therefore more performant for single-prong decays than the track-based algorithm. For an overall efficiency of 30% for single-prong decays, the rejection against jets is typically between 700 and 6000, as is illustrated more quantitatively and as a function of the visible transverse energy in table 10.6.

The track-based algorithm requires a good-quality track system, in which the leading track has transverse momentum above 9 GeV, as a seed for building a hadronic τ-candidate. This provides already after reconstruction considerable rejection against QCD jets with high track multiplicities. This is illustrated in figures 10.95 and 10.96, which show respectively the normalised track-multiplicity spectra for hadronic τ-candidates, with visible transverse energy above 20 GeV, from $Z \rightarrow \tau\tau$ decays and from QCD jets. The distributions are shown after the reconstruction step, after a cut-based identification algorithm and finally after applying a multi-variate discrimination technique using a neural network. The track multiplicity in the QCD jet sample is quite different from that in the signal sample, for any of the cuts applied. At the same time, figure 10.95 shows that the fractions of single-prong and three-prong decays in the signal sample approach those expected from an ideal signal sample: for single-prong (respectively three-prong) candidates, the fractions of correctly assigned decays improve from 87% (respectively 74%) after reconstruction to 91% (respectively 86%) after cut-based identification and to 92% (respectively 93%) after applying the neural-network discrimination technique.

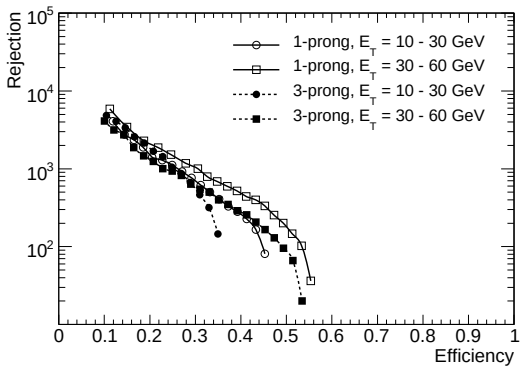

Figure 10.93: Expected rejection against hadronic jets as a function of the efficiency for hadronic τ- decays for the track-based algorithm using a neural-network selection. The results are shown separately for single- and three-prong decays and for two ranges of visible transverse energy.

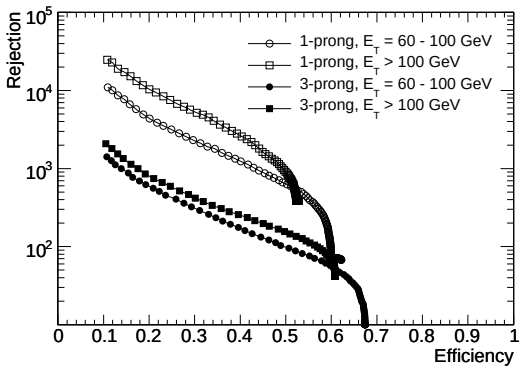

Figure 10.94: Expected rejection against hadronic jets as a function of the efficiency for hadronic τ- decays for the calorimeter-based algorithm using a likelihood selection. The results are shown separately for single- and three-prong decays and for two ranges of visible transverse energy.

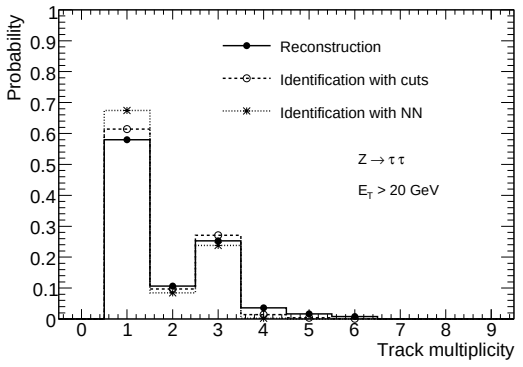

Figure 10.95: Track multiplicity distributions obtained for hadronic τ-decays with visible transverse energy above 20 GeV using the track-based τ-identification algorithm. The distributions are shown after reconstruction, after cut-based identification and finally after applying the neural network (NN) discrimination technique for an efficiency of 30% for the signal.

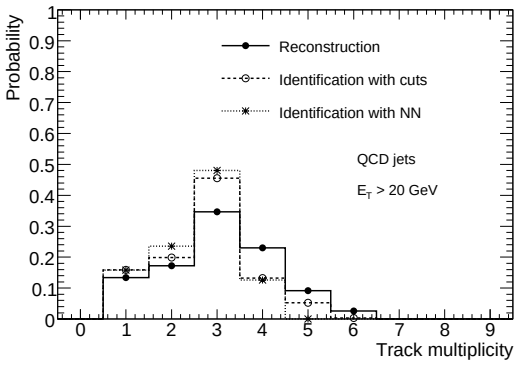

Figure 10.96: Track multiplicity distributions obtained for the background from QCD jets with visible transverse energy above 20 GeV using the track-based τ-identification algorithm. The distributions are shown after reconstruction, after cut-based identification and finally after applying the neural network (NN) discrimination technique for an efficiency of 30% for the signal.

2008 JINST 3 S08003

Table 10.6: Rejection of track-based and calorimeter-based τ-identification algorithms over the range of visible transverse energy in which they have been optimised. The values are given separately for single- and three-prong decays and for an efficiency of 30%. The quoted errors are statistical.

Algorithm		E_T = 10-30 GeV	E_T = 30-60 GeV	E_T = 60-100 GeV	E_T > 100 GeV
Track-based	1-prong	740±70	1030±160		
(neural network)	3-prong	590±50	590±70		
Calorimeter-based	1-prong		1130±50	2240±140	4370±280
(likelihood)	3-prong		187±3	310±7	423±8

Figures 10.95 and 10.96 also show that the candidates with track multiplicity above three may be used to normalise the QCD background. This would allow a reasonably precise calibration of the performance of the τ-identification algorithms using real data, provided the rejection against QCD jets is proven to be sufficient to extract a clean signal in the single-prong and three-prong categories. The sensitivity of such a method can be enhanced by also studying the track multiplicity outside the narrow cone used for τ-identification and combining this information with that presented in figure 10.96.

10.8 Flavour tagging

The ability to tag hadronic jets arising from heavy flavours is an important asset for many physics analyses, such as precision measurements in the top-quark sector and searches for Higgs bosons or other new physics signatures. This section describes the b-tagging performance which can be achieved using different methods [277]. In the results presented in this section, the impact of possible residual misalignements on the b-tagging performance has not been taken into account.

10.8.1 Ingredients of b-tagging algorithms

Except when explicitly stated otherwise, the results presented in this section are based on simulations without pile-up and with a perfect alignment of the inner detector. Jets are reconstructed in the calorimeters using standard algorithms (see section 10.5.1) and the jets with $p_T > 15$ GeV and $|\eta| < 2.5$ are considered for b-tagging. Only reconstructed tracks within a distance $\Delta R < 0.4$ from the jet axis are used for b-tagging.

To assess quantitatively the b-tagging performance, the Monte-Carlo truth is used to determine the type of parton from which a jet originates. This labelling procedure is somewhat ambiguous. For the results presented here, a quark-based labelling has been used: a jet is labelled as a b-jet if a b-quark with $p_T > 5$ GeV is found in a cone of size $\Delta R = 0.3$ around the jet direction. A jet is labelled as a c-jet (or τ-jet) if a c-quark (or τ-lepton) with $p_T > 5$ GeV is found in the cone instead of a b-quark. When no heavy quark nor τ-lepton satisfies these requirements, the jet is labelled as a light jet. No attempt is made to distinguish between u-, d-, s-quarks and gluons. It is important to note that this labelling procedure defines as b-jets most gluon jets splitting to a $b\bar{b}$ pair in the parton-shower process.

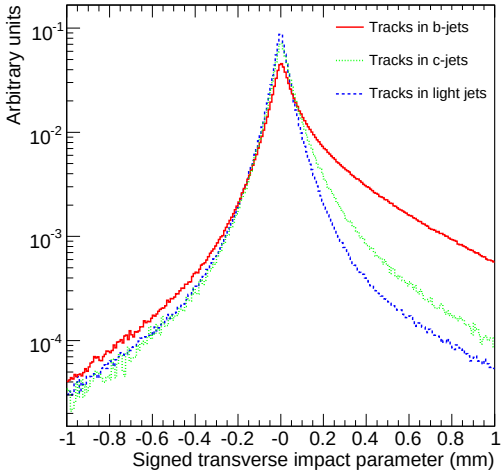

Figure 10.97: Signed transverse impact parameter, d_0, distribution for b-jets, c-jets and light jets.

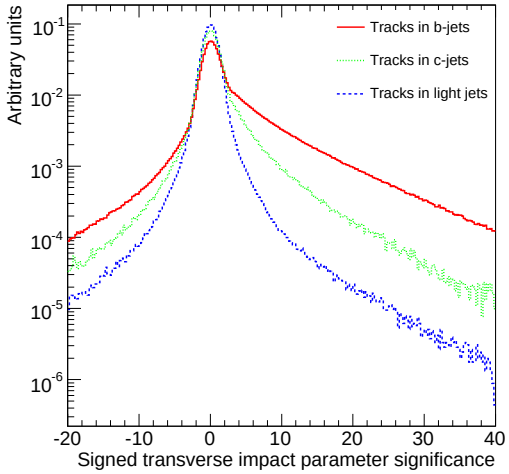

Figure 10.98: Signed transverse impact parameter significance, d_0/σ_{d_0}, distribution for b-jets, c-jets and light jets.

10.8.1.1 Track selection and track impact parameters

The track selection for b-tagging is designed to select well-measured tracks and to reject fake tracks in jets and secondary tracks from K_s^0, Λ and hyperon decays, as well as electrons from photon conversions. Only tracks with transverse momentum above 1 GeV are considered. At least seven precision hits (pixels and strips) are required, of which at least two must be in the pixel detector and one in the pixel vertexing layer. The transverse (d_0) and longitudinal (z_0) impact parameters at the point of closest approach to the vertex must fulfil respectively, $|d_0| < 1$ mm and $|z_0 - z_v| \sin\theta < 1.5$ mm, where z_v is the reconstructed primary vertex position in z and θ is the measured polar angle of the track. The efficiency of these cuts and the resulting fake-track rate in jets are discussed in section 10.2.3 (see in particular figure 10.14).

For the b-tagging algorithms, the impact parameters of tracks are computed with respect to the primary vertex (see section 10.2.4). The transverse impact parameter is signed using the jet direction as measured by the calorimeters: tracks crossing the jet axis behind the primary vertex have a negative impact parameter. The distribution of the signed transverse impact parameter, d_0, is shown in figure 10.97 for tracks reconstructed in b-jets, c-jets and light jets. Figure 10.98 shows the corresponding significance distribution, d_0/σ_{d_0}, which gives more weight to precisely measured tracks.

10.8.1.2 Secondary vertices

To further increase the discrimination between b-jets and light jets, the inclusive vertex formed by the decay products of the B-hadron, including the products of the subsequent charm hadron decay, can be reconstructed. The search starts by combining all track pairs which form a good vertex, using only tracks with a high impact-parameter significance in order to remove the tracks which are compatible with the primary vertex. The invariant mass of the particles originating from

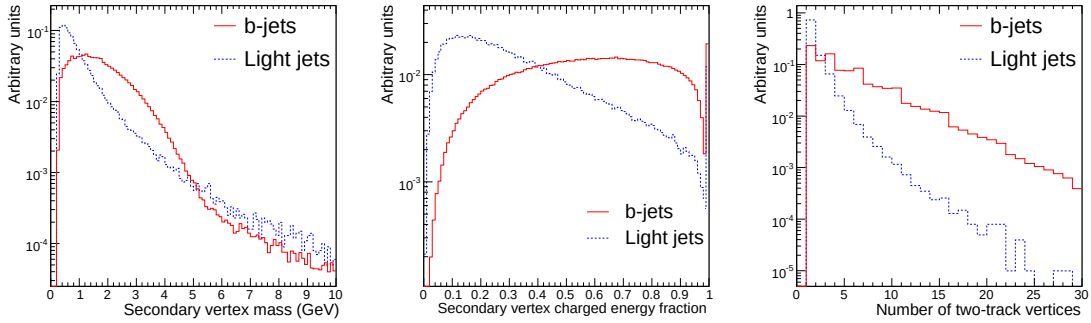

Figure 10.99: Properties of secondary vertices reconstructed in b-jets and light jets: invariant mass of all tracks originating from the vertex (left), the ratio of the sum of the energies of the tracks originating from the vertex to the sum of the energies of all tracks in the jet (middle) and number of two-track vertices (right).

the secondary vertex candidate and the location of this vertex candidate are used to reject vertices which are likely to come from K_s^0/Λ decays and photon conversions or from secondary interactions in material such as the beam-pipe or the vertexing layer. All tracks from the remaining two-track vertices are combined into a single vertex and three of its properties are exploited: the invariant mass of all the tracks originating from the vertex, the ratio of the sum of the energies of the tracks originating from the vertex to the sum of the energies of all tracks in the jet, and the number of two-track vertices. These properties are illustrated in figure 10.99 for b-jets and light jets. The secondary-vertex reconstruction efficiency depends quite strongly on the event topology and the typical efficiencies achieved are higher than 60% for the $t\bar{t}$ and WH events studied here.

10.8.2 Likelihood-ratio tagging algorithms

For both the impact-parameter tagging and the secondary-vertex tagging, a likelihood-ratio method is used: the discriminating variables are compared to pre-defined smoothed and normalised distributions for both the b- (signal) and light- (background) jet hypotheses. Multi-dimensional probability density functions are used as well for some b-tagging algorithms. The ratio of the probabilities defines the track or vertex weight, which can be combined in a jet weight as the sum of the logarithms of the individual weights. The distribution of such a weight is shown in figures 10.100 and 10.101 for b-, c- and light jets for two different b-tagging algorithms: the first one combines only the transverse impact parameter significance of tracks, while the second one combines in two dimensions the transverse and longitudinal impact parameter significances of tracks as well as the three variables from the secondary vertex search discussed above. The former algorithm is simpler and more robust than the latter which will require more time to commission. Currently, no use is made of probability density functions for c-jets, and these are not considered when creating the reference distributions for the signal and background hypotheses.

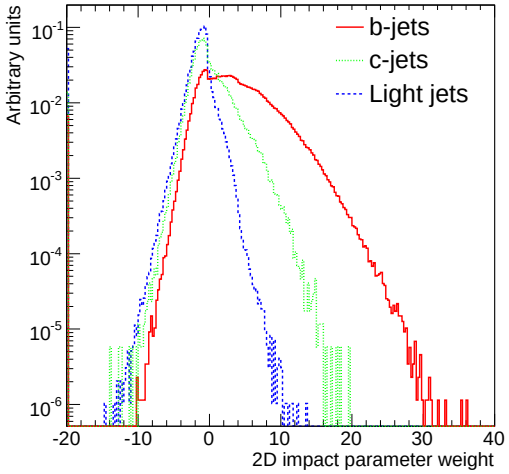

Figure 10.100: Jet b-tagging weight distribution for b-jets, c-jets and purified light jets (see section 10.8.3). The b-tagging algorithm is based on the transverse impact parameter significance of tracks.

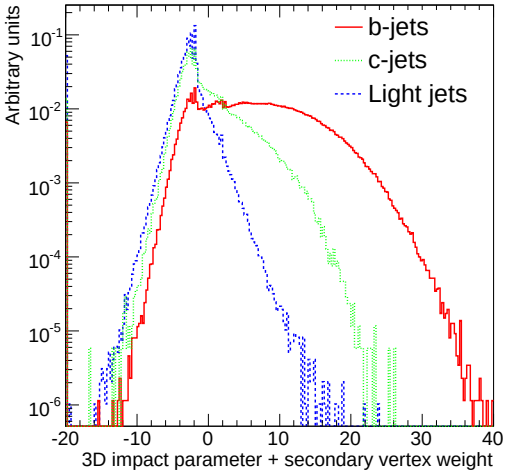

Figure 10.101: Jet b-tagging weight distribution for b-jets, c-jets and purified light jets (see section 10.8.3). The b-tagging algorithm uses the transverse and longitudinal impact parameter significances of tracks as well as the properties of the secondary vertex found in the jet.

10.8.3 Jet activity and jet purification

A difficulty arises as soon as the jet multiplicity is high and various jet flavours are present in the same event: a light jet close in ΔR to a b-jet will sometimes be labelled as a light jet, even though tracks from B-hadron decay with high lifetime content may be associated with it. This leads to an artificial degradation of the estimated performance, which is not related to the b-tagging algorithm itself but to the labelling procedure which strongly depends on the activity in the event. In order to obtain a more reliable estimation of the b-tagging performance, a purification procedure has been devised: light jets for which a b-quark, a c-quark or a τ-lepton are found within a cone of size $\Delta R = 0.8$ around the jet direction are not used to assess the b-tagging performance.

The performance estimated after purification represents the intrinsic power of the b-tagging algorithms and should be similar for different kinds of physics events; in contrast, results obtained using all the light jets, regardless of their environment, are more dependent on the underlying activity in the event. These latter results are, however, more representative of the actual b-tagging performance to be expected for a given physics analysis. This is illustrated in figures 10.102 and 10.103 for two types of physics processes. The WH events correspond to events in which the W decays leptonically and the Higgs boson decays to a $b\bar{b}$ pair (signal case) or is forced to decay to a $u\bar{u}$ or $c\bar{c}$ pair (background case). Such events therefore usually have only two high-p_T and well-separated jets and the light-jet rejection obtained is similar with and without jet purification, as shown in figure 10.102. For semi-leptonic $t\bar{t}$ events, the jet activity is quite high and therefore the two performance curves with and without purification shown in figure 10.103 differ in the region

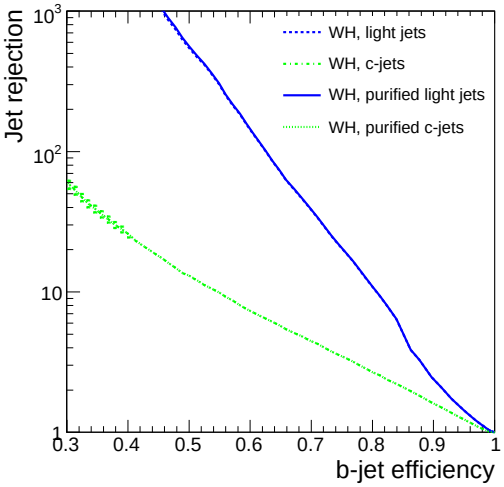

Figure 10.102: Rejection of light jets and *c*-jets with and without purification versus *b*-jet efficiency for WH events with $m_H = 120\,\text{GeV}$, using the *b*-tagging algorithm based on the 3D impact parameter and secondary vertices.

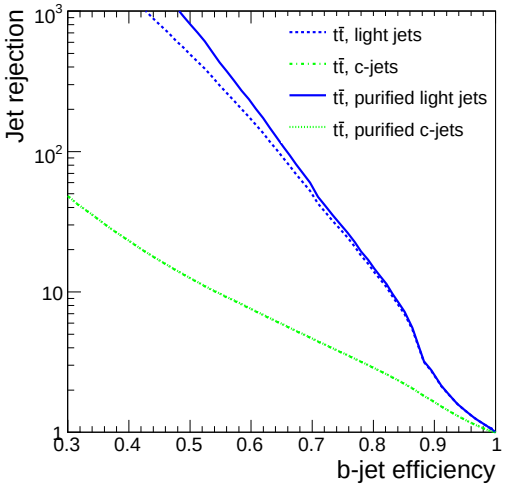

Figure 10.103: Rejection of light jets and *c*-jets with and without purification versus *b*-jet efficiency for $t\bar{t}$ events, using the *b*-tagging algorithm based on the 3D impact parameter and secondary vertices.

of *b*-jet efficiencies below 80%, where the lifetime content dominates over resolution effects. It is also important to note that the purification procedure discards jets coming from gluon-splitting to heavy quarks.

10.8.4 Expected *b*-tagging performance

As shown in figures 10.102 and 10.103, a light-jet rejection higher than 100 can be achieved for a *b*-jet efficiency of 60%. The performance depends strongly on the jet momentum and pseudorapidity. This is illustrated in figures 10.104 and 10.105 for the two *b*-tagging algorithms described above. At low p_T and/or high $|\eta|$, the performance is degraded mostly because of the increase of multiple scattering and secondary interactions. At high p_T, some dilution arises because the fraction of fragmentation tracks in the fixed-size cone increases, and more *B*-hadrons decay outside the vertexing layer: some gain should therefore be achieved by changing the track selection. At very high p_T, the performance degradation arises from pattern-recognition deficiencies in the core of very dense jets.

10.8.5 Soft-lepton tagging

Soft-lepton tagging relies on the semi-leptonic decays of bottom and charm hadrons. It is therefore intrinsically limited by the branching ratios to leptons: at most 21% of *b*-jets will contain a soft lepton of a given flavour, including cascade decays of bottom to charm hadrons. However, when a soft lepton is present, *b*-tagging algorithms based on soft leptons can exhibit high purity. More importantly, they have only small correlations with the track-based *b*-tagging algorithms, which is very important for checking and cross-calibrating performance with data.

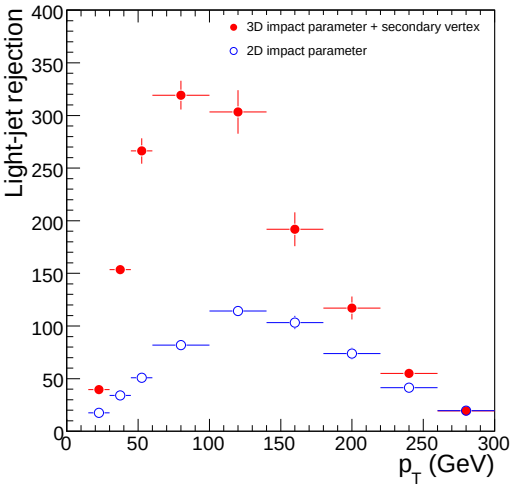

Figure 10.104: Rejection of purified light jets as a function of the jet transverse momentum for two different b-tagging algorithms operating at a fixed b-tagging efficiency of 60% in each bin.

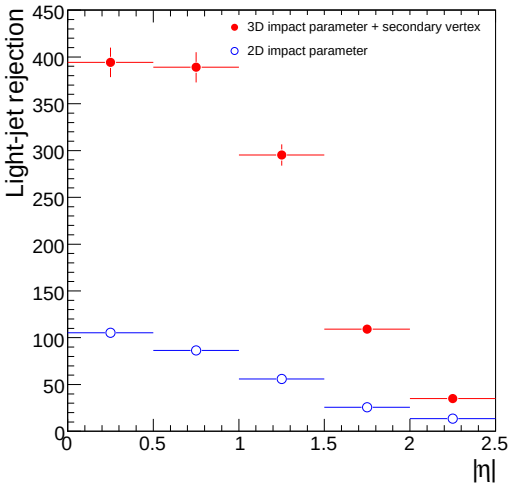

Figure 10.105: Rejection of purified light jets as a function of the jet pseudorapidity for two different b-tagging algorithms operating at a fixed b-tagging efficiency of 60% in each bin.

Soft muons are reconstructed using two complementary reconstruction algorithms (see section 10.3): combined muons, which correspond to a track fully reconstructed in the muon spectrometer and matched with a track in the inner detector, and muons with a low momentum, typically below $\sim 5\,\text{GeV}$, which cannot reach the muon middle and outer stations and are identified by matching an inner-detector track with a segment in the muon spectrometer inner stations only. Muons reconstructed in this way and satisfying some basic selection criteria, $p_T > 4\,\text{GeV}$ and $|d_0| < 4\,\text{mm}$, are associated to the closest jet provided their distance to the jet axis satisfies $\Delta R < 0.5$. Finally, the kinematic properties of the jet-muon system, such as the relative transverse momentum of the muon with respect to the jet axis, are used in order to reject the background caused by punch-through particles and decays in flight in light jets. As shown in figure 10.106 for $t\bar{t}$ events, the soft-muon b-tagging algorithm yields an efficiency of 10% (including branching ratios and identification efficiency) and a light-jet rejection of 200 for jets with $p_T > 15\,\text{GeV}$ and $|\eta| < 2.5$. The rejection against light jets decreases by approximately 30% when the expected contributions from pile-up and especially cavern background at $10^{33}\ \text{cm}^{-2}\ \text{s}^{-1}$ are included.

Reconstructing soft electrons in jets in the electromagnetic calorimeter is more difficult because of the overlap of hadronic showers with the electron shower itself. This is achieved using the soft-electron algorithm [266] which matches an inner-detector track to an electromagnetic cluster, as described in section 10.4.1. The performance of this algorithm is, however, highly dependent on the track density in the jets as well as on the amount of material in front of the electromagnetic calorimeter (photon conversions). As shown in figure 10.107, a light-jet rejection of 90 can be achieved for an efficiency of 7% in WH events. Currently, for a 7% (respectively 10%) b-tagging efficiency, about 75% (respectively 40%) of the surviving light jets are tagged by electrons originating from photon conversions: the performance would therefore substantially improve if these conversions could be rejected further.

2008 JINST 3 S08003

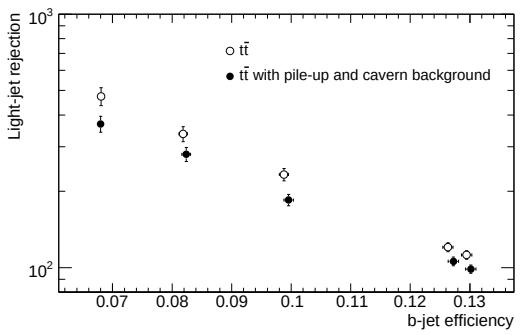

Figure 10.106: Rejection of light jets versus b-tagging efficiency in $t\bar{t}$ events (branching ratios to lepton and lepton identification efficiency included) for the soft-muon b-tagging algorithm. The results are shown without and with the pile-up and cavern background expected at a luminosity of 10^{33} cm^{-2} s^{-1}.

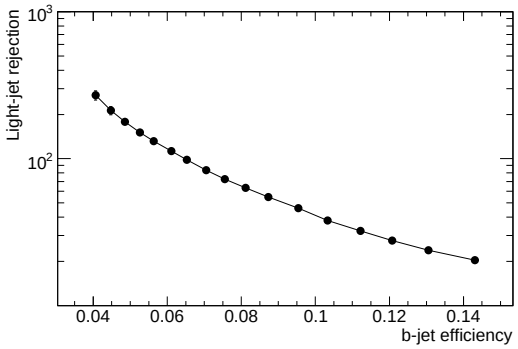

Figure 10.107: Rejection of light jets versus b-tagging efficiency in WH events (branching ratios to lepton and lepton identification efficiency included) for the soft-electron b-tagging algorithm.

10.9 Trigger performance

10.9.1 Overview

This section gives an overview of the performance achieved on simulated raw data using the online physics selection strategy of ATLAS. As already mentioned in section 8.1, components of the reconstruction and analysis software, implemented mostly in the offline environment in previous experiments, have had to be embedded within the trigger system to achieve the required rejection power while retaining excellent sensitivity to the various physics signatures of interest. A great deal of flexibility is provided by the three-level trigger system to adapt to changes in the luminosity (from fill-to-fill and even during a single fill), to variations in the background conditions, and to new requirements which will undoubtedly arise as the understanding of the physics, trigger performance and detector develops.

The approach taken to guarantee good acceptance for as broad a spectrum of physics as possible is to use mainly inclusive criteria for the online selection, i.e. signatures mostly based on single- and di-object high-p_T triggers. The choice of the thresholds is made to have a good overlap with the reach of the Tevatron and other colliders, and to ensure good sensitivity to new particles over a wide range of masses and decay channels. This high-p_T inclusive selection is complemented where necessary with more focussed signatures, such as the presence of several different physics objects or the use of topological criteria.

10.9.2 Selection strategy

The architecture of the trigger and data acquisition system is described in section 8.3 (see in particular figure 8.1) and is based on a three-level trigger system, with a first level (L1) using hardware based on ASIC's and FPGA's, and the other two (L2 and EF or event filter, collectively also called

high-level triggers or HLT) using software algorithms running on farms of commercial computers. At L2, the event selection is based on specialised algorithms, optimised for speed, whereas the EF uses more complex algorithms, basically identical to those used in the offline reconstruction software.

The L2 and EF algorithms are usually "seeded", meaning that reconstruction is normally guided by the previous trigger level to access and process data only in a "Region-of-Interest" (RoI) containing particle candidates. This significantly reduces the processing time (and also data movement from the holding buffers to the L2 processors), without degrading the selection performance. For the EF, and even for L2 where necessary, data can be accessed and processed from the full detector, within the constraints of available data-movement and processing resources. This applies for example to scans of the complete inner detector for low-p_T tracks for the B-physics selection or to the processing of all calorimeter cells for an improved calculation of missing transverse energy. At L2, this can only be done in special cases and for a small fraction of the events due to bandwidth limitations, whereas in the EF the full event data are available in memory. It is also possible to use so-called secondary RoI's which did not contribute to the L1 selection, but provide the coordinates of lower-p_T objects which can be included in the L2 selection.

In the HLT, "feature-extraction" algorithms are used to identify objects (such as electrons or jets) and determine their properties or to determine global characteristics of the event. The sequence of execution of the algorithms (e.g. ordered according to complexity) is chosen to maximise the physics potential and retain adequate flexibility within the available data-movement and processing resources of the HLT. After each step in the sequence, hypothesis algorithms determine whether a given signature is satisfied or not. The processing of any given RoI is stopped as soon as it is clear that it cannot contribute to the selection of the event. The event itself is rejected if none of the signatures in the trigger menu is satisfied.

The initial implementation and capabilities of the DAQ/HLT system are described in section 8.4, where it is stated that the system should handle a L1 trigger rate of ~ 40 kHz, i.e. approximately 50% of the design specification. Clearly, only the availability of real data will allow the whole strategy to be finalised. However, it is important to be able to face this initial phase with the most complete set of tools possible and with a versatile selection architecture, in order to cope with the surprises which are likely to appear at the time of LHC start-up.

10.9.3 Trigger menus

Trigger menus are tables which specify thresholds and selection criteria at each of the three trigger levels to address the physics-analysis requirements of ATLAS. The process of preparing the menus takes into account an assessment of the rejection capabilities at each selection stage and for each signature, and the rate capabilities of each level of the trigger and of the offline computing system. This procedure is iterative and makes use of earlier studies of the L1 trigger and HLT, as documented in [204, 237].

Trigger items, defined as entries in the trigger menu corresponding to selected physics objects, are identified using a notation where a symbol representing a particle type is preceded by a multiplicity value and followed by a E_T-threshold value, e.g. 2e5 corresponds to a requirement of two or more electrons, each with E_T above 5 GeV. The threshold value quoted for L1 is the

Table 10.7: Subset of items from an illustrative trigger menu at 10^{31} cm^{-2} s^{-1}.

Signature	L1 rate (Hz)	HLT rate (Hz)	Comments
Minimum bias	Up to 10000	10	Pre-scaled trigger item
e10	5000	21	$b,c \to e$, W, Z, Drell-Yan, $t\bar{t}$
2e5	6500	6	Drell-Yan, J/ψ, Υ, Z
γ20	370	6	Direct photons, γ-jet balance
2γ15	100	< 1	Photon pairs
μ10	360	19	W, Z, $t\bar{t}$
2μ4	70	3	B-physics, Drell-Yan, J/ψ, Υ, Z
μ4 + J/$\psi(\mu\mu)$	1800	< 1	B-physics
j120	9	9	QCD and other high-p_T jet final states
4j23	8	5	Multi-jet final states
τ20i + xE30	5000 (see text)	10	W, $t\bar{t}$
τ20i + e10	130	1	$Z \to \tau\tau$
τ20i + μ6	20	3	$Z \to \tau\tau$

raw E_T cut applied in the hardware, and high efficiency is only achieved for particles or jets of somewhat higher E_T; this differs from the definition used in previous documents [237]. For inclusive selections, the multiplicity requirement of one is implicit. An "i" following the threshold indicates that an isolation requirement is made in addition. For example, τ20i requires at least one hadronic τ candidate with transverse energy above 20 GeV and with a specific calorimeter isolation requirement in addition. The term "xE" is a short form for E_T^{miss}.

The steering and configuration of the trigger (see section 8.3.6) support the description of both straightforward RoI-based triggers like single electrons, muons, τ-leptons and jets along with more complex triggers like E_T^{miss} and triggers for B-physics. For each trigger level, items in the menu can be pre-scaled to reduce their rates, or "pass-through" flags can be raised, where events are accepted irrespective of the HLT selection decision for the purpose of systematic studies.

The initial start-up luminosity at the LHC is expected to be around 10^{31} cm^{-2} s^{-1}. This provides convenient conditions for commissioning the trigger and the detector sub-systems, validating the trigger and offline software algorithms, and ensuring that basic Standard Model signatures can be observed. The trigger menu for this start-up scenario reflects these requirements and allows for low p_T-thresholds on final-state leptons and photons, without any pre-scaling at L1, and for higher p_T-thresholds, for which most of the HLT algorithms are executed in "pass-through" mode.

Table 10.7 presents an example of a sample of the triggers which will be used at start-up. The rates shown have been estimated using non-diffractive minimum-bias events with a total assumed cross-section of 70 mb. Triggering on single and di-leptons should be possible with quite low p_T-thresholds and without applying isolation or other complex criteria, which must be validated with real data at turn-on. With the exception of the minimum-bias selection, the items indicated are those which should be operable without pre-scaling at 10^{31} cm^{-2} s^{-1}. The full menu contains a number of additional components, including many pre-scaled items with lower thresholds.

The rates for combined triggers which require two or more final-state leptons or photons are expected to be low in most instances, allowing them to be run without pre-scaling with very low thresholds. Significant bandwidth will be devoted to collecting large samples of minimum-bias data for use in physics analysis and for detector and trigger performance studies. Multi-jet triggers will be run at a comparatively high rate to test b-jet tagging in the HLT which is discussed in section 10.9.6. A small amount of bandwidth is allocated for inclusive E_T^{miss} and scalar sum-E_T triggers, as well as using the E_T^{miss} signature in combination with other criteria. Note that for the item τ20i + xE30 in table 10.7, the E_T^{miss} selection is made only at the EF level, in case the corresponding L1 selection takes time to commission. The rate of the τ20i item at L1 is approximately 5 kHz.

The quoted trigger rates are subject to large uncertainties on the cross-sections for QCD processes in proton-proton collisions at LHC energies, and on the modelling of the performance of the detector. The rates indicated assume that the selection cuts will already have been reasonably well tuned to achieve high background rejection with good signal efficiency. There is still scope to use tighter cuts and more delicate variables such as isolation after extensive optimisation and thorough validation. Should the rates turn out to be higher than estimated, the inclusive thresholds could be raised substantially without compromising much of the main initial physics programme, but nevertheless to the detriment of an efficient collection of large data samples required for the initial understanding of the detector performance.

10.9.4 Examples of trigger performance

The expected trigger performance at an initial luminosity of 10^{31} cm^{-2} s^{-1} is illustrated in the following with representative examples from the menu discussed above. As documented in ref. [237] and discussed briefly in section 10.9.6, the trigger also meets the physics requirements up to a luminosity of 10^{34} cm^{-2} s^{-1}.

The performance results presented here were obtained using an exact simulation of the algorithms which are implemented in the L1 hardware and using the same HLT algorithms as those which are run online. The full HLT chain was used to obtain the performance results. As described in section 10.1, these studies have also been made for data simulated with a misaligned and mis-calibrated detector to verify, and improve if necessary, the robustness of the selection.

10.9.4.1 Electrons and photons

The performance of the electron and photon triggers has been evaluated for a luminosity of 10^{31} cm^{-2} s^{-1}, using simulations of single particles and selected physics channels. The trigger efficiencies are quoted with respect to events containing electrons and photons identified with loose offline particle identification cuts (see section 10.4). Inefficiency in the trigger selection arises mainly from tighter selection requirements needed to reduce the background rate to an acceptable level. There are also small losses due to the coarser calorimeter granularity used at L1 and the simpler (and faster) selection algorithms applied at L2 compared to the offline reconstruction.

Figure 10.108 shows the L1, L2 and EF efficiencies as a function of E_T for the signature e10, the menu item selecting electrons with $E_T > 10$ GeV, as estimated using simulations of single electrons. The efficiency reaches a plateau value for E_T above ~ 15 GeV and is quite uniform as a function of $|\eta|$, except for a 10–20% dip in the transition region between the barrel and the end-cap

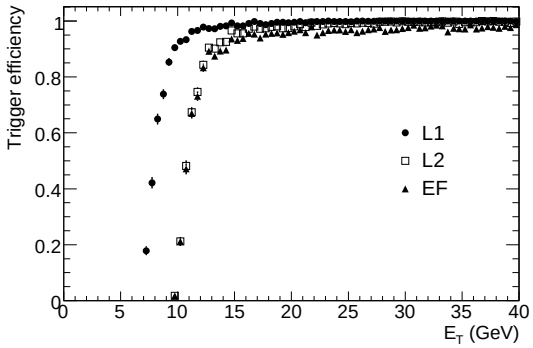

Figure 10.108: Trigger efficiencies at L1, L2 and EF as a function of the true electron E_T for the e10 menu item. The efficiencies are obtained for single electrons and are normalised with respect to the medium set of offline electron cuts discussed in section 10.4.

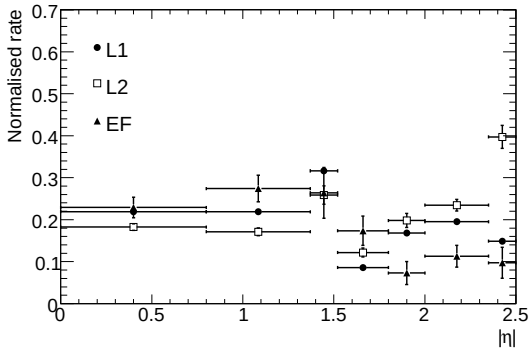

Figure 10.109: Relative rates versus $|\eta|$ for jets passing the L1, L2 and EF trigger selections for the e10 menu item. The relative rates are shown for each of the seven η- ranges used to optimise the offline selection of isolated electrons and are normalised as described in the text.

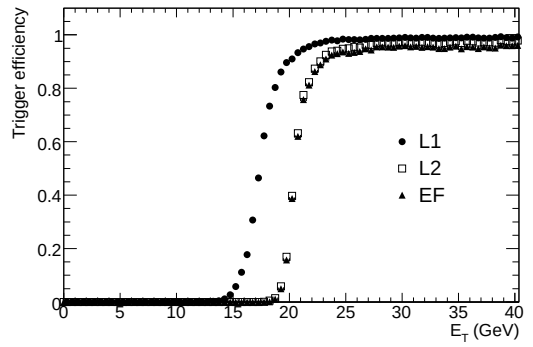

Figure 10.110: Trigger efficiencies at L1, L2 and EF as a function of the true photon E_T for the γ20i menu item. The efficiencies are obtained for single photons and normalised with respect to loose offline photon identification cuts.

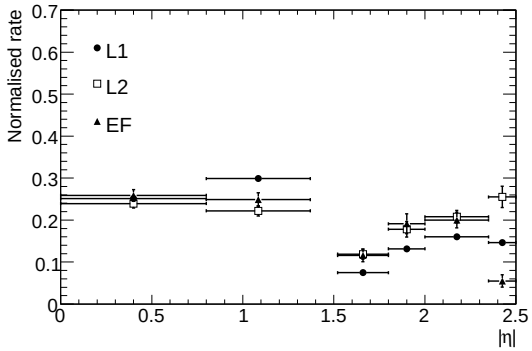

Figure 10.111: Normalised relative rates versus $|\eta|$ for jets passing the L1, L2 and EF trigger selections for the γ20i menu item. The relative rates are shown for each of the six η-ranges used to optimise the offline selection of isolated photons and are normalised as described in the text. The bin corresponding to the barrel/end-cap transition region is not shown because the offline selection excludes it.

calorimeters. Figure 10.109 shows the normalised relative rates expected from QCD jets satisfying the e10 signature as a function of $|\eta|$ for the successive trigger levels. These relative rates are normalised for each trigger level to the total number of events selected and then the rate in each bin is rescaled to that expected for a bin of fixed size $\Delta\eta = 0.5$. The rates are quite sensitive to the result of the trigger efficiency optimisation and their non-uniformity reflects the lower efficiency in the regions where the electromagnetic calorimeter performance is not optimal, as in the barrel/end-cap transition region with $1.37 < |\eta| < 1.52$. Similar results are obtained for photons and shown for the signature γ20i, the menu item selecting isolated photons with $E_T > 20$ GeV, in figures 10.110 and 10.111.

2008 JINST 3 S08003

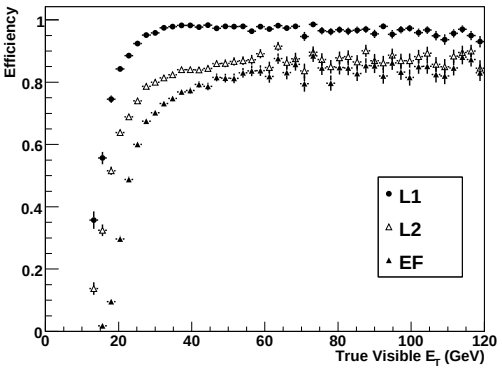

Figure 10.112: Trigger efficiencies at L1, L2 and EF as a function of the true visible E_T of the hadronic τ-decays for the τ20i menu item.

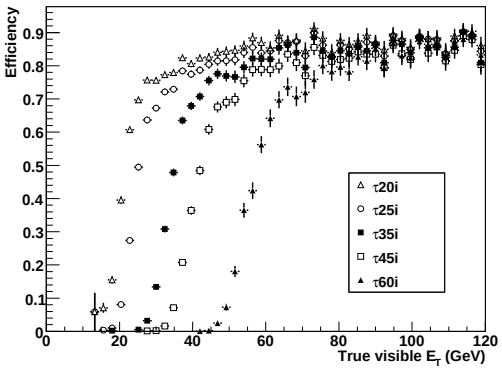

Figure 10.113: Efficiency after EF for τ-trigger items with different thresholds as a function of the true visible E_T of the hadronic τ-decay.

10.9.4.2 τ-leptons and E_T^{miss}

The performance of the trigger for selecting high-p_T τ-leptons is illustrated with the τ20i signature selecting hadronic τ-decays with true visible E_T of the hadronic τ-decay (defined as the summed transverse energy of all the decay products which are not neutrinos) larger than 20 GeV. Figure 10.112 shows the trigger efficiency after each trigger level, normalised to an offline selection with loose requirements (see section 10.7), for hadronic τ-decays from $W \rightarrow \tau\nu$ and $Z \rightarrow \tau\tau$ decays. The efficiency exhibits a drop of approximately 15% after L2, mostly because of the τ-identification cuts applied. The efficiency turn-on rises more slowly than for the electron and photon triggers, especially at L1, reflecting the poorer resolution obtained for hadronic showers. Figure 10.113 shows the efficiency turn-on curves for various τ-trigger thresholds as a function of the true visible E_T of the hadronic τ-decay. The overall efficiency with respect to the offline selection is typically 85% on the plateau.

A somewhat special case is that of E_T^{miss} triggers which can be used either inclusively or in combination with other objects, in particular with jets or hadronic τ-triggers. Because E_T^{miss} is a global property of the event, the RoI-driven L2 trigger is not capable of substantially improving the L1 trigger. However, the E_T^{miss} algorithm in the EF improves substantially on L1 by accessing the precision readout of the entire calorimeter and performing a simplified version of the offline algorithm.

A challenging goal of the τ-selection during the low-luminosity period is to collect a large sample of $W \rightarrow \tau\nu$ decays. This can be achieved using a τ-trigger in combination with a requirement (potentially only at the level of the EF) of substantial E_T^{miss} (see table 10.7). Such events are obviously interesting for physics analyses, but are also needed to monitor the hadronic energy scale using single charged pions, and for other performance studies. An additional goal is to provide triggers with low p_T-thresholds and loose trigger requirements, in addition to the single high-p_T electron and muon triggers, for collecting efficiently Z-bosons decaying into two τ-leptons, where one τ-lepton decays to an electron or muon and the other to hadrons. The background rates for these e/μ+τ triggers are estimated to be in the range of one Hz or less at the initial luminosity of 10^{31} cm^{-2} s^{-1}, with rather loose HLT cuts applied to the trigger objects.

Table 10.8: Summary of L1 single-jet and multi-jet menu items, of L1 pre-scale factors and expected L1 and EF rates at a luminosity of 10^{31} cm^{-2} s^{-1}.

Trigger item	j10	j18	j23	j35	j42	j70	j120	3j10	3j18	4j10	4j18	4j23
Pre-scale factor at L1	42000	6000	2000	500	100	15	1	150	1	30	1	1
L1 rate (Hz)	4	1	1	1	4	4	9	40	140	40	20	8
EF rate (Hz)	4	1	1	1	4	4	9	0.05	1	0.04	0.1	5

10.9.4.3 Jets

The inclusive jet trigger j120 presented in table 10.7 is complemented by a series of pre-scaled items chosen to give an approximately uniform rate across the jet E_T-spectrum. Collecting sufficient statistics over the entire jet E_T-spectrum is important for differential cross-section measurements and also for the measurement of detector, trigger and physics algorithm efficiencies. The set of threshold and pre-scale combinations is expected to be stable with rising luminosity for the first few years of data-taking. The strategy adopted to optimise the jet trigger menu for different luminosities is then primarily to modify the pre-scale factors associated with each jet-trigger threshold, rather than to change the set of thresholds on an ad-hoc basis.

Table 10.8 summarises a set of L1 jet-trigger items, L1 pre-scale factors and L1 and EF rates for a luminosity of 10^{31} cm^{-2} s^{-1}. Since the jet rates cannot be reduced much by the HLT, the EF rates quoted in table 10.8 are obtained through additional pre-scale factors applied wherever necessary. Figure 10.114 shows the corresponding reconstructed differential E_T spectrum of the leading jet after the L1 trigger accept. The differential distribution thus obtained is almost uniform over the range of L1 single-jet triggers run with different pre-scale factors, yielding about 10^8 leading jets with E_T in the range between 10 and 100 GeV for an integrated luminosity of 100 pb^{-1}. Figure 10.115 shows that over this range of jet E_T, the efficiency at threshold of the various pre-scaled jet trigger menu items turns on much more slowly than the corresponding curves for leptons because of the poorer resolution of the jet E_T reconstructed at L1.

10.9.4.4 Muons

The geometrical coverage of the muon trigger detector system (see section 6.6 for a detailed description) limits the overall acceptance for triggering on muons at L1, as illustrated in figure 10.116. The barrel trigger system covers approximately 80% of the η-ϕ plane (over $|\eta| < 1.0$), while the end-cap trigger extends over approximately 96% of the relevant η-ϕ space. The limitations of the barrel system can be seen in figure 10.116, and are dominated by the crack at $\eta < 0.1$ (largely to accommodate inner-detector and calorimeter services), by the regions occupied by the feet of the experiment and by the space taken by the barrel toroid ribs. The end-cap trigger coverage is limited only by the detector supports and by the holes needed for the optical alignment system. Within the fiducial acceptance of the trigger detectors, the L1 trigger efficiency for muons with p_T larger than the selection thresholds exceeds 99%. The L2 trigger then provides a first reduction of the L1 rates by confirming the muon candidates with a more precise measurement of their momentum and by matching them to inner-detector tracks.

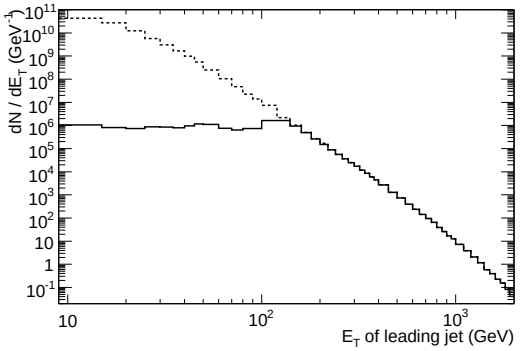

Figure 10.114: Expected differential spectrum for single jets as a function of the reconstructed E_T of the leading jet. The solid line shows the distribution after applying the L1 trigger thresholds and pre-scale factors presented in table 10.8, while the dashed line represents the distribution expected without any trigger requirements.

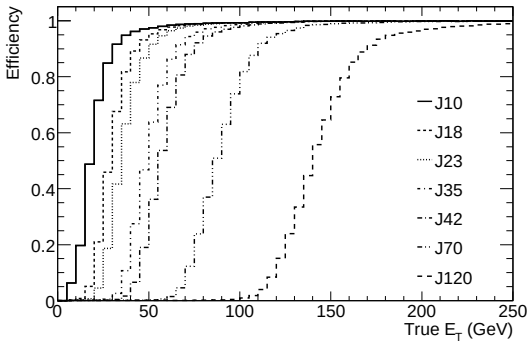

Figure 10.115: Efficiency as a function of the true jet E_T (as defined for a cone of size $\Delta R = 0.4$) for each of the single-jet L1 menu items shown in table 10.8.

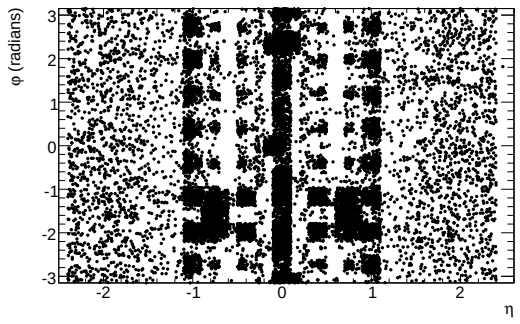

Figure 10.116: Acceptance map in η-ϕ space for the L1 muon trigger, which covers the η-range $|\eta| < 2.4$. The black points represent regions not instrumented with L1 trigger detectors because of the presence of various supports and services.

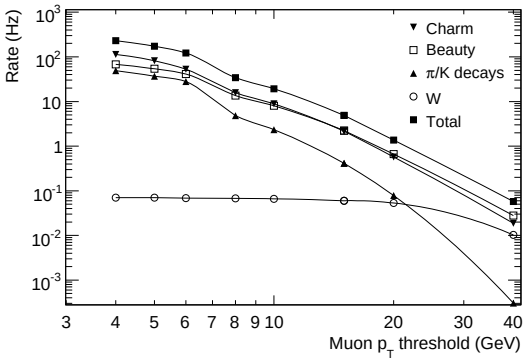

Figure 10.117: Estimated EF output rates for muons as a function of p_T-threshold at a luminosity of 10^{31} cm^{-2} s^{-1}, integrated over the full η-range covered by the L1 trigger, $|\eta| < 2.4$.

The rates of muons at the output of the EF have been computed at a luminosity of 10^{31} cm^{-2} s^{-1}, by summing the contributions from the barrel and end-cap regions of the muon spectrometer. As shown in figure 10.117, several physics processes contribute significantly to the rate. The rates given as a function of the p_T-threshold are for an inclusive muon selection, without applying an isolation requirement. The largest contributions to the total rate in the p_T-range from 4 to 6 GeV are from charm, beauty and in-flight decays of charged pions and kaons. Isolation, as well as refined matching requirements between the tracks in the inner detector and muon spectrometer, can be used to further reduce the rates.

2008 JINST 3 S08003

10.9.4.5 B-physics

The trigger for B-physics is initiated by a single- or di-muon selection at L1. At 10^{31} cm^{-2} s^{-1}, a threshold $p_T > 4$ GeV will be used, rising to about 6 GeV at 10^{33} cm^{-2} s^{-1} to match the rate capabilities of the HLT.

At the initial expected luminosity of 10^{31} cm^{-2} s^{-1}, the dimuon final states are selected by the $2\mu4$ trigger which is expected to have a rate of a few Hz. For single-muon triggers, searches can be made in the HLT for additional features using information from the inner detector and calorimeters, as well as from the muon spectrometer. Mass cuts and secondary-vertex reconstruction are used to select the B-decay channels of interest. Channels, such as $B_d \rightarrow J/\psi(\mu\mu)K^0_s$ and $B_{s,d} \rightarrow \mu\mu$, are triggered by requiring two muons fulfilling J/ψ or $B_{s,d}$ invariant-mass cuts. Identification of the second muon can either originate from a separate L1 RoI, or from the HLT in an enlarged RoI around the first muon. For other channels containing muons, such as $B_d \rightarrow K^{*0}\mu\mu$ or $B_s \rightarrow \phi\mu\mu$, inner-detector tracks are combined to first reconstruct the K^{*0} or ϕ and then the muon tracks are added to reconstruct the $B_{s,d}$.

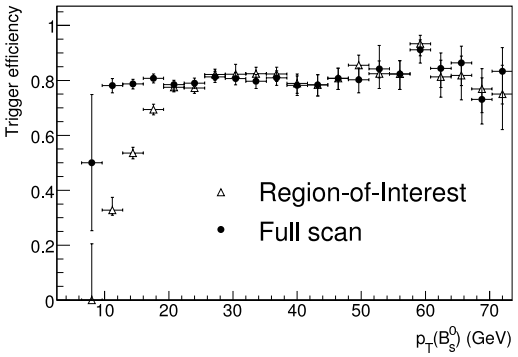

Figure 10.118: Trigger efficiency for $B_s \rightarrow D_s^- a_1^+$ events passing the offline selection as a function of the p_T of the B-meson. The results are shown for two HLT scenarios, the most performant one, based on a full scan of the inner detector which can be used at low luminosity, and a RoI-based scan which can be used at higher luminosities (see text).

For hadronic final states like $B_s \rightarrow D_s^-\pi^+$ and $B_s \rightarrow D_s^-\mathrm{a}_1^+$, inner-detector tracks are combined to reconstruct first the ϕ-meson from the D_s decay, then the D_s and finally the B_s. Two different strategies are used for finding the tracks, depending on luminosity. Full reconstruction over the whole inner detector can be performed at 10^{31} cm^{-2} s^{-1}, since the L1 muon rate is comparatively modest, while at higher luminosities reconstruction will be limited to L1 jet RoI's with $E_T > 5$ GeV. This latter approach has lower efficiency for selecting the signal, as shown in figure 10.118, but requires fewer HLT resources for a fixed L1 rate. If one combines triggers for hadronic final states and pre-scaled single muon triggers needed for trigger efficiency measurements, the overall rate for B-physics triggers is approximately 10 Hz at 10^{31} cm^{-2} s^{-1}.

10.9.5 Trigger commissioning

A detailed strategy for commissioning the trigger during initial running with beam is being developed. It is assumed that the luminosity will be significantly less than 10^{33} cm^{-2} s^{-1} during this period. A first step will be to establish a time reference for bunches of protons colliding at the interaction point in ATLAS. Signals from passive beam pick-ups will be used to form a filled-bunch trigger with known latency. This will be combined with the minimum-bias trigger, based on scintillation counters which are mounted in front of the end-cap cryostats (see section 5.5), which will

be used to signal inelastic proton-proton collisions. The resulting interaction trigger will be used in setting up the timing of the experiment for the detector readout and of the calorimeter and muon L1 trigger systems.

Once the timing-in of the detector is completed, the minimum-bias trigger will be used to collect data for initial physics studies, in parallel with continuing work on commissioning the rest of the trigger. Since the calorimeter and muon L1 trigger systems are digital, commissioning tasks such as calibration using real (minimum-bias) data can be done offline, comparing the results read out from the trigger systems with corresponding quantities from the detector readout. It is anticipated that the trigger system will be brought on-line progressively. A first step will be to use, in parallel with a pre-scaled minimum-bias selection, the L1 trigger with loose and simple selection criteria, with relaxed requirements in the muon trigger and not using calorimeter quantities such as isolation and global energy sums, which are sensitive to low-energy detector behaviour. Tighter and more complicated selections will be brought in progressively after thorough offline validation of their performance.

Once the calorimeter and muon L1 triggers are operational, work will ramp up on commissioning the HLT. Many aspects can be addressed offline, using exactly the same algorithms as online, but running on data recorded previously. Then the L2 and EF algorithms will be used online in passive mode, while still recording all events selected by L1. The highest-priority physics channels will initially be covered by high-threshold L1 triggers which are passed through the HLT without further selection, while using the HLT actively elsewhere. Analysis of the recorded data will provide further optimisation of the algorithms and cross-checks on the efficiency of the HLT. As the luminosity increases towards 10^{33} cm^{-2} s^{-1}, the full power of the trigger will be required to limit the event rate, while retaining high efficiency for the physics channels of interest.

As an example, one can consider in more detail the commissioning of the L1 muon trigger. Given the low luminosity assumed for initial data-taking (10^{31} cm^{-2} s^{-1}), the related low cavern-background rates expected and the large bunch spacing foreseen (75 ns or more), the configuration parameters of the muon trigger system can initially be relaxed while maintaining acceptable rates. The data collected will be used to check and complete the commissioning of the muon trigger, which has already started using cosmic-ray data. In particular, large samples of muons will be needed to fine-tune the time calibration of the full system, with a required accuracy of about 3 ns in the barrel system. Initial coincidence roads will have been prepared based on simulation and will be available for several p_T-thresholds from about 4 GeV to 40 GeV. Once real data are available with large statistics, these roads will be checked and optimised with muons reconstructed over the full acceptance of the detector, using the p_T-measurement obtained with the inner detector. The commissioning of the muon trigger will use data collected with wide coincidence roads and also with other triggers (minimum bias, jets). The information recorded from the L1 muon trigger will be examined together with the results of the offline reconstruction, allowing measurements of the trigger efficiency for muons as a function of p_T.

In a similar way, the start-up menu for the electron and photon selection must provide data samples needed to commission trigger and detectors, as well as for physics analyses. Relevant physics processes include $J/\psi \rightarrow ee$, $\Upsilon \rightarrow ee$, Drell-Yan, $Z \rightarrow ee$, $W \rightarrow e\nu$ and direct photon production. The menu discussed above selects such events with single electrons with E_T above $\sim$ 10 GeV or single photons with E_T above $\sim$ 20 GeV, in addition to the selection with double-object triggers at significantly lower thresholds.

2008 JINST 3 S08003

Table 10.9: Subset of items from two illustrative trigger menus at L1 (left) and at the HLT (right) for a luminosity of 2×10^{33} cm^{-2} s^{-1}. The capital letters designate L1 trigger objects, whereas the small letters designate HLT trigger objects. The examples given are more to illustrate the evolution of the rates and thresholds as a function of luminosity, when comparing to table 10.7, than to provide accurate predictions of the expected rates.

L1 signature	Rate (kHz)
EM18I	12.0
2EM11I	4.0
MU20	0.8
2MU6	0.2
J140	0.2
3J60	0.2
4J40	0.2
J36+XE60	0.4
TAU16I+XE30	2.0
MU10+EM11I	0.1
Others	5.0

HLT signature	Rate (Hz)
e22i	40
2e12i	< 1
γ55i	25
2γ17i	2
μ20i	40
2μ10	10
j370	10
4j90	10
j65+xE70	20
τ35i+xE45	5
2μ6 for B-physics	10

10.9.6 Evolution to higher luminosities

Building on the experience gained during the start-up phase, the trigger algorithms and parameters will be optimised to provide a trigger selection for use at higher luminosities. As the LHC luminosity ramps up towards its design value, tighter selections will be needed to control the rate. These will include using complex signatures involving multiple observables, higher p_T-thresholds, tighter selection criteria and requiring a more precise matching between different detector systems.

The trigger reconstruction and selection software must be robust against higher detector occupancies, pile-up and cavern backgrounds, which may affect the performance significantly at luminosities above 10^{33} cm^{-2} s^{-1}. Many studies have been made to assess the performance of the trigger and data-acquisition system at high luminosities. Table 10.9 [237] shows an illustrative sample of L1 and HLT signatures, which could be used under stable operating conditions at luminosities around 2×10^{33} cm^{-2} s^{-1}.

The triggers should guarantee coverage of the full physics programme, including searches for new physics and precision measurements of Standard Model parameters. The signatures include single- and di-lepton, photon and jet triggers, similar to those used at 10^{31} cm^{-2} s^{-1}, but with higher p_T-thresholds and tighter selection criteria. Requirements on lepton and photon isolation, large E_T^{miss}, and possibly other complex criteria such as flavour tagging, which will have been operated only in a passive or loose mode during the start-up phase, will surely play an important role to achieve a sufficient rate reduction.

As an example, one can consider the case of b-jet tagging at the HLT. The performance of the proposed HLT b-tagging algorithms is based on transverse and longitudinal impact parameters of charged tracks in jets. The L2 and EF b-tagging efficiencies are strongly correlated with the offline b-tagging efficiency. To preserve full acceptance for an offline analysis with its b-tagging

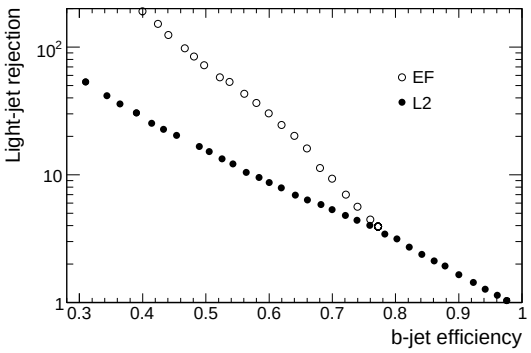

Figure 10.119: Light-jet rejection factor as a function of *b*-jet efficiency at L2 and EF.

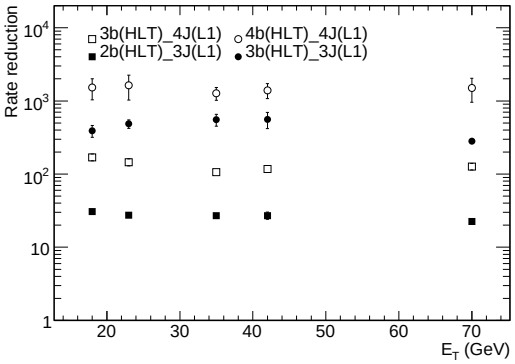

Figure 10.120: Rate reduction after L2 and EF as a function of E_T, using *b*-jet signatures with an efficiency of 70% per *b*-jet. Specific examples are shown, e.g. $3b(HLT)\ 4J(L1)$ which uses the combination of four jets at L1 and of three *b*-jets at the HLT.

selection criteria set for a given offline *b*-jet efficiency, the L2 and EF *b*-tagging algorithms must operate at an efficiency which is higher. Since most of the offline *b*-tagging results are obtained for *b*-jet efficiencies of $\sim 60\%$, the results quoted here for *b*-tagging in the HLT are given for *b*-jet efficiencies of approximately 80% for L2 and 70% for EF. Figure 10.119 shows that light-jet rejection factors larger than ten can be achieved, both at L2 and EF for a *b*-jet efficiency of 70% and *b*-jet tagging could thus allow a more flexible operation of the L1 multi-jet trigger menus. To illustrate this, the rate reduction which could be achieved at L2 or EF by requesting two or more *b*-jets, is shown as a function of E_T in figure 10.120.

Far more accurate projections of the rates given in table 10.9 will become possible once real data from the start-up phase have been accumulated and analysed. The total output rate of the trigger system at luminosities above 10^{33} cm^{-2} s^{-1} should remain fixed at approximately 200 Hz, a rate defined by the capabilities of the offline computing system.

10.9.7 Measurements of trigger efficiency from data

Since the trigger efficiency represents a basic element of any physics analysis, it is essential to have several independent methods for estimating it. It is important to depend as little as possible on Monte-Carlo models of LHC physics and on the detector operating conditions, particularly at the start-up of the LHC programme, given the large extrapolation from lower-energy measurements. Techniques under study include the "tag-and-probe" method, e.g. triggering events with the electron in $Z \rightarrow ee$ decays and measuring the efficiency to trigger on the positron in addition, and the "bootstrap" method, e.g. using minimum-bias events to measure the efficiency to trigger on low-p_T jets, then triggering on low-p_T jets and using them to measure the efficiency to trigger on higher-p_T jets, etc. Redundant selections can also be used, in which one or more of the steps in the selection are skipped, thereby providing the possibility of determining the corresponding contributions to the inefficiency.

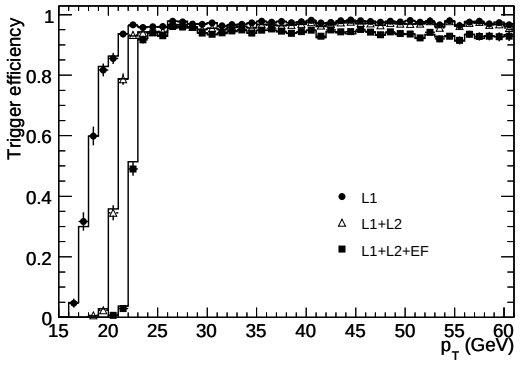

Figure 10.121: Trigger efficiencies as expected to be measured from data using the tag-and-probe method for electrons from approximately 25,000 $Z \rightarrow ee$ decays corresponding to an integrated luminosity of 100 pb^{-1}. The efficiencies are normalised with respect to a reference loose offline selection. The points with error bars show the measured efficiencies after L1 (full circles), L2 (open triangles) and the EF (full squares). Also shown as histograms are the corresponding distributions obtained using as a reference the Monte-Carlo truth information.

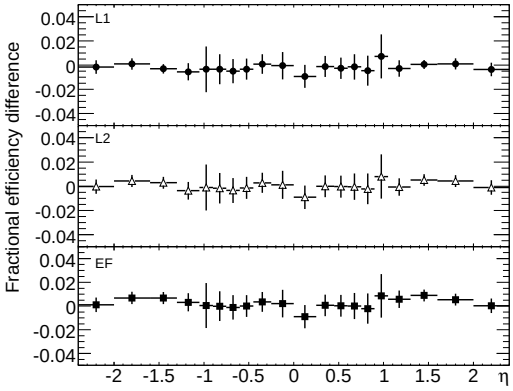

Figure 10.122: Difference between trigger efficiency as expected to be measured from data (using the tag-and-probe method for muons from $Z \rightarrow \mu\mu$ decays) and true efficiency (obtained using as a reference the Monte-Carlo truth information) normalised to true efficiency as a function of η. The efficiencies are normalised with respect to a reference loose offline selection. The results are shown after L1 (top), L2 (middle) and EF (bottom), and correspond to a sample of approximately 50,000 $Z \rightarrow \mu\mu$ decays for an integrated luminosity of 100 pb^{-1}.

As an example, studies have been made for the $Z \rightarrow ee$ tag-and-probe method, using events satisfying the e22i single-electron trigger selection, in which an opposite-charge electron pair has been identified by the offline reconstruction with an invariant mass near the Z peak. Using the second lepton in these events as the probe which was not required to pass any trigger selection, the efficiency (relative to the offline selection) of a given trigger signature can be measured. Figure 10.121 shows the efficiency of the e22i trigger as a function of p_T of the electron, as measured without any reference to Monte-Carlo truth information in the simulated sample of $Z \rightarrow ee$ events. The shape of the trigger-threshold curves in figure 10.121, obtained using as a reference the Monte-Carlo truth information, are accurately reproduced by the tag-and-probe measurements, and the values agree to better than 1% on the plateau for a sample of $Z \rightarrow ee$ decays corresponding to an integrated luminosity of 100 pb^{-1}. It is estimated that with such an integrated luminosity, the e22i trigger efficiency can be evaluated with a statistical accuracy of approximately 0.2%. Obviously, more data will be needed to study the trigger efficiency with much higher granularity, in particular as a function of η and ϕ. An example of such a study is shown in figure 10.122 for a sample of reconstructed $Z \rightarrow \mu\mu$ decays also corresponding to an integrated luminosity of 100 pb^{-1}. The results are plotted as the relative difference between the trigger efficiency measured using the tag-and-probe method and the true trigger efficiency as obtained from the Monte-Carlo truth information. The statistical accuracy achieved per bin is at the percent level.

A similar method can be used to measure the efficiency for triggering on hadronic τ-decays, which can be measured using $Z \rightarrow \tau\tau$ samples collected with single electron and muon triggers (as shown in table 10.7), where one of the τ-leptons decayed leptonically. In events where the second τ-lepton decays to hadrons, one can measure the fraction of τ-leptons reconstructed offline, which also pass the τ-trigger. This will be done by correlating the detailed information recorded from the trigger with the results of the offline reconstruction and will require more integrated luminosity than in the case of the electron and muon triggers.